HIGH-PRECISION TIME-DOMAIN ASTROPHYSICS IN CROWDED STAR-FIELDS WITH GROUND BASED TELESCOPES

GLOBULAR CLUSTERS AND THE MITIGATION OF THE ATMOSPHERIC TURBULENCE

Roberto Figuera Jaimes

A Thesis Submitted for the Degree of PhD
at the
University of St Andrews

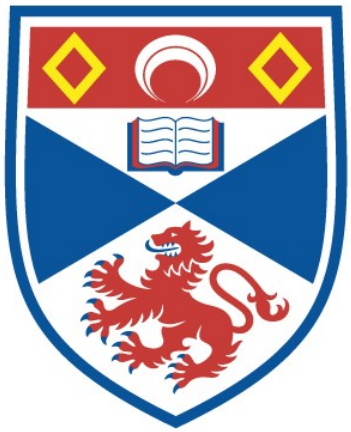

2018

High-Precision Time-Domain Astrophysics in Crowded Star-Fields with Ground Based Telescopes

Globular clusters and the mitigation of the atmospheric turbulence

M. Sc. Roberto Figuera Jaimes

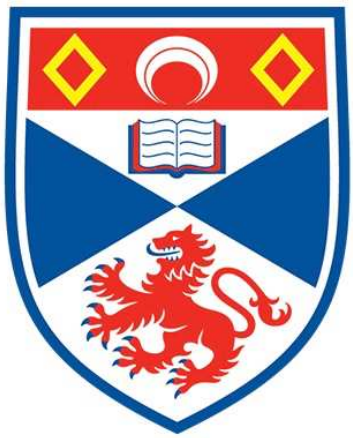

University of
St Andrews

This thesis is submitted in partial fulfilment for the degree of
PhD
at the University of St Andrews

April, 2018

Abstract

We carried out a three year (2013-2015) observational campaign at the Danish 1.54-m Telescope at the ESO observatory at La Silla in Chile in which we obtained ∼1000 astronomical images in the field of 11 Galactic globular clusters. The selection of these stellar systems was focused mainly on the visibility of the targets and their relevant physical properties available in the catalogues, among them were considered the density, variable stars known, colour-magnitude diagrams, and luminosity.

The telescope was equipped with an electron-multiplying CCD (EMCCD) with the aim of taking very short exposure-time images. The camera was configured to take 10 frames per second. Due to this, the brighter stars observed were not affected by saturation, it helped to give higher signal to noise ratio to the fainter stars and, importantly, it minimised the effects of the atmospheric turbulence such as blending between stars in the crowded fields. To produce normal-exposure-time images (minutes) we implemented the shift-and-add technique that also enabled us to produce images with better angular resolution than previously achieved with conventional CCDs on ground-based telescopes, and even enabled us to produce images with angular resolution close to that obtained with space telescopes.

The detection of the stars in each of the globular clusters and the photometry was performed via difference image analysis by using the DanDIA pipeline whose procedures and mathematical techniques have been demonstrated to produce high-precision time-series photometry of very crowded stellar regions.

We produced time-series photometry for ∼15000 stars in the fields observed which were statistically analysed in order to automatically extract variable stars. Our aim is to complete, or improve, the census of the variable star population in the globular clusters. In NGC 6715, we found light curves for 17 previously known variable stars near the edges of our reference image (16 RR Lyrae and 1 semi-regular) and we discovered 67 new variables (30 RR Lyrae, 21 long-period irregular, 3 semi-regular, 1 W Virginis, 1 eclipsing binary, and 11 unclassified). This cluster was particularly interesting because apart from the results obtained, it shows the benefits of using the EMCCD cameras and the shift-and-add technique. It is a cluster studied several times including data obtained with the OGLE survey and also with the Hubble Space Telescope and our discoveries were still new. Our new RR Lyrae star discoveries help confirm that NGC 6715 is of intermediate Oosterhoff type.

In the other 10 globular clusters, we obtained light curves for 31 previously known variable stars (3 L, 2 SR, 20 RR Lyrae, 1 SX Phe, 3 cataclysmic variables, 1 EW and 1 NC) and we discovered 30 new variables (16 L, 7 SR, 4 RR Lyrae, 1 SX Phe and 2 NC). In NGC 6093, we analysed the famous case of the 1860 Nova, for which no observations of the Nova in outburst have been made until the present study. Ephemerides and photometric measurements for the variable stars are available in electronic form through the Strasbourg Astronomical Data Centre.

"For the achievement of triumph it has always been indispensable to pass through the path of sacrifice."

"The art of victory is learned in defeat."

Simon Bolivar

Dedication

To Venezuela

A great and rich country with so many possibilities and resources but so many challenges and complications.

Declaration

Candidate's declaration

I, Roberto Jose Figuera Jaimes, do hereby certify that this thesis, submitted for the degree of PhD, which is approximately 48,000 words in length, has been written by me, and that it is the record of work carried out by me, or principally by myself in collaboration with others as acknowledged, and that it has not been submitted in any previous application for any degree. I was admitted as a research student at the University of St Andrews in September 2012. I received funding from an organisation or institution and have acknowledged the funder(s) in the full text of my thesis.

Date Signature of candidate

Supervisor's declaration

I hereby certify that the candidate has fulfilled the conditions of the Resolution and Regulations appropriate for the degree of PhD in the University of St Andrews and that the candidate is qualified to submit this thesis in application for that degree.

Date Signature of supervisor

Permission for publication

In submitting this thesis to the University of St Andrews we understand that we are giving permission for it to be made available for use in accordance with the regulations of the University Library for the time being in force, subject to any copyright vested in the work not being affected thereby. We also understand, unless exempt by an award of an embargo as requested below, that the title and the abstract will be published, and that a copy of the work may be made and supplied to any bona fide library or research worker, that this thesis will be electronically accessible for personal or research use and that the library has the right to migrate this thesis into new electronic forms as required to ensure continued access to the thesis.

I, Roberto Jose Figuera Jaimes, confirm that my thesis does not contain any third-party material that requires copyright clearance. The following is an agreed request by candidate and supervisor regarding the publication of this thesis:

Printed copy

No embargo on print copy.

Electronic copy

No embargo on electronic copy.

Date Signature of candidate

Date Signature of supervisor

Underpinning Research Data or Digital Outputs

Candidate's declaration

I, Roberto Jose Figuera Jaimes, hereby certify that no requirements to deposit original research data or digital outputs apply to this thesis and that, where appropriate, secondary data used have been referenced in the full text of my thesis.

Date Signature of candidate

Acknowledgements

To my parents Maria Angelica Jaimes and Juan Carlos Figuera for their unconditional support not only during this thesis but throughout my whole life.

To the Scottish Universities Physics Alliance (SUPA) for funding 3.5 years of my doctorate.

To Keith Horne for accepting to be my doctorate and thesis supervisor and the support given to me in numerous opportunities, especially during my time at Saint Andrews.

To Daniel Bramich, a person who is not the first time I thank in my life, for supervising my doctorate as well as Ph. D. thesis, for his asserted support and unselfish help. Especially during the first years of doctorate when we had the opportunity to work together at the European Southern Observatory. It was a fruitful experience. Also for introducing me to the RoboNet and MINDSTEp consortia. Many thanks will not be enough.

To Christiane Helling and Martin Dominik, examiners during my doctorate, for their comments and suggestions to constantly achieve a high-performance during my doctorate.

To the student services fund of the University of Saint Andrews for covering flight expenses from Venezuela to Scotland and a 3-night stay for my thesis defense.

To Alexander Scholz and Pierre Maxted, examiners of this thesis, for the excellent organization of the viva examination and great feedback I received.

To the European Southern Observatory (ESO) especially to Eric Emsellem for giving me the opportunity, once again, to mature in this amazing institution during the first two years of my doctorate. It is difficult to quantify in words the incredible time and experience I had working at ESO.

To MINDSTEp, especially to Uffe Jorgensen and Martin Dominik heads of the MINDSTEp programme for supporting this project through observational time at the Danish 1.54 m telescope at La Silla Observatory with the EMCCD camera which was the fundamental device used during this research. Similarly to Jesper Skottfelt for supporting us with the software needed for the early stages of the EMCCD observations.

To RoboNet, especially to Rachel Street a person whom I have had the opportunity to work with in several opportunities since the beginning of my doctorate. Thanks for the opportunities you have given me to participate and collaborate on your projects and the two occasions in which you received me at Las Cumbres Observatory. It has been very fruitful and I have gained a lot of experience.

To the ESO and Saint Andrews Human Resources staff, especially to Lesley Aitken, Pamela Bristow, Stella-Maria Chasiotis-Klingner, Wendy Clark, Anna Michaleli, Betül Özener, and Christina Stoffer for their diligent and asserted support sorting out the paperwork needed during my doctorate including travels and visas.

To the ESO helpdesk especially to Xavier Garcia and Tamas Tutuntzisz for their diligent, competent, asserted support, and no hesitation to help with all my computational needs.

To Las Cumbres Observatory staff, for their diligent work sorting out my visits to the headquarter, especially to Nan Brooks, Jodi Shaw, Sarah Rettinger, and Brian Haworth for his excellent dedication sorting out all my computational needs.

To Aldo Batta, Jose Burgos, Luis Perez, Felipe Ramon, Marie Rodriguez, Jose Sacahui, and Laith Taj Aldeen for their support at different stages of my doctorate.

To any other person that should be on this page.

Contents

1 Introduction **1**
- 1.1 Importance of globular clusters . . . 5
- 1.2 Types of variables in globular clusters . . . 7
  - 1.2.1 RR Lyrae . . . 7
  - 1.2.2 SX Phoenicis . . . 9
  - 1.2.3 Pulsating red giants . . . 9
  - 1.2.4 Eclipsing binaries . . . 10
  - 1.2.5 Cataclysmic variables . . . 10
  - 1.2.6 Cepheid variables - W Virginis stars . . . 11
  - 1.2.7 RV Tauri stars . . . 12
- 1.3 What can be learned from the variables and why they are important . . . 12
  - 1.3.1 Oosterhoff type . . . 12
  - 1.3.2 RR Lyrae . . . 13
  - 1.3.3 SX Phoenicis . . . 15
  - 1.3.4 Eclipsing Binaries . . . 15
  - 1.3.5 Cataclysmic Variables . . . 15
  - 1.3.6 Asymptotic and red giant branch variables . . . 16

2 CCD vs EMCCD Technology **17**
- 2.1 Definition of CCDs . . . 17
- 2.2 Definition of EMCCDs . . . 19
- 2.3 Comparison between CCDs and EMCCDs . . . 19
  - 2.3.1 Mode 1 (Unity gain or Conventional mode) . . . 20
  - 2.3.2 Mode 2 (Moderate to high gain or Linear mode) . . . 20
  - 2.3.3 Mode 3 (High gain and thresholding or Photon counting mode) . . . 21
- 2.4 EMCCD Reductions . . . 21
  - 2.4.1 Tip-tilt correction . . . 23
  - 2.4.2 Image quality and stacking . . . 24
  - 2.4.3 Photometry . . . 24

3 New Variables in Globular Clusters **29**
- 3.1 Selection of Clusters . . . 29
- 3.2 Time-Resolved Imaging Observations . . . 30
- 3.3 Photometric calibration . . . 32
- 3.4 Astrometry and finding chart . . . 33
- 3.5 Known and new variables . . . 33
  - 3.5.1 Root mean square . . . 33

3.5.2 S_B statistic . . . 34
3.5.3 Stacked difference image . . . 35
3.6 Classification . . . 35
3.6.1 Colour-magnitude diagram . . . 36
3.6.2 Period search . . . 37
3.6.3 Variable star classification . . . 37

4 Summary of Results **39**
4.1 NGC 6715 / C1851-305 / Messier 54 . . . 39
4.1.1 Known variables . . . 39
4.1.2 New variables . . . 40
4.2 Oosterhoff dichotomy . . . 42
4.3 **NGC 104 / C0021-723 / 47 Tucanae** . . . 50
4.3.1 Known variables . . . 51
4.3.2 New variables . . . 51
4.4 **NGC 5139 / C1323-472/ Omega Centauri** . . . 54
4.4.1 Known variables . . . 54
4.4.2 New variables . . . 54
4.5 **NGC 5286 / C1343-511 / Caldwell 84** . . . 57
4.5.1 Known variables . . . 58
4.5.2 New variables . . . 59
4.6 **NGC 6093 / C1614-228 / M 80** . . . 63
4.6.1 Known variables . . . 64
4.6.2 New variables . . . 65
4.7 **NGC 6121 / C1620-264 / M4** . . . 67
4.8 **NGC 6541 / C1804-437** . . . 69
4.8.1 Known variables . . . 69
4.8.2 New variables . . . 70
4.9 **NGC 6656 / C1833-239 / M 22** . . . 72
4.9.1 Known variables . . . 72
4.10 **NGC 6681 / C1840-323 / M70** . . . 75
4.10.1 Known variables . . . 75
4.10.2 New variables . . . 76
4.11 **NGC 6723 / C1856-367** . . . 78
4.11.1 Known variables . . . 78
4.12 **NGC 6752 / C1906-600 / C93** . . . 81
4.12.1 Known variables . . . 81

5 Discussions and Conclusions **83**
5.1 The DanDIA pipeline . . . 84
5.2 The EMCCD implementation . . . 85
5.3 Our analysis . . . 89
5.4 Our future work . . . 91

A Histogram of observations **95**

B Photometric calibrations **97**

C Cross identification between variables **99**

List of Figures

1.1 Field of view of globular cluster NGC 5272 studied by Shapley (1918d). As seen in the image, the core of the cluster appears crowded in the images and it was only possible to detect variability in their surrounding areas. Small circles are variable stars found in the cluster. This study was done using photographic plates. 3

1.2 Field of view of globular cluster NGC 6715 studied by Layden & Sarajedini (2000a). Again, the core of the cluster appears crowded in the image and it was only possible to detect variability in the surrounding areas. Small circles are variable stars found in the cluster. This study was done using a CCD. 4

1.3 Histogram of the central luminosity density for globular clusters listed in Harris (1996) built with a binning of 0.2. The vertical lines correspond to the minimum, mean, and maximum values, respectively. 6

1.4 Hertzsprung-Russell diagram for globular clusters. Image taken from Enciclopedia of Astronomy and Astrophysics 8

1.5 Light curves of two RR Lyrae stars in globular cluster NGC 6981. On the left a RR0 type is shown and of the right a RR1 type. The red lines correspond to the fit obtained with a 10 harmonics in the Fourier analysis of Eq. 1.6. 14

2.1 Structure of a conventional CCD. (Extracted from Figure 1 in Smith et al. 2008). The three basic parts of a CCD are shown. 18

2.2 Structure of a conventional EMCCD. (Extracted from Figure 1 in Smith et al. 2008). The three basic parts of a CCD are shown. 19

2.3 A 512×512 pixel square image that corresponds to a bias taken with the EMCCD camera used at the Danish 1.54 m telescope at ESO-La Silla observatory. 22

2.4 A 512×512 pixel square image that corresponds to a dark taken with the EMCCD camera used at the Danish 1.54 m telescope at ESO-La Silla observatory. It is the result of collapsing ten 0.1 second exposure time images 22

2.5 A 512×512 pixel square image that corresponds to a bias-subtracted and normalized flat taken with the EMCCD camera used at the Danish 1.54 m telescope at ESO-La Silla observatory. 23

2.6 Finding chart for the globular cluster NGC 6715. The image used corresponds to the reference image constructed during the reduction. All known variables and new discoveries are labeled with their V numbers. Known variables, or new variables discovered in this work, are plotted with black symbols. Variables discovered by the OGLE survey are plotted with blue symbols. Those variables that were candidate variables from Montiel & Mighell (2010) are plotted using squares. Otherwise, symbols are circles. Green squares and red circles, both without labels, are candidate variables from Montiel & Mighell (2010) and McDonald et al. (2014) respectively for which we do not detect variability in our survey. Image size is $\sim 40 \times 40\text{arcsec}^2$. 28

3.1 Plot in galactic coordinates showing the 157 globular clusters (black points) so far known in our Galaxy. The clusters in colour correspond to those studied in this work. 31

3.2 Each box represents the histograms with the number of data taken during each year for the globular cluster NGC 6715. Thus, on the left is the 2013, in the middle 2014, and on the right 2015. 32

3.3 Standard I magnitude taken from the HST observations as a function of the instrumental $i' + z'$ magnitude. The red line is the fit that best matches the data and it is described by the equation in the title. The correlation coefficient is 0.999. 33

3.4 Root mean square (RMS) magnitude deviation (top) and S_B statistic (bottom) versus the mean I magnitude for the 1402 stars detected in the field of view of the reference image for NGC 6715. Coloured points follow the convention adopted in Table 3.1 to identify the types of variables found in the field of this globular cluster. 34

3.5 Zoom in to the central region of the globular cluster NGC 6715. On the left all the stars in the field covered are shown and variables stars are labeled in blue. On the right the stacked image is shown. Similarly, the position of the variable stars is given in blue. The spots at their positions correspond to the sum of the differential fluxes as given in Equation 3.2. . . . 35

3.6 Colour magnitude diagram for the globular cluster NGC 6715 built with V and I magnitudes available in the ACS globular cluster survey extracted from HST images. The variable stars are plotted in colour following the convention adopted in Table 3.1. 36

4.1 The number of RR Lyraes, mean periods, and number ratios as a function of the distance from the cluster centre. The red lines correspond to the tidal radii calculated by McLaughlin & van der Marel (2005). 43

4.2 (a) Light curves of the known and new variables discovered in globular cluster NGC 6715. Red, blue, and yellow triangles correspond to the data obtained during the years 2013, 2014, and 2015, respectively. For V229, V244, V246, V286-V291, we plot the quantity $f_{\text{diff}}(t)/p(t)$ since a reference flux is not available. 46

4.2 (b) Light curves of the known and new variables discovered in globular cluster NGC 6715. Red, blue, and yellow triangles correspond to the data obtained during the years 2013, 2014, and 2015, respectively. For V229, V244, V246, V286-V291, we plot the quantity $f_{\text{diff}}(t)/p(t)$ since a reference flux is not available. 47

4.2 (c) Light curves of the known and new variables discovered in globular cluster NGC 6715. Red, blue, and yellow triangles correspond to the data obtained during the years 2013, 2014, and 2015, respectively. For V229, V244, V246, V286-V291, we plot the quantity $f_{\text{diff}}(t)/p(t)$ since a reference flux is not available. 48

4.2 (d) Light curves of the known and new variables discovered in globular cluster NGC 6715. Red, blue, and yellow triangles correspond to the data obtained during the years 2013, 2014, and 2015, respectively. For V229, V244, V246, V286-V291, we plot the quantity $f_{\text{diff}}(t)/p(t)$ since a reference flux is not available. 49

4.3 Root mean square (RMS) magnitude deviation (top) and S_B statistic (bottom) versus the mean I magnitude for the 575 stars detected in the field of view of the reference image for NGC 104. Coloured points follow the convention adopted in Tab. 3.1 to identify the types of variables found in the field of this globular cluster. 51
4.4 Colour magnitude diagram for the globular cluster NGC 104 built with V and I magnitudes available in the ACS globular cluster survey extracted from HST images. The variable stars are plotted in colour following the convention adopted in Tab. 3.1. 52
4.5 Finding chart for the globular cluster NGC 104. The image used corresponds to the reference image constructed during the reduction. All known variables and new discoveries are labelled. Image size is $\sim 41 \times 41$ arcsec^2. 53
4.6 NGC 104: Light curves of the known and new variables discovered in this globular cluster. Red triangles correspond to the data obtained during the year 2013 and blue circles correspond to the data obtained during the year 2014. For EM7, we plot the quantity $f_{\rm diff}(t)/p(t)$ since a reference flux is not available. 53
4.7 Root mean square (RMS) magnitude deviation (top) and S_B statistic (bottom) versus the mean I magnitude for the 2616 stars detected in the field of view of the reference image for NGC 5139. Coloured points follow the convention adopted in Tab. 3.1 to identify the types of variables found in the field of this globular cluster. 54
4.8 Colour magnitude diagram of the globular cluster NGC 5139 built with V and I magnitudes available in the ACS globular cluster survey extracted from HST images. The variable stars are plotted in colour following the convention adopted in Tab. 3.1. 55
4.9 Finding chart for the globular cluster NGC 5139. The image used corresponds to the reference image constructed during the reduction. The new variables discovered are labelled. Image size is $\sim 41 \times 41$ arcsec^2. 55
4.10 NGC 5139: Light curves of the 3 new variables discovered in this globular cluster. Symbols are the same as in Fig. 4.6. 56
4.11 Root mean square (RMS) magnitude deviation (top) and S_B statistic (bottom) versus the mean I magnitude for the 1903 stars detected in the field of view of the reference image for NGC 5286. Coloured points follow the convention adopted in Tab. 3.1 to identify the types of variables found in the field of this globular cluster. 57
4.12 Colour magnitude diagram for the globular cluster NGC 5286 built with V and I magnitudes available in the ACS globular cluster survey extracted from HST images. The variable stars are plotted in colour following the convention adopted in Tab. 3.1. 59
4.13 Finding chart for the globular cluster NGC 5286. The image used corresponds to the reference image constructed during the reduction. All known variables and new discoveries are labelled. Image size is $\sim 41 \times 41$ arcsec^2. The image stamps are of size $\sim 4.6 \times 4.6$ arcsec^2. . 60
4.14 NGC 5286: Light curves of the known and new variables discovered in this globular cluster. Symbols are the same as in Fig. 4.6. 61
4.15 Amplitude-period diagram for the RR Lyrae stars in the globular cluster NGC 5286. 62
4.16 Root mean square (RMS) magnitude deviation (top) and S_B statistic (bottom) versus the mean I magnitude for the 1220 stars detected in the field of view of the reference image for NGC 6093. Coloured points follow the convention adopted in Tab. 3.1 to identify the types of variables found in the field of this globular cluster. 63
4.17 Colour magnitude diagram for the globular cluster NGC 6093 built with V and I magnitudes available in the ACS globular cluster survey extracted from HST images. The variable stars are plotted in colour following the convention adopted in Tab. 3.1. 64
4.18 Finding chart for the globular cluster NGC 6093. The image used corresponds to the reference image constructed during the reduction. All known variables and new discoveries are labelled. Image size is $\sim 41 \times 41$ arcsec^2. 65

4.19 NGC 6093: Light curves of the known and new variables discovered in this globular cluster. Symbols are the same as in Fig. 4.6. 66
4.20 Finding chart for the globular cluster NGC 6121. The image used corresponds to the reference image constructed during the reduction. The only known variable in the field is labelled. Image size is $\sim 41 \times 41$ arcsec^2. 67
4.21 NGC 6121: Light curve of the variable V21 in this globular cluster. Symbols are the same as in Fig. 4.6. 68
4.22 Root mean square (RMS) magnitude deviation (top) and S_B statistic (bottom) versus the mean I magnitude for the 843 stars detected in the field of view of the reference image for NGC 6541. Coloured points follow the convention adopted in Tab. 3.1 to identify the types of variables found in the field of this globular cluster. 69
4.23 Colour magnitude diagram for the globular cluster NGC 6541 built with V and I magnitudes available in the ACS globular cluster survey extracted from HST images. The variable stars are plotted in colour following the convention adopted in Tab. 3.1. 70
4.24 Finding chart for the globular cluster NGC 6541. The image used corresponds to the reference image constructed during the reduction. All known variables and new discoveries are labelled. Image size is $\sim 41 \times 41$ arcsec^2. 70
4.25 NGC 6541: Light curves of the known and new variables discovered in this globular cluster. Symbols are the same as in Fig. 4.6. 71
4.26 Finding chart for the globular cluster NGC 6656. The image used corresponds to the reference image constructed during the reduction. All known variables and new discoveries are labelled. Image size is $\sim 41 \times 41$ arcsec^2. 73
4.27 NGC 6656: Light curves of the known variables found in this globular cluster. Symbols are the same as in Fig. 4.6. 73
4.28 Colour magnitude diagram for the globular cluster NGC 6656 built with V and I magnitudes available in the ACS globular cluster survey extracted from HST images. The variable stars are plotted in colour following the convention adopted in Tab. 3.1. 74
4.29 Root mean square (RMS) magnitude deviation (top) and S_B statistic (bottom) versus the mean I magnitude for the 1315 stars detected in the field of view of the reference image for NGC 6681. The coloured point follows the convention adopted in Tab. 3.1 to identify the types of variables found in the field of this globular cluster. 75
4.30 Colour magnitude diagram for the globular cluster NGC 6681 built with V and I magnitudes available in the ACS globular cluster survey extracted from HST images. One variable star is plotted in colour following the convention adopted in Tab. 3.1. 76
4.31 Finding chart for the globular cluster NGC 6681. The image used corresponds to the reference image constructed during the reduction. All known variables and new discoveries are labelled. Image size is $\sim 41 \times 41$ arcsec^2. 76
4.32 NGC 6681: Light curve of the new variable discovered in this globular cluster. Symbols are the same as in Fig. 4.6. 77
4.33 Root mean square (RMS) magnitude deviation (top) and S_B statistic (bottom) versus the mean I magnitude for the 1258 stars detected in the field of view of the reference image for NGC 6723. Coloured points follow the convention adopted in Tab. 3.1 to identify the types of variables found in the field of this globular cluster. 78
4.34 Period-amplitude diagram for the globular cluster NGC 6723. The previously known RR Lyrae are plotted. 79
4.35 Colour magnitude diagram for the globular cluster NGC 6723 built with V and I magnitudes available in the ACS globular cluster survey extracted from HST images. The variable stars are plotted in colour following the convention adopted in Tab. 3.1. 79

4.36 Finding chart for the globular cluster NGC 6723. The image used corresponds to the reference image constructed during the reduction. All known variables and new discoveries are labelled. Image size is $\sim 41 \times 41$ arcsec^2. 80
4.37 NGC 6723: Light curves of the known variables in this globular cluster. Symbols are the same as in Fig. 4.6. 80
4.38 NGC 6752: Light curve of the variable V26 in this globular cluster. Symbols are the same as in Fig. 4.6. We plot the quantity $f_{\rm diff}(t)/p(t)$ since a reference flux is not available. 81

5.1 Globular cluster NGC 4590 observed with 3 different cameras. In (a) the field of view correspond to the ACS instrument at the HST and the small green box is the field shown in (d) for the same HST image, (b) for Las Cumbres Observatory camera, and (c) for the EMCCD at the Danish 1.54m telescope. PSF FWHM for (a) and (d) is 0.1″ to 0.14″, 1.49″ in (b), and 0.40″ in (c). 88

A.1 Each plot represents the histograms with the number of data taken for each globular cluster during the different observational seasons. The boxes correspond to each year. 96

B.1 Standard I magnitude taken from the HST observations as a function of the instrumental $i' + z'$ magnitude. The red lines are the fits that best match the data and they are described by the equations in the titles of each plot. The correlation coefficient is 0.999 in all cases. . . 98

List of Tables

1.1 Typical semi-empirical calibrations employed in the analysis of RR Lyrae stars through a Fourier decomposition of their light curves. 14

2.1 Time-series I-band photometry for all known and new variables in the field of view covered in each globular cluster. The standard $M_{\rm std}$ and instrumental $M_{\rm ins}$ magnitudes are listed in columns 5 and 6, respectively, corresponding to the cluster, variable star, filter, and epoch of mid-exposure listed in columns 1-4, respectively. The uncertainty on $M_{\rm ins}$ is listed in column 7, which also corresponds to the uncertainty on $M_{\rm std}$. For completeness, we also list the quantities $f_{\rm ref}$, $f_{\rm diff}$ and p from Eq. 2.11 in columns 8, 10 and 12, along with the uncertainties $\sigma_{\rm ref}$ and $\sigma_{\rm diff}$ in columns 9 and 11. This is an extract from the full table, which is available with the electronic version of the articles Figuera Jaimes et al. (2016b) and Figuera Jaimes et al. (2016a) at the CDS. 27

3.1 Convention used in the variable star classification of this work based on the definitions of the General Catalogue of Variable Stars (Samus et al. 2009a). Column 1 corresponds to the type of variability, Column 2 is the abbreviated name for the specific variability type, Column 3 is the shape of the point used to plot the variable, and Column 4 is the colour used to plot the point. 30

3.2 Some of the physical properties of the globular clusters studied in this work. Column 1, is the name of the cluster as it is defined in the New General Catalogue, Columns 2 and 3 are the celestial coordinates (right ascension and declination), Column 4 is the distance from the Sun, Column 5 is distance from the Galactic centre, Column 6 is metallicity, Column 7 is reddening, Column 8 is V magnitude level of the horizontal branch, Column 9 is V distance modulus, Column 10 is King-model central concentration c = $\log(r_t/r_c)$, Column 11 is central luminosity density $\log_{10}(L_\odot {\rm pc}^{-3})$, Column 12 is the mean full-width half-maximum (arcsec) measured in the reference image and Column 13 is the exposure time in the reference image. 31

4.1 Ephemerides and main characteristics of the variable stars in the field of globular cluster NGC 6715. Column 1 is the id assigned to the variable star, Column 2 is a previously known id assigned to the stars (5 digit numbers correspond to OGLE identifications of the form OGLE-BLG-RRLYR-*NNNNN*), Columns 3 and 4 correspond to the right ascension and declination (J2000), Column 5 is the epoch used, Column 6 is the period measured in this work unless the variable is an OGLE star in which case we use their period, Column 7 is median magnitude, Column 8 is the peak-to-peak amplitude in the light curve, Column 9 is the number of epochs and Column 10 is the classification of the variable. The numbers in parentheses indicate the uncertainty on the last decimal place of the period. 44

4.2 NGC 104: Ephemerides and main characteristics of the variable stars in the field of this globular cluster. Column 1 is the id assigned to the variable star, Columns 2 and 3 correspond to the right ascension and declination (J2000), Column 4 is the epoch used, Column 5 is the period, Column 6 is median of the data, Column 7 is the peak-to-peak amplitude in the light curve, Column 8 is the number of epochs and Column 9 is the classification of the variable. The numbers in parentheses indicate the uncertainty on the last decimal place of the period. . 50
4.3 NGC 5139: Ephemerides and main characteristics of the variable stars in the field of this globular cluster. Columns are the same as in Tab. 4.2. 54
4.4 NGC 5286: Ephemerides and main characteristics of the variable stars in the field of this globular cluster. Columns are the same as in Tab. 4.2. 58
4.5 NGC 6093: Ephemerides and main characteristics of the variable stars in the field of this globular cluster. Columns are the same as in Tab. 4.2. 63
4.6 NGC 6121: Ephemerides and main characteristics of one variable star in the field of this globular cluster. Columns are the same as in Tab. 4.2. 67
4.7 NGC 6541: Ephemerides and main characteristics of the variable stars in the field of this globular cluster. Columns are the same as in Tab. 4.2. 69
4.8 NGC 6656: Ephemerides and main characteristics of the variable stars in the field of this globular cluster. Columns are the same as in Tab. 4.2. 72
4.9 NGC 6681: Ephemerides and main characteristics of one variable star in the field of this globular cluster. Columns are the same as in Tab. 4.2. 75
4.10 NGC 6723: Ephemerides and main characteristics of the variable stars in the field of this globular cluster. Columns are the same as in Tab. 4.2. 78
4.11 NGC 6752: Ephemerides and main characteristics of one variable star in the field of this globular cluster. Columns are the same as in Tab. 4.2. 81

5.1 Fields that are needed in the headers of FITS files to be used by the DanDIA pipeline to be considered during the reduction procedure. 84
5.2 Parameters written in the light curve files for each of the stars detected by the DanDIA pipeline. 86
5.3 The intervals covered by several parameters of the 11 globular clusters are shown. Column 1 is the interval in metallicities, Column 2 corresponds to the interval covered in the magnitude level of the horizontal branch, Column 3 is for distance modulus, Column 4 for central luminosity density and column 5 for FWHM measured in the reference frames 89
5.4 Variables and magnitude ranges covered by our observations for the 11 globular clusters. Column 1 is the name of the globular cluster, Column 2 is the number of stars detected inside the field of view of our reference frame for each cluster, Column 3 is the number of epochs of our observations, Column 4 is the magnitude of the brightest star we detected, Column 5 is the magnitude of the faintest star detected, Column 6 is the range in magnitude covered by our observations, Column 7 is the number of previously known variable stars in the cluster (inside and outside our field of view), Column 8 is the number of new discoveries we made. 90

C.1 Cross identification between the RR Lyrae variables listed by the CVSGGC (Clement et al. 2001), the variable star candidates from Montiel & Mighell (2010), and the OGLE RR Lyrae stars (Udalski et al. 2015) 100

Chapter 1

Introduction

The first generation of devices used in astronomy to register the light emitted or reflected by stellar sources were photographic films. With those films and large telescopes, it was possible to study fainter objects than the eyes can see.

It was not until 1976 that the first astronomical CCD image was taken (Smith 1976), and not until the 1980's (Martinez & Klotz 1998) that the astronomy community started to use the Charge Couple Devices (CCDs) more widely as a new tool to obtain photometric images. A CCD is an electronic device consisting of a light-sensitive pixel array that can count the number of photons from the incoming light by converting them into electrons through a process called the photoelectric effect.

With the use of CCDs, many advantages could be obtained. For example, photographic films could only register around 1% of the photons that hit the emulsion. The response of the photographic film to light intensity is non-linear, so it was difficult to make quantitative measurements of the magnitude of stars. With CCDs, it is possible to obtain images with higher signal and in less exposure time than with photographic films. The final images obtained with CCDs are digital, so that, they are processed and analyzed in computers, and they can be duplicated any time needed just by clicking copy and paste. CCDs have a linear response to input intensity (constant gain) over a wide range.

High quality images are a very important aspect in astronomy (Léna 1996). This is one of the reasons astronomers started to build telescopes with bigger and bigger mirrors, with the aim of obtaining the highest resolution images that is possible. But, there is an important factor that always limits the quality obtained in the images. This factor is the **Earth's atmosphere**; The layers of the atmosphere, combined with turbulent effects inside it, can disperse the light of the stellar objects limiting the quality of the images. To avoid these atmospheric effects, astronomers have started to build space telescopes such as Hubble, Kepler, Spitzer, etc. As these telescopes are outside of the Earth's atmosphere, they do not have to deal with it. Excellent high-quality images have been obtained with space telescopes, and a lot of important discoveries have been made. But space telescopes are much more expensive than ground-based telescopes, their maintenance is more complicated, and lifetime much shorter. From ground-based telescopes, it was necessary to implement new technologies, as for example, adaptive optics (see e. g. Rousset et al. 1990; Wizinowich et al. 2000; Léna 1996), more modern CCDs (Jones 2006; Beletic & Amico 1998), and as we will discuss in this thesis, the use of Electron-Multiplying CCDs (Denvir & Conroy 2003; Tulloch 2003).

In general terms, EMCCDs are the conventional CCDs used in astronomy but as part of their electronics they have been equipped with a solid-state photo-multiplier and an extended gain register which is a row of pixels placed between the photo-sensitive area and the output node (see Chapter 2) configured with high and well very well defined voltages that make possible a probability that a new electron is created every time an electron touch a pixel in this register gain.

This makes it possible to produce an electron cascade when electrons move from the register row to the computer. That means many electrons can be detected above the noise level in very short exposure times

(milliseconds). These detectors can work at a frame rate of 10 to 100 images per second. Several studies, and as we will discuss in this work, show that due to the short exposure time in the acquired images, the effect of the atmosphere is mitigated. This technique has enabled astronomers to study many stellar objects with almost the same resolution as for example the *Hubble Space Telescope* (HST), among them the study of crowded stellar fields as we will show in the further chapters.

The study of globular clusters started a long time ago (Shapley 1918d). However, due to the crowded nature of these stellar systems, only their surrounding areas were possible to be properly studied rather than their cores. In Figure 1.1, we can see the field of view covered in Shapley (1918d) during his study of globular cluster NGC 5272 where all variable stars found in the cluster are in the external zones of the cluster and none in the center. The image shown was taken using photographic plates. A similar situation can be seen in Figure 1.2 of globular cluster NGC 6715 studied by Layden & Sarajedini (2000a), even though this study is much more recent in comparison with that of Shapley, and a CCD was employed, the limitation to studying the core of the cluster is evident. Again, variables were found only in the surrounding areas of the cluster. More recently, the implementation of new mathematical techniques employed to analyze the images such as difference image analysis and the implementation of new technologies such as adaptive optics have helped to study the core of globular clusters in better ways (see e. g. Salinas et al. 2016).

In a similar vein, more recent studies where globular clusters have been observed with new technology cameras such as the EMCCD to test and quantify the improvements of this technology and the methods employed in crowded fields are found in the literature (Law et al. 2006; Mackay et al. 2004; Díaz-Sánchez et al. 2012; Mackay 2013). However, it was not until this study that the planning and carrying on of a programme exclusively dedicated and optimized to the study of variable stars in the crowded core of globular clusters was done.

As we will see the implementation of using EMCCDs can be explained by analyzing images that were taken in crowded starfields in conventional ways, such as the Milky Way center and globular clusters centers. It is possible to note that many of the stars in the image center are blended. That means it is not possible to distinguish the flux of each star, and as a consequence, those stars cannot be studied, or cannot be studied properly. If some of the stars that are blended are intrinsic variables, their variability information is lost. Although the blending and the atmospheric effect continue being issues to deal with, the implementation of methods such as Difference Image Analysis (DIA) has shown to work well in crowded fields.

In this modest study, we will focus on producing images with the highest resolution possible to be able to do a proper exploration of the very crowded core of globular clusters in our Galaxy. The study of these stellar systems has been historically relevant in astrophysics. We will show the benefits of using EMCCDs and the shift-and-add technique combined with DIA to overcome the blending between stars and saturation issues in the brightest stars and perform a proper photometric measurement of the fluxes in each of the stars in the fields observed. Finally, we will employ some statistical techniques to automatically (or semi-automatically) detect variable stars in the globular clusters and we will characterize and classify them to update the variable star population in those stellar systems. A discussion about variable stars and their use as tools to determine physical parameters of the clusters they belong to is also given.

High precision photometry in crowded fields is a very challenging task, blended stars degrade the information that could be obtained from these stellar sources, saturated stars in crowded fields can affect the PSF models used to extract the photometry of surrounding stars, and the fainter stars are less likely to be detected if they are blended with brighter stars. Additionally, in the case of globular clusters, the information of variable stars in their cores can completely be lost; multiple stellar populations in crowded regions might not be detected; information related to the possible presence of intermediate-mass black holes in their centers can be lost completely. Finally, globular clusters are known to host exotic stellar populations as results of the high densities in their cores (See e. g. Knigge et al. 2008). Due to this, high-resolution imaging is a vital key to expanding the frontiers of our knowledge on globular clusters.

Thus, Chapter 2 describes the differences between conventional CCDs and EMCCDs and the procedures employed to do the reductions and photometry extraction, Chapter 3 makes an extensive analysis of the stars in the field of eleven globular clusters for variable star detection, Chapter 4 summarises the main results

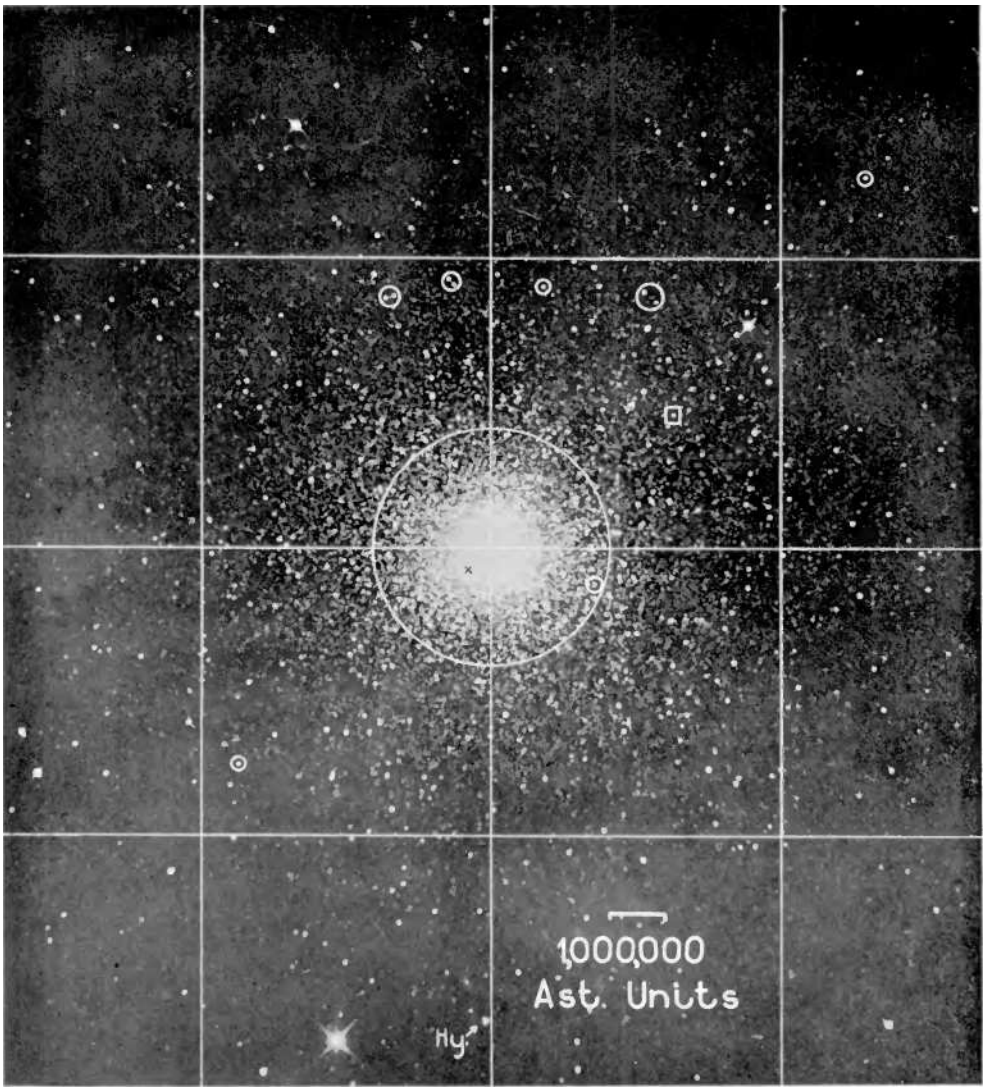

Figure 1.1: Field of view of globular cluster NGC 5272 studied by Shapley (1918d). As seen in the image, the core of the cluster appears crowded in the images and it was only possible to detect variability in their surrounding areas. Small circles are variable stars found in the cluster. This study was done using photographic plates.

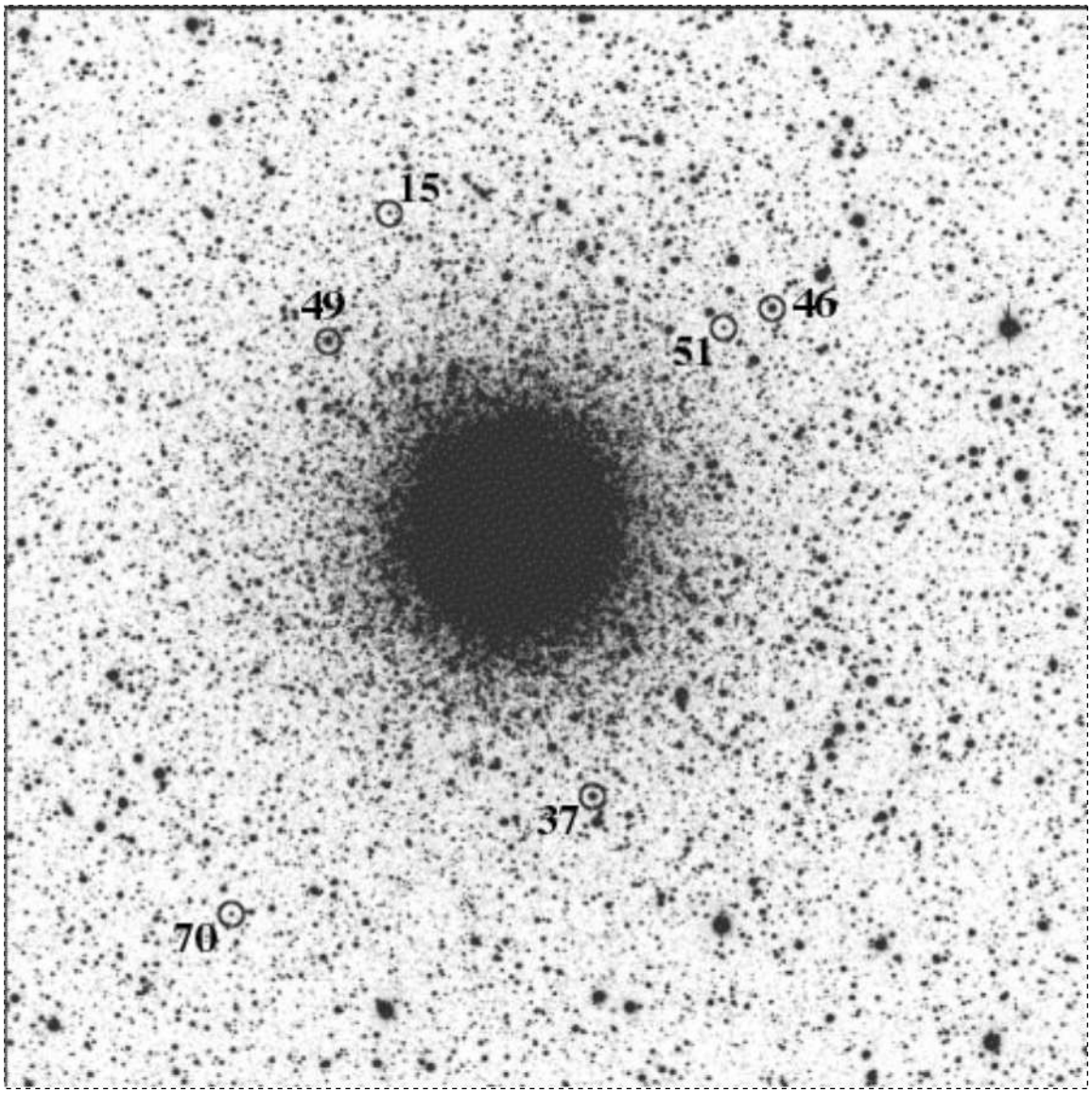

Figure 1.2: Field of view of globular cluster NGC 6715 studied by Layden & Sarajedini (2000a). Again, the core of the cluster appears crowded in the image and it was only possible to detect variability in the surrounding areas. Small circles are variable stars found in the cluster. This study was done using a CCD.

obtained in this work, and finally, Chapter 5 contains the discussions and conclusions.

1.1 Importance of globular clusters

In comparison with our Galaxy, globular clusters are small stellar systems with a diameter between 20 to 100 pc and a number of stars of 10^4 to 10^5. They are formed by hundreds of thousands of stars gravitationally bound to form the cluster itself. These stars were formed more or less at the same time and more or less with the same chemical composition. They orbit in the halo of the Milky Way, they have high spherical symmetry, and most of them have a high concentration of stars toward their centers (Abell 1982; Ashman & Zepf 1998; Martínez Roger et al. 1999).

Due to their nature of having a high concentration of stars in their center (up to at least 10^6 $M_\odot$, Knigge et al. 2008), it makes them excellent candidates to do studies and analysis of crowded starfields as will be shown in further chapters. They are good to test new technologies such as CCDs, new photometric measurement techniques such as DIA, and can be used to test studies related to the blending of stars, among others.

Even though globular clusters were formed more or less at the same time and more or less with the same chemical composition and share similar properties, they are not so identical and there are properties in which they differ between each other. A compilation of the main properties and characteristics of globular clusters is found in the Catalog of Milky Way Globular Clusters (Harris 1996, 2010 version). Thus, the reader will find physical parameters such as the metallicity, the abundance of elements heavier than hydrogen and helium, of the clusters as given in Equation 1.1.

$$[\mathrm{Fe/H}] = \log(\mathrm{Fe/H})_* - \log(\mathrm{Fe/H})_\odot, \tag{1.1}$$

the abundance ratio of iron to hydrogen of the stars (*) are measured respect to the abundance ratio of iron to hydrogen of the sun ($\odot$) (Binney & Merrifield 1998). Values of metallicity listed in Harris (1996, 2010 version) spread between -2.31 to 0.0 dex. Thus, if a cluster has a metallicity [Fe/H]=-1.00 dex (e. g. Terzan 10), then the cluster is 10 times poorer in metals than our Sun. In a similar vein, the reader will see values as the central luminosity density ρ_0 of the clusters, the definition of which is given by Djorgovski (1993):

$$\rho_0 = \Sigma_0/(r_c p). \tag{1.2}$$

Here Σ_0 is associated to the central surface brightness as: $\log \Sigma_0 = 0.4[26.362 - \mu_v(0)]$, $\mu_v(0)$ is the central surface brightness, r_c is the core radius, and p is a dimensionless parameter that depends on the cluster concentration. This parameter is particularly interesting because it was used in our work to select globular clusters with different types of a concentration of stars in the core with the aim of testing our techniques in clusters with different levels of crowdedness. In Figure 1.3 the histogram of ρ_0 listed in Harris (1996, 2010 version) is shown. It shows that the distribution of clusters spread between -0.97 to 6.06 dex (left and right blue lines, respectively) peaking to a maximum at 3.63 dex which is very close to the mean central luminosity density of 3.44 dex (middle blue line) calculated for all the clusters. It is possible to see that the majority of the clusters have values of ρ_0 between 2.5 - 6 dex while only 26 clusters have values of ρ_0 <2.5 dex giving us a reference that most of them are crowded systems.

Globular clusters host the oldest stars in the Galaxy, in this context, they are like fossils of the early Galaxy formation and evolution. They also host a lot of stars in different evolution stages (Ashman & Zepf 1998; Martínez Roger et al. 1999). In Figure 1.4 the Hertzsprung-Russell diagram for globular clusters is shown in its luminosity versus spectral type version. The diagram covers the evolution of each of the stars at its current evolution stage starting in the main sequence (MS) which is the first position in the life-cycle of the stars after the radiative equilibrium is reached and the hydrogen fusion started in their core. After the hydrogen in the core of the stars is consumed they move toward the main sequence turn off point (TO) and finally leave it toward the red giant branch (RGB) when all hydrogen is exhausted and a new core

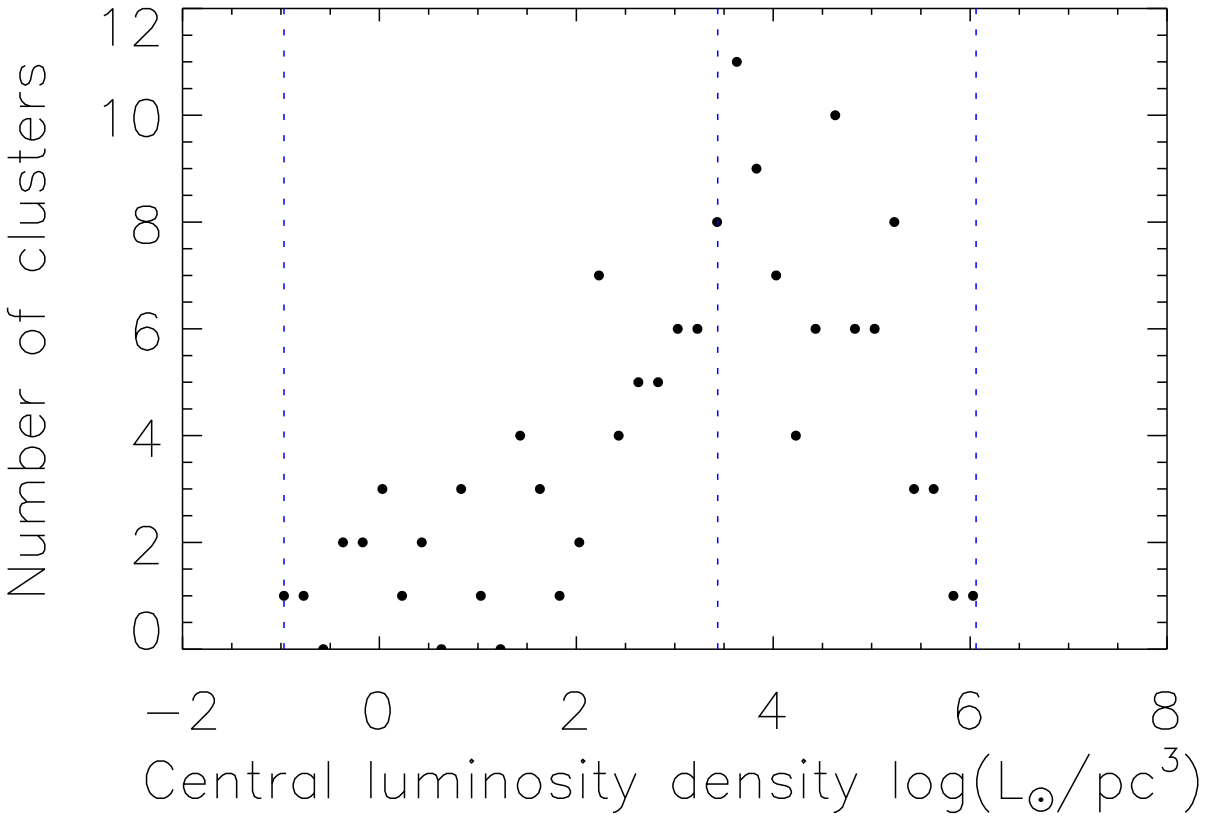

Figure 1.3: Histogram of the central luminosity density for globular clusters listed in Harris (1996) built with a binning of 0.2. The vertical lines correspond to the minimum, mean, and maximum values, respectively.

formed with helium surrounded by a burning hydrogen shell is obtained. Once the helium core obtains the proper temperature the fusion starts again (Helium-flash) by the triple-alpha process and the stars move to the horizontal branch (HB). The position in the HB will depend on the amount of mass lost in the envelope of the stars during their time in the RGB and the stars could be placed in the instability strip of the horizontal branch where the star will be a pulsating RR Lyrae variable. However, the stars could also be placed in what is known the blue horizontal branch (BHB) which is a region on the left end of the horizontal branch or in the red horizontal branch (RHB), which is a redward section of the HB. The position of the stars in the horizontal branch is known to depend on metallicity, usually known as the first parameter, but it was found that globular clusters with similar metallicities have different HBs, thus it was necessary to think in the idea of a second parameter which is thought to be the same age of the clusters, also their total masses. It was found that cluster density and concentration correlate with the position of the stars to the blue part. It also has been thought that a third parameter is the He abundance or self-enrichment which variations could explain the shape of the HB (Milone 2013; Gratton et al. 2010, and references therein). The stars during their time in the HB will produce carbon and oxygen by burning helium in the core but also will be producing helium in the external shell by burning hydrogen. Once all the helium is exhausted in the core the stars then will move to the asymptotic giant branch (AGB) where they will have a carbon-oxygen core surrounded by a burning helium shell and more externally by a burning hydrogen shell. Finally, the stars in the AGB will start to lose mass in the form of stellar winds to become a white dwarf (WD) in the central region surrounded by a planetary nebula and will move down in the CMD parallel to the faintest region of the MS. The diagram in Figure 1.4 also shows the blue stragglers region, which corresponds to MS stars that increased their masses in times after their formation. They are associated with binary systems and stars that suffered collisions and due to the increase of their masses, they look bluer in the HRD. The reader can also check the Encyclopedia of Astronomy and Astrophysics (Murdin 2001) for a general review or can go directly to Ashman & Zepf (1998), Binney & Merrifield (1998), Martínez Roger et al. (1999), Hansen et al. (2004), and Kippenhahn et al. (2012) for a deeper review.

1.2 Types of variables in globular clusters

Thanks to previous studies on globular clusters we know today that also variable stars are part of the stellar population that belong to the clusters. Due to the high number of stars and the wide range of evolutionary stages found in globular clusters, it is not rare that lots of different types of variable stars are found among them.

A compendium of variable stars has traditionally been kept in the Catalogue of Variable Stars in Galactic Globular Clusters (Sawyer 1939; Clement et al. 2001). In the last review in (Clement et al. 2001) they found that only considering variable stars with known periods, 1842 stars were RR Lyrae, 117 SX Phoenicis, 117 Semi-regulars or red variables, 96 eclipsing binaries, and 60 Cepheids (including population II Cepheids and RV Tauri stars).

1.2.1 RR Lyrae

RR Lyrae stars are the most common type of variables so far known in globular clusters (Clement et al. 2001). They are placed in the instability strip of the horizontal branch. They have a burning helium core surrounded by a burning hydrogen shell. They are pulsating stars with spectral type A to F and amplitude variations in V around 0.2 to 2 mag (Samus et al. 2009a).

According to their pulsation variation, light curve shape, period, and amplitude, RR Lyraes are classified into three groups:

RRab (RR0) stars which have radial pulsations in the fundamental mode with periods from 0.3 to 1.0 d and amplitudes in V from 0.5 to 2 mag. They have a very asymmetric light curves.

RRc (RR1) stars present radial pulsations in the first overtone with periods shorter than those in RR0 stars between 0.2 to 0.5 d and amplitudes in V shorter than 0.8 mag.

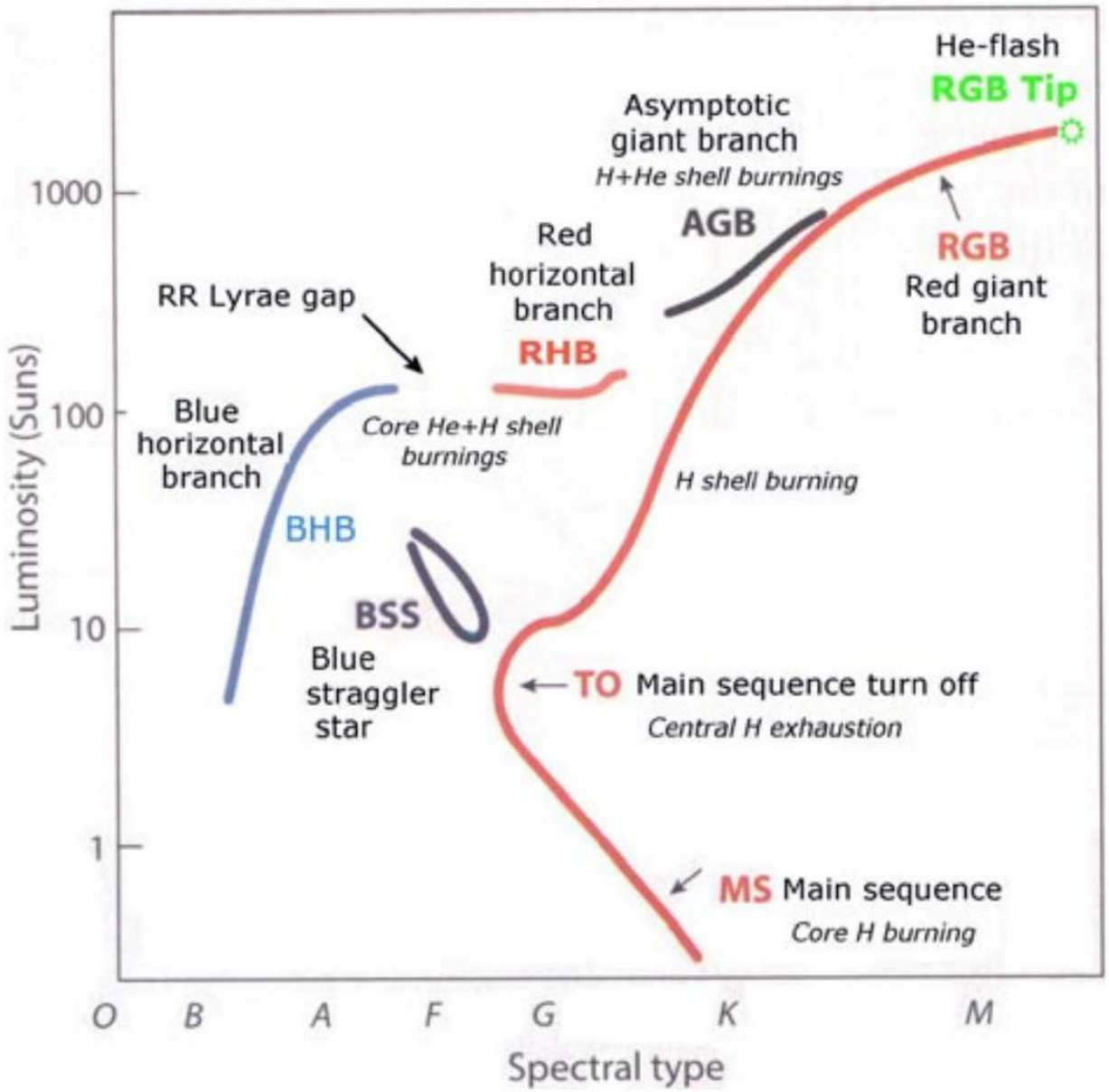

Figure 1.4: Hertzsprung-Russell diagram for globular clusters. Image taken from Enciclopedia of Astronomy and Astrophysics

RRb (RR01) variables are basically a combination of the previous two cases showing two simultaneously operating pulsation modes, the fundamental tone with the period P0 and the first overtone, P1. The ratio P1/P0 is approximately 0.745.

Due to the pulsation behavior of the RR Lyrae stars, Alcock et al. (2000) found it necessary to implement the RR0, RR1, and RR01 notation in their research rather than using the original designation. Later, this new designation was also adopted by (Clement et al. 2001) in the Catalogue of Variable Stars in Galactic Globular Clusters. Finally, it became the designation in most subsequent works including this thesis.

Some of the RR Lyrae stars are known to have a peculiar behavior. This peculiarity can be detected in the light curve of these stars because they present a variation in their amplitudes and in their period. So if these variations are periodic, then it is said that the RR Lyrae star has Blazhko effect. This is not a well-understood effect, however, it is thought to be associated with the inclination of the magnetic field of the star respect to its rotational axis. It is also thought to be associated with resonances between the fundamental mode and first overtone, that it could be associated with cycles in the convection zones of the stars (Blažko 1907; Smith 2004).

1.2.2 SX Phoenicis

The SX Phoenicis stars are pulsating variables in the blue straggler zone of the CMD. As commented before in this section, these stars are main sequence stars that increased their masses in times after their formation. The increase in their masses also increased their temperature making them look hotter and bluer than the other stars in the main sequence. Due to this, they appear as an extension of the main sequence past the turn off point. The instability strip also crosses this region of the color-magnitude diagram, then these variables are pulsating and are called SX Phoenicis. They are spectral types in A2-F5 and their periods are around 0.03 to 0.08 d and diverse amplitudes sometimes reaching 0.7 mag in V. These stars can be found pulsating in the fundamental mode, in the first overtone, in both, or multiple of them.

Similar to RR Lyrae, the pulsation properties of these stars have found to be very useful in the study and better understanding of the blue straggler structural parameters, especially their mass (Fiorentino et al. 2015) but also to determine their distance and that of the stellar systems they belong to such as globular clusters and dwarf galaxies (Fiorentino et al. 2015).

1.2.3 Pulsating red giants

These are stars at the top-right of the color-magnitude diagram and they belong to the red giant or asymptotic giant branch with intermediate or late spectral type. Depending on their periods, amplitudes, and light curve shapes they are divided into semi-regular, irregular, and Mira variables.

Semi regular

As their name points out they show semi-regular variability in their light curves which are associated with some periodicity and several amplitudes. They are subdivided into SRA, SRB, and SRC with spectral type M, C, S or Me, Ce and Se. Their periods range between 35-1200 d, 20-2300 d, and 30 to several thousand days, respectively. Amplitudes vary and can reach over 1 mag in V. Among the semi-regulars there is another type the SRD, but in this case, the stars present spectral types F, G or K and their amplitudes and periods range between 0.1-4 mag and 30-1100 d, respectively.

Irregular

These type of stars do not show any type of regularity or periodicity in their light curves. Usually, any type of a variable at the top of the red giant branch that was not possible to properly characterize is labelled as irregular with the symbol L. Slow irregular variables with spectral type K, M, C, and S are labeled as LB and irregular supergiants with late spectral type and amplitudes of around 1 mag are labeled as LC.

Mira

The Mira variables are characterized to be pulsating in the fundamental mode with periods between 80 to 1000 days with very well defined light curve shapes and amplitudes in V between 2.5 to 11 mag with spectral types Me, Ce and Se. Probably the ones with the highest amplitude and masses between 0.6 and a few solar masses. So far, there are no more than 10 Mira variables known in globular clusters.

1.2.4 Eclipsing binaries

Eclipsing binary stars as the name suggests are systems formed by two stars that are orbiting around their mass center as in a two-body problem. Usually, these stars are classified following three criteria (Samus et al. 2009a): Shape of the light curve, physical and evolutionary characteristics of their components, and degree of inner Roche lobe filling. The variation in their magnitudes does not correspond to intrinsic physics behavior of the stars itself but to geometrical effects produced when one of the stars in the binary system is passing in front of the other. It makes their total brightness decrease during the eclipse and then recover once the eclipse is over. From the light curve shapes of eclipsing variables it is possible to determine the size, temperature, and luminosity of the two stars, and if the inclination (i) between the orbit and the plane of the sky is known from spectroscopic observations, then it is possible to determine their masses (Percy 2011).

1.2.5 Cataclysmic variables

Cataclysmic variables are basically binary systems that are close enough to exchange material but not so close to merge with each other. These close binary systems, are usually formed by a compact object such as a white dwarf, a black hole or a neutron star - the main star - and the main sequence star - the secondary star. Their variability is associated with eruptive and abrupt changes in their magnitude and light curves shapes. The reason for their variability is related to the fact that the secondary star fills its Roche lobe and starts to transfer material to the accretion disk of the main star. Thus, the shape of their light curve variation depends on how the material impacts the accretion disk and it is ejected (outburst), the geometry of the system and all the physics processes occurring between the stars (Samus et al. 2009a; Percy 2011).

The General Catalogue of Variable Stars (Samus et al. 2009a) contains the detailed classification of these objects according to their periods, amplitudes, light curve shapes, and spectroscopic signatures, however, all cataclysmic variables, are associated with explosive, novae, and supernovae events.

Novae

Novae are cataclysmic variable stars from which a nova outburst has been observed. Nova outbursts are thermonuclear runaways on the surface of the accreting white dwarf star. Here fresh hydrogen-rich fuel from the binary builds up to the point at which a thermonuclear runaway occurs. Novae are evolved stars with orbital periods from 0.05 - 230 days that increase their visual magnitude up to 15 mag. Although the outburst can be detected and observed easily when there is not much absorption due to the high increased magnitudes, there is no clear understanding about their behavior before the outburst usually know as the prenova stage. There is a correlation between the absolute magnitude M_V of a Nova and the time it takes for its maximum brightness to go down 3 mag. This time is known as the t_3 parameter as shown in Equation 1.3

$$M_v = -12.25 + 2.66 \log(t_3). \tag{1.3}$$

Using Equation 1.3, once the t_3 parameter is known, is possible to determine the absolute magnitude of the novae and therefore its distance. They also show ultraviolet (UV) radiation, after the outburst begins, the temperature of the star very inside its expanding photosphere increases considerably that most of the energy is released in the UV. Additionally, the dust formed by the gas that is expanding around the stars absorbs the visible and UV radiation which is then emitted in the infrared (IR). During the prenova, absorption lines of a G-M type star will be seen and broad emission lines of H, He I and He II, and Ca II and a blue continuum

from the accretion disk. But instead, during the maximum, absorption lines similar of an A-F type supergiant will be seen but blue shifted by hundreds of km/s. Finally, the postnova stage will be similar to the prenova. For a more detailed description see Percy (2011) and Samus et al. (2009a).

Supernovae

The supernovae are very evolved stars that increase their magnitude strongly to about 20 mag. and even more during this stage known as the supernova in which the core of the star has exhausted its nuclear fuel and collapses to nuclear density. Contrary to the novae, where the increase in brightness can be recurrent, in the supernovae this is the last stage in the life of the star with a nuclear fusion core. After this explosion, what is left is a core collapsed into a neutron star or a black hole surrounded by an expanding shell produced by the explosion known as the supernova remnant that will expand at several thousands of km/s. As their maximum absolute magnitudes can be calibrated they are also used as distance indicators. According to their light curve shape and spectral characteristics, they are classified into two groups, the supernovae type I (SNI) and supernovae type II (SNII). The SNI will present absorption lines of Ca II, Si, etc., but no hydrogen perhaps only a little in their expanding remnant. After 20 or 30 days of peaking the maximum in their brightness, their magnitude will decrease about 0.1 mag per day and then become a constant value of 0.014 mag per day. The SNII will present hydrogen lines and other elements in the spectra but in this case, the expanding shell will be mainly of H and He. After the maximum brightness, it will take about 40 to 100 days for the bright to decrease at a rate of 0.1 mag. per day.

U Geminorum

These type of stars are also part of the cataclysmic variables sub-classification and are also known in the literature as **dwarf novae**. They are very interesting close binary systems as both of the stars have some peculiar behavior. From one side one of the stars in a dwarf or subgiant K-M star that fills its Roche lobe and from another side a white dwarf with an accretion disk. Their orbital periods range from 0.05 to 0.5 days with brightness suddenly increasing by up to 6 mag with an irregular periodicity of a few weeks.

The U Geminorum type stars are sometimes called in the literature dwarf novae (DNe) stars. The dwarf nova outbursts are caused by an increase in the accretion rate onto the white dwarf accretion disk instability associated with ionisation of hydrogen. Similar to the Novae, they also follow a relation between their amplitude A and the time t in days of the outburst as shown in Equation 1.4

$$A = 0.80 + 1.667 \log(t). \tag{1.4}$$

Spectroscopically speaking, the spectra of these stars are similar to those seen in novae but with a lack of emission lines at their maximum brightness. They also show a P Cygni profile during their outburst. Depending on their light curve shapes they are subdivided in SS Cygni- (SS Cyg), SU Ursae Majoris- (SU UMa), and Z Camelopardalis- (Z Cam) type variables (see Samus et al. 2009a; Percy 2011, for a detailed description).

1.2.6 Cepheid variables - W Virginis stars

The population II Cepheids, are old and low mass stars from 0.5 to 0.6 $M_\odot$ (Percy 2011) and periods that range from 0.8 to 35 days with amplitudes from 0.3 to 1.2 mag in V (Samus et al. 2009a). Although most of them are between 10-20 days (Percy 2011) they are classified as CWA for stars with periods longer the 8 days which are referred as W Virginis stars and CWB for stars with periods shorter than 8 days which are referred as BL Herculis stars. Some of them are found in the old disc of the Galaxy (Percy 2011) but tend to be found further from the Galactic plane as for example in globular clusters where so far there are 60 of these stars known (Clement et al. 2001). They follow a period-luminosity relation and luminosity, temperature, chemical composition, and age of these stars can be independently determined. There is a group of so far 47

stars that are classified as **"anomalous cepheids"** (Percy 2011). These stars look like W Virginis but their masses are of the order of 1.5 $M_{\odot}$. It is thought that they are either very young stars or they are merged binary stars. These stars are also referred as BLBOO variables after the star BL Bootis found in NGC 5466.

1.2.7 RV Tauri stars

These are pulsating stars of the yellow supergiant class with spectral types F-G at maximum light and K-M at minimum (Samus et al. 2009a). Their light curves have double waves as in the case of a star having two periods with ranges from 30 to 150 days (Percy 2011) with amplitudes of 3 - 4 magnitudes in V. They are classified in two types, the RVA which do not vary in mean magnitude and the RVB which do vary in mean magnitude periodically with periods between 600 to 1500 days (Samus et al. 2009a).

1.3 What can be learned from the variables and why they are important

Historically variable stars have been important in astrophysics because in some of them the periodic variability and mean magnitude (which do not change with the time) are related. It makes them standard candles to calculate their distances. It was Leavitt & Pickering (1912) who first discovered the period-luminosity relation for Cepheid variables with photographic observations of the Small Magellanic Cloud (SMC), afterward calibrated by Hertzsprung (1913) and the first distance calculation to the SMC was attempted. Shapley (1918b) also worked on the determination of distances to cepheid variables and later Hubble (1925) discovered a group of Cepheids in galaxies M31 and M33 and by applying the period-luminosity relation determined how far these systems are (see a review in Fernie 1969).

1.3.1 Oosterhoff type

Oosterhoff (1939) noticed that the mean period of RR0 stars changes depending on the clusters observed and found what is known today as the Oosterhoff classification of globular clusters, Oosterhoff type or Oosterhoff dichotomy.

As commented below in Section 1.3.2, it was found that the period of RR Lyrae stars is correlated with their amplitudes. With the study of this behavior in a diverse sample of globular clusters, Oosterhoff (1939) found that the mean period of RR Lyrae stars changed depending on the clusters observed. It turns out, that globular clusters can be classified into two groups based on the mean periods and the number ratios of their RR0 and RR1 stars.

There have been debates about possible explanations of this RR Lyrae behavior with their evolution stages, metallicity, and the connexion with physical properties of globular clusters. Thus, the spectroscopic study carried out by Preston (1959) for RR Lyrae stars appeared to show a separation in amplitude for RR Lyrae between metal-poor and metal-rich stars. This result is supported by Dickens & Saunders (1965) in their RR Lyrae study in Omega Centauri and Dickens (1970) in NGC 6171. After that, Sandage (1981) in the study of the period-luminosity-relation of RR Lyrae in six globular clusters (M3, M4, M15, NGC 6171, NGC 6891, and ω Cen) found a $\Delta \log(P)$ correlation for the RR Lyrae in each cluster and the RR Lyrae metal abundance (see a more detailed discussion in Clement & Shelton 1999).

Clement & Shelton (1999) also explored the period-amplitude relation for RR Lyrae variables in globular clusters M107, M3, M4, M5 (Oosterhoff I type) and M9, M68, and M92 (Oosterhoff II type) with CCD photometric data already available in the literature for the V filter. They took into consideration that there are RR Lyrae stars that could have the Blazhko effect and their mean periods and amplitudes could affect the real distribution of these variables in the Bailey diagram. To avoid these stars, they used the Jurcsik & Kovacs (1996) test to detect which RR Lyraes were having it. In their analysis, they considered that the period-amplitude relation for RR0 stars does not depend on metallicity but instead it depends on their evolutionary stage and that there may be a P - A relation for ZAHB stars and another for more evolved stars while in RR1 stars in OoI clusters depends on metallicity.

In a similar vein, Lee & Carney (1999) compared two globular clusters which have similar metallicity ([Fe/H]) and helium abundances but different Oosterhoff type. Those clusters are M2 (OoII) and M3 (OoI). Their metallicities are [Fe/H]= −1.62 and −1.66 dex, respectively. However, they have different HB morphologies $(B-R)/(B+V+R)$= 0.92 for M2 and 0.08 for M3. In this research, they explore four questions. Do RR Lyrae variables with similar metallicities in different Oosterhoff classes have the same luminosity?. Are the differences of these two types related to RR Lyrae evolution stages?. If so, what leads to such differences?. If Oosterhoff classes differ in ages, do they differ in origin as well?. To address these questions they calculated the period shift $\Delta\log(P)$ between M2 and M3 and by using Equation 1.5 of van Albada & Baker (1971)

$$\log(P_0) = -1.772 - 0.68\log\left(\frac{M}{M_\odot}\right) + 0.84\log\left(\frac{L}{L_\odot}\right) + 3.48\log\left(\frac{6500}{T_{eff}}\right). \tag{1.5}$$

They were able to calculate the differences in luminosity of the two clusters assuming same mass and effective temperatures for the RR0 stars. They compared the period shift of M2 with other OoI (NGC 5986) and OoII (NGC 3201 and NGC 7006) clusters for which the metallicities are similar. The main conclusion in their work is that the period shift analyses indicate that the OoII clusters M2 and NGC 5986, have similar RR Lyrae luminosities and both clusters' variables are more luminous than those of Oosterhoff I having similar metallicities.

In this part, Lee & Carney (1999) considers that the differences in luminosity between M2 and M3 are due to differences in the HB evolutionary stages of the stars arguing that their position of the HB branch is related to the mean mass and the mass loss at their time in the red giant tip, as mass loss can produce bluer HBs. Also consider that stars become more luminous when they evolve away from the ZAHB and that this is the case of M2 which has a bluer horizontal branch morphology and a higher period change rate of its RR Lyrae in comparison with those in M3. Additionally, they consider that these evolutionary differences are due to differences between the age of the clusters. The work explains that older GCs have bluer HBs at fixed chemical composition. Thus, RR Lyrae in an older BHB cluster would be more evolved, with faster periods and higher luminosities as the case of M2 respect to M3 and that this is congruent with the age calculation done for these clusters as he found that M2 is 2 Gyr older than M3 by adjusting synthetic isochrones to the colour-magnitude diagrams of the clusters. Recent reviews, argue that the metallicity of the clusters plays an important role in this classification and that it could be related with the formation history of the Galactic halo (see e.g. discussions in Lee & Carney 1999; Catelan 2004, 2009; Smith et al. 2011; Sollima et al. 2014).

1.3.2 RR Lyrae

RR Lyrae stars also follow a period-luminosity relation. They are the most common variables known in globular clusters, they are also commonly found in other stellar systems, and in the field of the Galaxy. The first variable star of this type was discovered by Wilhelmina Fleming (Pickering et al. 1901) in the Lyra constellation and one of the known pioneers in the study of globular clusters was Harlow Shapley, he was the first who attempted to determine the first distances to these stellar systems (Shapley 1918a,c, 1917). Nowadays several semi-empirical calibrations have been employed using RR Lyrae stars and other interesting physical parameters can be determined such as metallicity and effective temperature. It is done through a Fourier decomposition of their light curves and the use of their amplitudes, phases, and periods (see Figure 1.5). In Equation 1.6,

$$m(t) = A_0 + \sum_{k=1}^{N} A_k \cos\left[\frac{2\pi k}{P}(t-E) + \phi_k\right], \tag{1.6}$$

the Fourier analysis used for the analysis of the light curve data is shown. A_0 is the mean magnitude of the RR Lyrae, E is the epoch used, P is the period of the variability, ϕ_k and A_k are phases and amplitudes of the k^{th} harmonics, N is the total number of harmonics used in the fit, and $m(t)$ is the magnitude at the given time

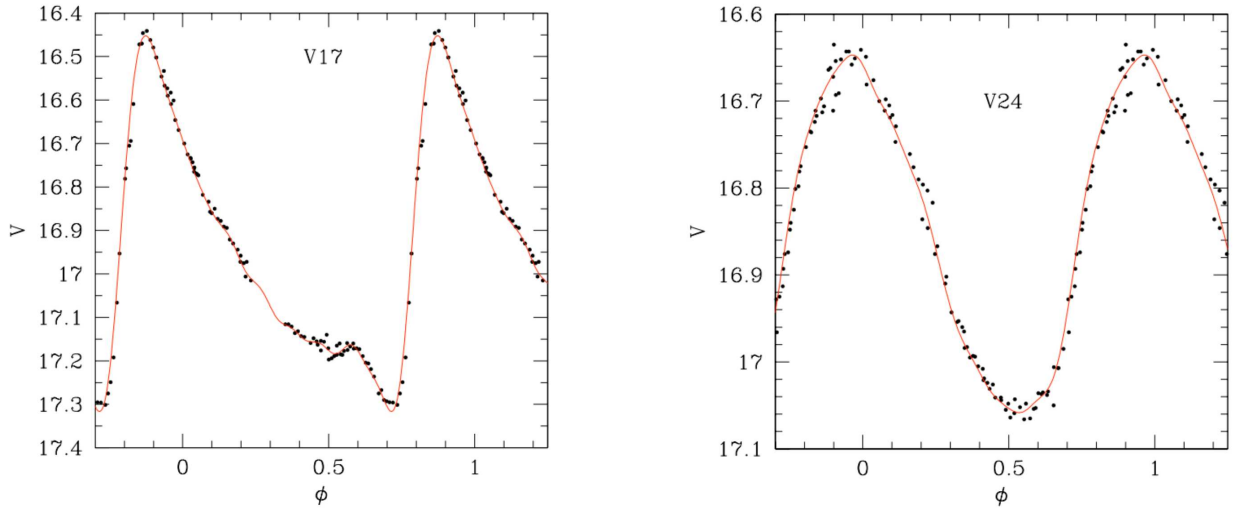

Figure 1.5: Light curves of two RR Lyrae stars in globular cluster NGC 6981. On the left a RR0 type is shown and of the right a RR1 type. The red lines correspond to the fit obtained with a 10 harmonics in the Fourier analysis of Eq. 1.6.

t. The terms

$$R_{ij} = A_i/A_j$$

$$\phi_{ij} = j\phi_i - i\phi_j$$

are known as the Fourier parameters and are used in the semi-empirical calibrations of RR Lyrae stars listed below.

Table 1.1: Typical semi-empirical calibrations employed in the analysis of RR Lyrae stars through a Fourier decomposition of their light curves.

Type	Calibration	Reference
	Metallicity	
RR0	$[\mathrm{Fe/H}]_J = -5.038 - 5.394P + 1.345\phi^s_{31}$	Jurcsik & Kovacs (1996)
RR1	$[\mathrm{Fe/H}]_{ZW} = 2.424 - 30.075P + 52.466P^2 + 0.982\phi^2_{31} - 4.198P$	Morgan et al. (2007)
	Effective Temperature	
RR0	$\log T_{\mathrm{eff}} = 3.9291 - 0.1112(V-K)_0 - 0.0032[\mathrm{Fe/H}]_J$	Jurcsik (1998)
RR0	$(V-K)_0 = 1.585 + 1.257P - 0.273A_1 - 0.234\phi^s_{31} + 0.062\phi^s_{41}$	Jurcsik (1998)
RR1	$\log T_{\mathrm{eff}} = 3.7746 - 0.1452\log P + 0.0056\phi_{31}$	Simon & Clement (1993)
	Absolute Magnitude	
RR0	$M_V = -1.876\log P - 1.158A_1 + 0.821A_3 + K_0$	Kovács & Walker (2001)
RR1	$M_V = -0.961P - 0.044\phi^s_{21} - 4.447A_4 + K1$	Cacciari et al. (2005)

RR Lyrae stars have been so useful to astronomy that they have even been employed in studies carried out with space telescopes. Brown et al. (2004) used the HST in a survey to study the Andromeda galaxy to produce a complete census of RR Lyrae stars in the halo of this system and used these stars to determine their distance, metallicity, and Oosterhoff type (See Section 1.3.2). Similarly, Nemec et al. (2011) did a research through a Fourier decomposition of RR Lyraes in the field covered by the Kepler telescope.

1.3.3 SX Phoenicis

Another group of stars that with the improvements of CCDs and telescopes are being frequently found and that can be used to also determine distances are the SX Phoenicis stars as they also follow a period-luminosity relation (see e. g. Jeon et al. 2003; McNamara 1995). More recently, Cohen & Sarajedini (2012) updated this relation using 77 double-mode SX Phe stars in Galactic globular clusters, which is of the form given in Equation 1.7

$$M_V = -1.640(\pm 0.110) - 3.389(\pm 0.090)\log(P_f) \tag{1.7}$$

where P is the fundamental period of the SX Phoenicis stars and and M_V is the absolute magnitude in the V band.

1.3.4 Eclipsing Binaries

Eclipsing binaries have been main targets in astrophysics and in the study of globular clusters (Kaluzny et al. 1998). It was thought that globular clusters were formed without primordial binaries, binaries that were formed once there was no more gas in the surroundings (Kouwenhoven et al. 2005). However, nowadays we know that they are widely found in globular clusters (Clement et al. 2001) and that their occurrence frequency could even be compared with that found in the Galactic disk (Hut et al. 1992). It makes it necessary to rethink about the formation processes and evolution of globular clusters. An example, can be found in Goodman & Hut (1989) where they propose that the energy needed to re-expand the cluster after the core collapsed could be obtained from primordial binaries. A similar study using N-body simulations was done by (Tanikawa & Fukushige 2009, and references therein), they also summarise several studies which point out the importance of considering binaries in the dynamical evolution of globular clusters as binaries supply energy through interaction with other stars even if the cluster does not have binaries in their early stages as they can be formed through three-body encounters. They also point out that if the clusters have an important fraction of primordial binaries the dynamical evolution of the clusters can be affected as shown in Goodman & Hut (1989). Finally, Tanikawa & Fukushige (2009) remark that it is possible to properly determine the population of primordial binaries in globular clusters by estimating mass fraction, distribution of binding energies, and eccentricities through theory but it can be limited by observations as there is not enough information yet available. In a similar vein, Hut et al. (1992) consider that the processes in which binary populations are formed need a better understanding. They explain the importance of determine radial velocities with the aim of calculating orbital periods and eccentricities of the binary systems, the period which can also be determined from photometry as we will see in later sections, helps to understand if the binary systems were formed by tidal capture or primordial binaries, and it also helps to determine the mass of the system. Additionally, by the time of their publication, 1992, they considered that it would take many years until a proper and complete project to characterize the binary population in globular clusters is implemented. Today, almost thirty years later, this characterization has not been done even though we do have better telescopes, instruments, and surveys. Hut et al. (1992) also suggest that an observational survey of binaries in clusters can corroborate, or reject, two predictions obtained with simulations of dynamical evolution of globular clusters, one is that most of the binary stars are more concentrated toward the central regions of the clusters, and the second is that most of the binaries were destroyed over the Hubble time in dense clusters.

1.3.5 Cataclysmic Variables

Cataclysmic variables have also been part of the research interests in astronomy, not only in the Galactic center but also in globular clusters (see e. g. Heinke et al. 2008) and are considered one of the most interesting objects found in the clusters (Belloni et al. 2016). Following the ideas from our previous section 1.3.4, as cataclysmic variables are also binary systems, they play an important role in the dynamical evolution of globular clusters specially because main-sequence binaries can be difficult to detect (Knigge 2012) and

studies done using the Kroupa models (Belloni et al. 2016) suggest that it is not possible to have cataclysmic variables formed only by considering a binary evolution system but instead it suggests that they are formed through strong dynamical interactions that can occur in systems such as globular clusters. Although they point out that this result might not be entirely congruent as there are cataclysmic variables seen in isolated fields and the models are more likely to be improved as clearly theory and observations do not match. Similarly, as the age and distance to globular clusters is known by alternatives sources, this information can be used in the test of cataclysmic variable theories (Knigge 2012). Finally, theory suggests that cataclysmic variables should be present in high quantities, around 100-200, in massive globular clusters (Knigge 2012; Belloni et al. 2016).

1.3.6 Asymptotic and red giant branch variables

In this last part of the chapter, but not less important, are the variables associated with the top of the color-magnitude diagram as is the case of the red and asymptotic giant branch. These are variables, that in comparison with the RR Lyrae stars, have not been frequently found in globular clusters, in principle because they might simply be less frequent. However, there other reasons that are also important, among them is that these type of variables are very bright and it is more likely they appear saturated in our astronomical images. Another reason is that in general, they have long periods and small amplitudes (see e. g. section 1.2.3) and if the observations do not cover a long base-time, then their variation might not be detected by the observers. Proper surveys optimized to observe these stars are needed (see, for example, discussions in Welty 1985; Frogel & Whitelock 1998). The deep understanding of red giant stars would be important as the variation is intrinsically associated with evolutionary processes of these stars in the colour-magnitude diagram as their variability stages seem to start just before the helium-flash and in the case of asymptotic giant stars seem to be associated to thermal instabilities that happen possibly before the expulsion of their external envelopes (Welty 1985). As pointed out by Frogel & Whitelock (1998), a major advantage that could be used in the study of these stars in globular clusters is that the age, distance moduli, reddening, and metallicity can be known from other studies of the clusters and be used to better understand these variables and their physical parameters as currently, they are not accurate enough. They also concluded that a greater sample of these stars in globular clusters is needed, especially in heavily-reddened metal-rich globular clusters to be able to do better studies of these stars.

Chapter 2

CCD vs EMCCD Technology

A part of the evolution in astronomy has been thanks to new technologies. The creation of modern and bigger telescopes but also implementation of new cameras employed to capture the images has enabled astronomers to reach boundaries that may be some time ago no one thought could be possible.

In the era of Charge Coupled Devices (CCDs) several benefits were obtained in comparison with the previously used photographic plates and photometers. Probably one of the most important characteristics is their linearity feature. Also, the sensitivity of CCDs goes far beyond of that reached with photographic plates in much less exposure time. The CCDs cover a larger dynamic range (see e. g. Table 1 in Furenlid 1984) and a higher quantum efficiency than photographic plates and photometers (see also Kjeldsen & Frandsen 1992). Also, the fact that images are digital and stored in computers makes CCDs a very sophisticated tool in our age of modern astronomy.

In general, to obtain a digital astronomical image the CCD is attached to the telescope as part of a camera, it is electrically power supplied, it is cooled, and properly configured through software. It captures the light of the source observed, and the readout electronics count the captured electrons to produce a digital version of the source observed which is transfered to the computer for manipulation as required by the user.

Of course, the digital image obtained will not be an exact replica of the source observed. The final image will be the result of the light that survived different environments such as interstellar dust, the atmosphere, air mass, air pollution, telescope structure, deformations in lenses and mirrors, dust, and any other impurities in the equipment used. Additionally, the final image may also suffer alterations related to the electrical devices used as in the case of the CCD which can be related to background and dark current, saturation, and transfer loss (see e. g. Howell 2006), etc.

2.1 Definition of CCDs

Charge Coupled Devices (Boyle & Smith 1970) are basically a set of electronic elements that are built and configured to capture, for a user-defined period of time, the light that is emitted or reflected by a source, and then they produce a digital picture which contains all the relevant properties related to the light that was captured . The source can be a person, an animal, a fruit, a tree, a bomb, a planet, a star, a galaxy, anything that falls within the range of detection and sensitivity of the CCDs.

In the most basic idea, the CCDs are composed of three parts: The photo-sensitive area, a readout register section, and an output node (see e. g. Smith et al. 2008).

The photo-sensitive area is a bidimensional array formed by several hundred or thousands of pixels (see Figure 2.1), it depends on the type of CCD, which are covered by a silicone emulsion that emits an electron every time that a photon is absorbed by a pixel in this section during the exposure time as long as the photon is the wavelength detection range of the silicon. The physics behind this behavior is known as the photoelectric effect.

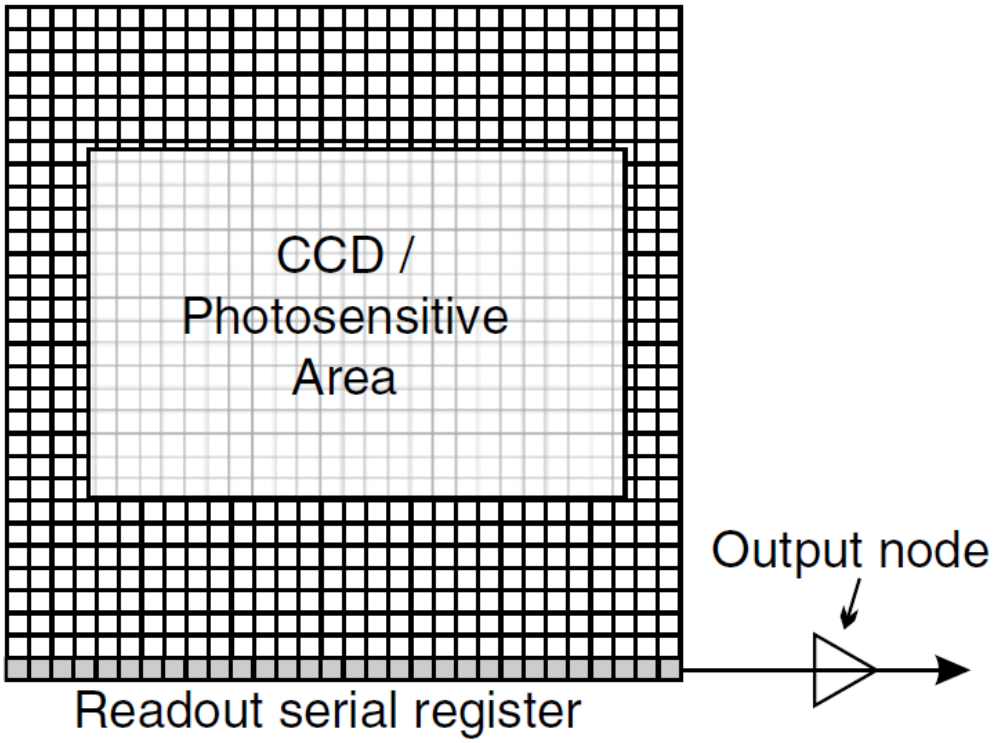

Figure 2.1: Structure of a conventional CCD. (Extracted from Figure 1 in Smith et al. 2008). The three basic parts of a CCD are shown.

To be able to hold more than a single electron in each pixel, the pixels have a specific structure. They are formed by three electrodes that are called gates and each of the gates are configured to keep all of the electrons in potential wells until the exposure is finished.

Once the exposure time is over, the total number of electrons obtained in each pixel can be shifted to their neighbor pixels because the third gate in each pixel is connected to a clock circuit. The function of the clock is to change the potential voltages in the gates cycling them to shift the electrons pixel by pixel until they are read out to the serial register and to the output node. This procedure is known as clocking (Lesser 2015; Howell 2006).

The serial register section is basically another row of pixels that are not exposed to light that works as a transition zone between the photo-sensitive area and the output node (Howell 2006).

Finally, the output node is where the electrons produced in each pixel of the photo-sensitive area are sensed and converted to voltage (Lesser 2015). This procedure is characterised by Equation 2.1

$$V = \frac{Nq}{C} \tag{2.1}$$

where C is the capacitance of the node, N is the number of electrons sensed in the node, and q is the charge of the electron. Thus, the final voltage obtained is amplified and converted to a digital number (DN) by an analog-to-digital converter, due to this, the counts in the digital images are referred as ADUs which stand for analog-to-digital-units (Howell 2006).

During the whole process explained in the previous paragraphs, several sources of noise are also introduced in the resulting image, such as readout noise, shot noise (photon noise) and fixed pattern (flat field uncertainties) noise (see e. g. Howell 2006). Regarding the readout noise, one part corresponds to the conversion from the analog signal to a digital number which conversion is not perfectly repeatable and the second corresponding to the electronics themselves as this will introduce spurious electrons to the final out-

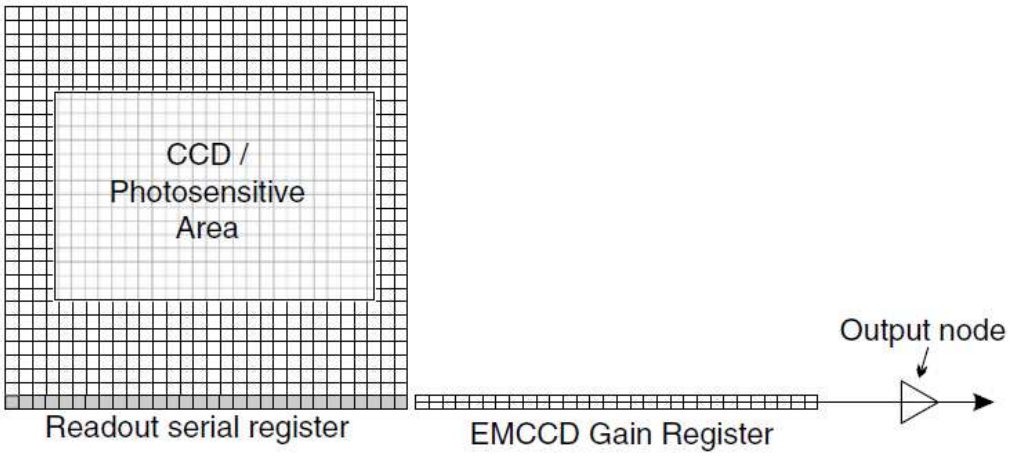

Figure 2.2: Structure of a conventional EMCCD. (Extracted from Figure 1 in Smith et al. 2008). The three basic parts of a CCD are shown.

put measured for each pixel. It also depends on the speed with which the electrons are read out, thus the faster they are read out, the higher the readout noise (Howell 2006). Photon noise is due to the fact that photons do not arrive at the photo-sensitive area at a constant rate but instead, they follow a Poison distribution. Finally, fixed patterns are associated with the fact that all pixels in the CCD might not have the same sensitivity as the others, so it is important to normalize (flat field) them to the same relative sensitivity.

2.2 Definition of EMCCDs

Astronomy, as with any other research field, is constantly making progress and it is done hand-in-hand with technology which is also constantly evolving. In CCDs, as commented in the previous section, the readout process takes some time to be done and the faster it is done, the higher the readout noise obtained. Nowadays, there are adaptive optics system and other astrophysical applications that need high frame rate imaging at very low signal levels(Lesser 2015). To address this, new techniques and cameras have been created and implemented such as the case of the Electron-Multiplying Charge Coupled Devices (EMCCDs) which are cameras that effectively reduce readout noise to less than one electron rms (Jerram et al. 2001).

EMCCDs , low light level CCDs or L3CCDs, are conventional CCDs as those described in Section 2.1. They have their photo-sensitive area, the serial register section, and the output node aswell. During the exposure time, electrons are also obtained by the photoelectric effect, etc. The only difference, as shown in Figure 2.2, is that they have an extended serial register (Lesser 2015; Howell 2006), usually known as the gain register. Each pixel in this section has been configured with high voltages, much higher than those in CCDs(Lesser 2015; Howell 2006). Thus, when electrons are shifted in each of the pixels in the gain register, there is a probability, usually of the order of 1% (Smith et al. 2008, see Section 2.3), that a new electron is created. This means, that at the end when all electrons have passed through the whole gain register, there will be an electron cascade. The result of this is that the signal is amplified in a way that makes the readout noise in comparison negligible (Tulloch & Dhillon 2011).

2.3 Comparison between CCDs and EMCCDs

As seen in Figures 2.1 and 2.2 both devices are identical in terms of the structure and electronics and both use the same physical principles. The main difference lies in the fact that EMCCDs have the gain register section which is what makes them very powerful. As defined in Smith et al. (2008), if a serial register gain

has a total number of pixels N and a probability g to create a new electron by impact ionization in each of these pixels, then the total effective gain M in an EMCCD is defined as

$$M = (1 + g)^N. \tag{2.2}$$

For a given EMCCD the typical values for g and N are 0.01 and 500-600 pixels, respectively (Smith et al. 2008) which means that effective gains of over 100 can easily be obtained. Discussions about the technical details and behavior of EMCCDs can be found at Smith et al. (2008) and Tulloch & Dhillon (2011). However, there are three modes for using the EMCCDs which the user must choose from depending on the research done and the type of performance the user would like to obtain (Smith et al. 2008; Tulloch & Dhillon 2011).

2.3.1 Mode 1 (Unity gain or Conventional mode)

In mode 1, the full QE of the EMCCD is achieved. It is referred to as conventional mode because the EMCCD camera is used as a conventional CCD. It is also referred as unity gain mode because the gain is not amplified when the photo-electrons are being moved through the extended serial register. However, since the EMCCD has been designed to be used in high gain mode, it means that when the photo-electrons are passing through this extended serial register gain, the readout noise will be higher than in CCDs. On the other hand, the dynamic range in the EMCCD is usually 16 bits for a frame in comparison to 14 bits obtained with CCDs (Smith et al. 2008). The S/N ratio obtained in this mode can be expressed as in Equation 2.3 of Tulloch & Dhillon (2011)

$$SNR_c = \frac{M}{\sqrt{M + \nu_C + D + K + \sigma_N^2}} \tag{2.3}$$

where M is the mean signal per pixel from the source, σ_N the read noise from the conventional amplifier, ν_C the mean clock induced charge generated within the EMCCD register per pixel, D the dark current and K the charge received from sky photons.

2.3.2 Mode 2 (Moderate to high gain or Linear mode)

In mode 2, the gain in the EMCCD is set to operate at a moderate or high value, (high enough to make the readout noise effects negligible). In this case, the QE is halved meaning that the S/N is reduced by a factor of $\sqrt{2}$. However, in this configuration photo-electrons can be read out at a high frame rate without losing any extra signal-to-noise ratio (Smith et al. 2008) and the extra dynamical range lost in this configuration can be recovered by shifting-and-adding frames to produce images with the desired exposure times of our astrophysical goals. As we will show later, the use of this high frame rate procedure will also give us a major advantage over the conventional mode and it is that the effect of the atmospheric turbulence will be frozen in the frames obtained, and by applying the shift-and-add technique it can be mitigated in the final science images enabling observations with high angular resolutions, resolutions similar to those obtained with space telescopes. As commented in Tulloch & Dhillon (2011), the S/N obtained can be expressed by Equation 2.4

$$SNR_{lin} = \frac{M}{\sqrt{2(M + \nu_C + D + K) + (\sigma_{EM}/g_A)^2}} \tag{2.4}$$

where σ_{EM} corresponds to the read noise in the EM amplifier and as can be seen in the equation it is negligible with the use of a high EM gain g_A. In Equation 2.4, is also possible to see the factor two in the denominator which is related to the multiplication noise (Tulloch & Dhillon 2011) and that reduces the S/N by a factor of ∼1.4 as pointed out above.

2.3.3 Mode 3 (High gain and thresholding or Photon counting mode)

In mode 3, the EMCCD achieves the full QE, but as part of the configuration, it is necessary to define a threshold level in which any counts above the threshold are considered a single photo-electron (Smith et al. 2008; Tulloch & Dhillon 2011). In this procedure, it is important to select an appropriate threshold. If it is selected too high, then pixels receiving two or more photo-electrons will be discarded. To the contrary, if the level is selected too low then the user could detect signal that is related to the clock induced change and readout noise rather than the real signal coming from a single photo-electron (Tulloch & Dhillon 2011). If the threshold is selected adequately, the multiplication noise can be completely eliminated and ideal values for S/N ratios can be obtained. Thus, this is useful for detecting weak signals where the probability of detecting more than two photo-electrons is low (Tulloch & Dhillon 2011). In this case, Tulloch & Dhillon (2011) shows that an ideal photon counting CCD S/N considering the effects of coincidence losses can be expressed by Equation 2.5

$$SNR_{pc} = \frac{M}{\sqrt{e^M - 1}}. \tag{2.5}$$

However, as pointed out in Tulloch & Dhillon (2011), this equation needs to be modified to take into account clock induced charge and the threshold level as they consider the S/N can vary greatly with those quantities. Thus, by using a photon counting threshold of 0.1 e^-_{pe}, they found the S/N given in Equation 2.6

$$SNR_{EMCCD_{pc}} = \frac{0.9M}{\sqrt{\delta}\sqrt{exp[(0.9(M + D + K)/\delta) + 0.23\ln(g_A)\nu_C] - 1}}. \tag{2.6}$$

where δ corresponds to the number of frames combined by e. g. using the shift-and-add technique as commented in Section 2.3.2.

2.4 EMCCD Reductions

As commented at the beginning of this chapter, astronomical images need to be corrected for several errors (or instrumental signatures), that are added to the images when they are taken, before they can be used for research purposes. These corrections are done using what we call calibration frames which are better known as bias, dark, and flat images.

A bias B_{ij}(ADU) is instantaneous, in this case, 0.1 seconds. These images are taken with the shutter closed to do not enable any light from reaching the photo-sensitive area of the detector. In this way, it is possible to measure the readout noise level or the background noise produced by the electronics itself. Similarly, a dark image $D_{ij}(ADU/s)$, as in the case of the bias, is taken with the shutter closed but it is taken with a given exposure time t_d with the aim of measuring what is called the dark current. It is taken with a non-zero exposure time to count the electrons produced per second by the electronics of the CCD, the amplification zone and the temperature of the CCD (see e. g. Howell 2006). In Figure 2.3 and 2.4, an example of a bias and a dark is shown. The patterns visible in the left and bottom borders are related to the multiplication effect in the extended gain register. To avoid the spurious charges, the 5% of the highest pixel values are omitted and thus, the mean value is calculated over the remaining pixels. This is known as the 5% truncated mean. Using this technique, it is found that the standard deviation in the pixel values for a master bias is ~0.25 ADU (or ~ 0.01 photons), for more details see Skottfelt et al. (2015b) and Harpsøe et al. (2012b,a).

The flat field F_{ij} is an illuminated image used to normalize the different sensitivities between pixels, to correct for imperfections in the lenses used, and to correct for any artifacts found in the field of view of the camera such as dust or any other impurities. The flats are either dome flats, in which case the telescope is pointed to a screen in the dome that is uniformly illuminated, or they are sky flats in which case the telescope is pointed to a sunset (or sunrise) illuminated section of the sky with none very few bright stars (see e. g. Howell 2006). In Figure 2.5, a sky-flat taken with the EMCCD camera used at the Danish 1.54 m telescope

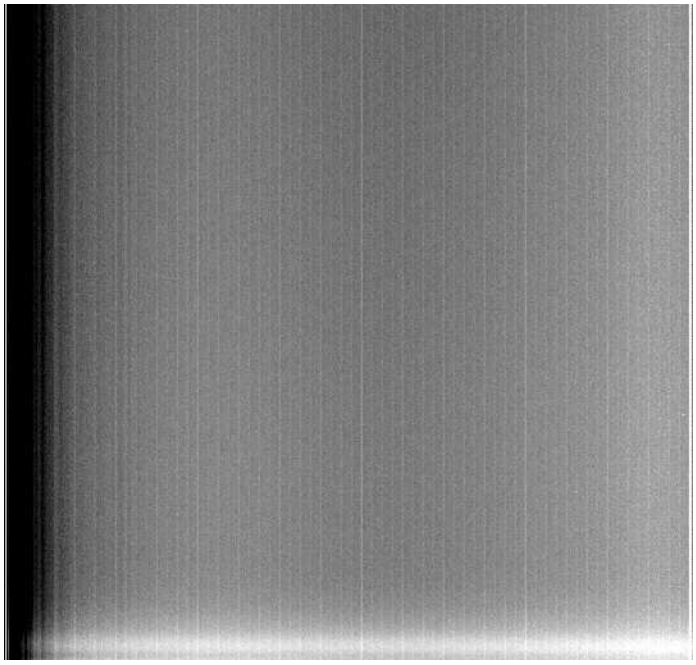

Figure 2.3: A 512×512 pixel square image that corresponds to a bias taken with the EMCCD camera used at the Danish 1.54 m telescope at ESO-La Silla observatory.

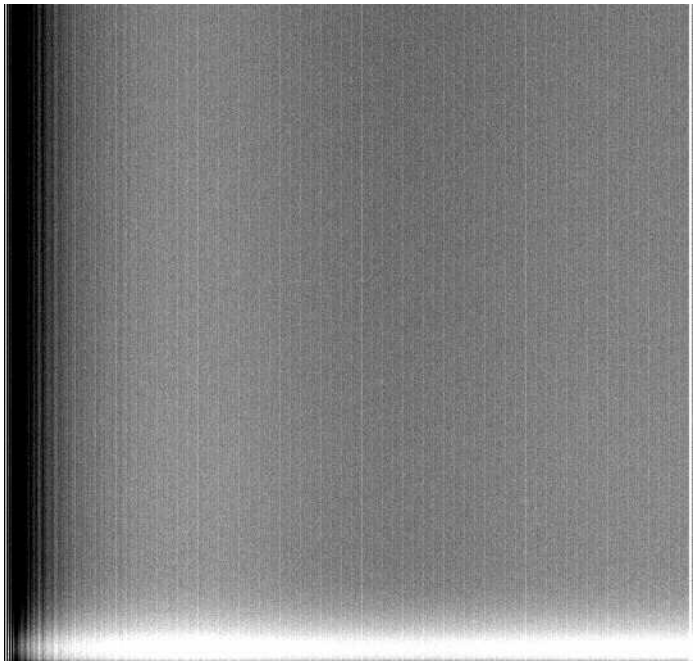

Figure 2.4: A 512×512 pixel square image that corresponds to a dark taken with the EMCCD camera used at the Danish 1.54 m telescope at ESO-La Silla observatory. It is the result of collapsing ten 0.1 second exposure time images

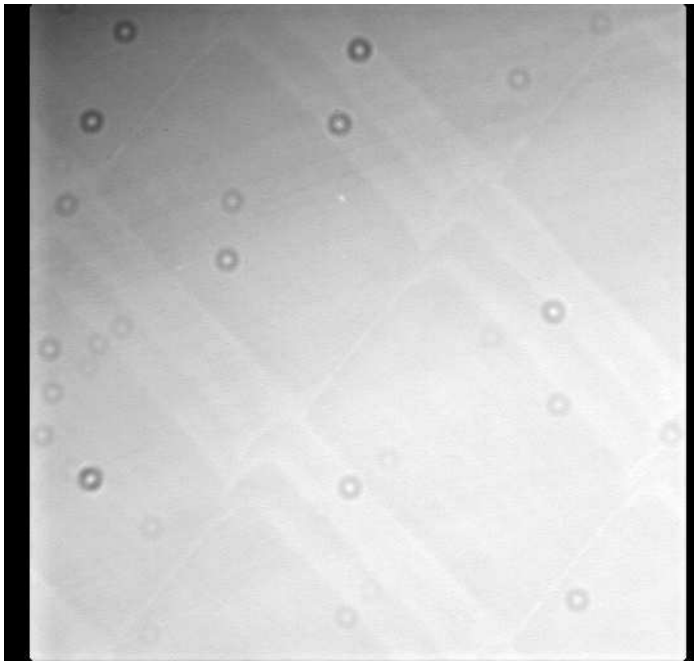

Figure 2.5: A 512×512 pixel square image that corresponds to a bias-subtracted and normalized flat taken with the EMCCD camera used at the Danish 1.54 m telescope at ESO-La Silla observatory.

at ESO-La Silla observatory. It is possible to notice several patterns along the field of view covered by the camera related to imperfections as mentioned above.

Thus, an un-calibrated science image M_{ij}(ADU) is the result of a bias section, dark, and flat contribution plus the image obtained from the light observed as shown in Equation 2.7

$$M_{ij}(\mathrm{ADU}) = B_{ij}(\mathrm{ADU}) + D_{ij}(\mathrm{ADU}/s)t_{\mathrm{image}}(s) + \phi_{ij}(e^-/s)t_{\mathrm{image}}(s)\frac{F_{ij}}{G(e^-/\mathrm{ADU})} \tag{2.7}$$

where ϕ is the incident light, F_{ij} correspond to the flat field pattern with values $\sim$1, G is the gain, and t_{image} is the exposure time of the image. The ij subscripts are the x and y pixel positions in the camera.

Rearranging Equation 2.7, the calibrated science image S_{ij}(ADU) can be expressed as

$$S_{ij}(\mathrm{ADU}) = \frac{M_{ij} - B_{ij} - D_{ij}t_{\mathrm{image}}}{F_{ij}} = \frac{\phi_{ij}t_{\mathrm{image}}}{G}. \tag{2.8}$$

2.4.1 Tip-tilt correction

Once the frames are corrected by bias, dark, and flat field as commented above, it is possible now to combine them, to produce science images with exposure times and S/N that match our research goal. In previous sections we used the term "shift-and-add" technique. The tip-tilt correction refers to the first term in this expression, "the shift". Remember that with EMCCDs we are taking very short (0.1 second exposure time) images. It means that each of the frames will be aligned with a chosen reference frame with the aim of removing the blurring produced by the atmospheric effects. The reference frame is the best quality image obtained in the observations as commented in Section 2.4.2. To do the alignment, the shift, or the tip-tilt correction, the Fourier cross correlation theorem was employed. Thus, a group of previously calibrated (bias subtracted and flat-field normalized) images $I_i(x, y)$ can be shifted respect to a reference image $R(x, y)$ by finding the global maximum of P_i defined by Equation 2.9,

$$P_i(x,y) = |FFT^{-1}[FFT(R) \cdot \overline{FFT(I_i)}]| \tag{2.9}$$

which is the cross-correlation image. FFT is the fast Fourier transform, and the overline corresponds to the complex conjugate. The position of the maximum ($x_{\max}$, $y_{\max}$) is used to shift each of the images in the sample $I_i(x,y)$ to the position of the stars in the reference image (see e. g. Harpsøe et al. 2012b; Scargle 1989).

2.4.2 Image quality and stacking

To measure the quality of the images taken with EMCCDs we cannot use the methods used when observing with conventional CCDs such as directly measuring the FWHM on the stars. Remember that because of the very short exposure times employed our frames do not really have stars but instead, they have speckles. A way to measure the quality in the images is by comparing the fluxes of the speckles at their centers with the fluxes in their surrounding areas. Thus, it is possible to quantify a quality in the speckles depending on how much flux is spread around the center or how much flux is concentrated towards the center. This can be assessed by defining the quality index q_i

$$q_i = \frac{P_i(x_{\max}, y_{\max})}{\sum_{\substack{|(x-x_{\max}, y-y_{\max})|<r \\ (x,y)\neq(x_{\max},y_{\max})}} P_i(x,y)}, \tag{2.10}$$

which represents the ratio of the maximum $P_i(x_{\max}, y_{\max})$ to the sum of the $P_i(x,y)$ values of the surrounding pixels (see e.g. Skottfelt et al. 2015a; Harpsøe et al. 2012b; Smith et al. 2009). Once this index is calculated, images from a single observation are sorted by the pipeline from the one with the best quality (smallest q_i) to the one with the worst quality (largest q_i) and a ten-layer image frame is built by stacking images in the sequence: 1%, 2%, 5%, 10%, 20%, 50%, 90%, 98%, 99% and 100%. This means that the first-layer frame has stacked the top 1% of the best quality images, the second-layer frame has stacked the next 1% of the best quality images, the third-layer frame has stacked the next 3%, the fourth has stacked the next 5% and so on. The stacking explained in this section corresponds to the second term, “the add”, in the shift-and-add technique.

2.4.3 Photometry

To extract the photometry in each of the images we used the DanDIA[1] pipeline (Bramich 2008; Bramich et al. 2013), which is based on difference image analysis (DIA).

As commented in Sec. 2.4.2, for each EMCCD observation, we produced a ten-layer calibrated image cube where each of the images in the cube is sorted by quality. DanDIA builds a high S/N and high-resolution reference frame by selecting and combining the best quality images from all available cubes. In this study, we use the layers with the best FWHM over all the frames to build the reference image for each globular cluster (usually the 1%, 2%, and 5% layer-frames) and we stack the ten-layers of an observation into a single science image for the photometry. This is done by detecting bright stars using DAOFIND (Stetson 1987) and employing these to align the images using the triangulation technique described in Pál & Bakos (2006). In Figure 2.6 the reference frame used in the analysis of globular cluster NGC 6715 is shown. Similar finding charts for each of the clusters were done and the mean PSF FWHM for each reference image is listed in Tab. 3.2. Positions and reference fluxes ($f_{\rm ref}$) in ADU/s for each star are calculated using the PSF photometry package "STARFINDER" (Diolaiti et al. 2000a). The pipeline implements a low-order polynomial degree for the spatial variation of the PSF model (a quadratic polynomial degree was sufficient in our case).

Once the reference image is built, all of the science frames are registered with the reference image by using again the Stetson (1987) and Pál & Bakos (2006) algorithms described before. Image subtraction

[1] DanDIA is built from the DanIDL library of IDL routines available at `http://www.danidl.co.uk`

then determines a spatially variable kernel, modeled as a discrete pixel array, that best matches the reference image to each science image. The photometric scale factor ($p(t)$) used to scale the reference frame to each image is calculated as part of the kernel model (Bramich et al. 2015). Difference images are created by subtracting the convolved reference image obtained as part of determining the spatially variable kernel from each science image. Finally, difference fluxes ($f_{\rm diff}(t)$) in ADU/s for each star detected in the reference image are measured in each of the difference images by optimally scaling the point spread function model for the star to the difference image.

The next step, is to obtain the light curves, as we are working with difference image analysis we need to calculate the total flux ($f_{\rm tot}(t)$) in ADU/s for the stars. To do so, the difference fluxes of the stars $f_{\rm diff}(t)$ are scaled to the same level of the fluxes in the reference image $f_{\rm ref}$ by using using the photometric scale factor $p(t)$ as shown in Equation 2.11

$$f_{\rm tot}(t) = f_{\rm ref} + \frac{f_{\rm diff}(t)}{p(t)}. \tag{2.11}$$

Now the instrumental magnitudes $m_{\rm ins}$ at each given time t can be obtained using the total flux through the typical magnitude equation (see e. g. Howell 2006) shown in Equation 2.12:

$$m_{\rm ins}(t) = 17.5 - 2.5\log(f_{\rm tot}(t)). \tag{2.12}$$

A detailed description of the procedures and techniques employed by the pipeline can be found in Bramich et al. (2011).

The total error in our analysis is given in terms of a readout noise contribution (see e. g. Smith et al. 2008) given by σ_0 and a contribution given by the photon noise σ_{photon} as in Equation 2.13

$$\sigma_{total} = \sqrt{\sigma_0^2 + \sigma_{photon}^2} \tag{2.13}$$

which can be expressed as the total variance

$$\sigma_{total}^2 = \sigma_0^2 + \sigma_{photon}^2 = \sigma_0^2 + \lambda. \tag{2.14}$$

Remember that the photon noise follows a Poison distribution where λ is the average frequency of incoming photons reaching the photo-sensitive area of the CCD, thus $\sigma_{photon} = \sqrt{\lambda}$.

In a similar vein, the total error for a none calibrated science image is given as

$$\sigma_{M_{ij}}^2(e^{-2}) = \sigma_0^2(e^{-2}) + S'_{ij}(e^-/s)\phi_{ij}t_{\rm image}F_{ij} \tag{2.15}$$

but this expression is given in electrons. We can expressed in ADUs by normalizing it with the gain $G(e/\mathrm{ADU})$. In this case we will have that

$$\sigma_{M_{ij}}^2(\mathrm{ADU}^2) = \frac{\sigma_{M_{ij}}^2(\mathrm{e}^{-2})}{G^2(e^{-2}/\mathrm{ADU}^2)} \tag{2.16}$$

$$\sigma_0^2(\mathrm{ADU}^2) = \frac{\sigma_0^2(e^{-2})}{G^2(e^{-2}/\mathrm{ADU}^2)} \tag{2.17}$$

$$S_{ij}(\mathrm{ADU}) = \frac{S'_{ij}(e^-)\phi_{ij}t_{image}}{G(e^-/\mathrm{ADU})}. \tag{2.18}$$

Now, our Equation 2.15 using the new terms given in Equations 2.16, 2.17, and 2.18 is given as follows

$$G^2\sigma_{M_{ij}}^2(\mathrm{ADU}) = \sigma_0^2(\mathrm{ADU}^2)G^2 + \left[\frac{S_{ij}(\mathrm{ADU})G}{t_{image}}\right]t_{image}F_{ij} \tag{2.19}$$

which is equivalent to

$$\sigma^2_{M_{ij}} = \sigma^2_0 + \frac{S_{ij}}{G} F_{ij}. \tag{2.20}$$

Thus, if we consider a science image already calibrated (bias-corrected and flat normalized), we can express its error as

$$\sigma^2_{S_{ij}} = \sigma^2_{M_{ij}} \frac{1}{F^2_{ij}} \Rightarrow \sigma^2_{M_{ij}} = \sigma^2_{S_{ij}} F^2_{ij}. \tag{2.21}$$

Now, we can include this term in Equation 2.20 which gives us

$$\sigma^2_{S_{ij}} F^2_{ij} = \sigma^2_0 + S_{ij} \frac{F_{ij}}{G}. \tag{2.22}$$

The last expression drives us to the variance calculated pixel by pixel in a calibrated science image as shown in Equation 2.23

$$\sigma^2_{S_{ij}} = \frac{\sigma^2_0}{F^2_{ij}} + \frac{S_{ij}}{G F_{ij}} \tag{2.23}$$

In a similar vein, it is possible to demonstrate that for an EMCCD, the noise model for a single exposure is given as:

$$\sigma^2_{ij} = \frac{\sigma^2_0}{F^2_{ij}} + \frac{2\, S_{ij}}{F_{ij}\, G_{\rm EM}\, G_{\rm PA}}, \tag{2.24}$$

where $G_{\rm EM}$ is the electron-multiplying gain (photons/e^-) and $G_{\rm PA}$ is the pre-amplication gain (e^-/ADU).

Thus, if N exposures are combined by summation as explained with the shift-and-add technique, then the noise model for the combined image $\sigma^2_{ij,\rm comb}$ is given by Eqn. 2.25:

$$\sigma^2_{ij,\rm comb} = \frac{N\, \sigma^2_0}{F^2_{ij}} + \frac{2\, S_{ij,\rm comb}}{F_{ij}\, G_{\rm EM}\, G_{\rm PA}}, \tag{2.25}$$

where $S_{ij,\rm comb}$ is the science image of the combined (stacked) frames (see e. g. Skottfelt et al. 2015a). It is also possible to see the factor 2 related to the multiplication noise explained in Tulloch & Dhillon (2011) and showed in Equation 2.4 in our Section 2.3.2.

In Tab. 2.1, we illustrate the format of the electronic table with all fluxes and photometric measurements as they are available at the CDS[2].

[2]http://cds.u-strasbg.fr/

Table 2.1: Time-series I-band photometry for all known and new variables in the field of view covered in each globular cluster. The standard $M_{\rm std}$ and instrumental $M_{\rm ins}$ magnitudes are listed in columns 5 and 6, respectively, corresponding to the cluster, variable star, filter, and epoch of mid-exposure listed in columns 1-4, respectively. The uncertainty on $M_{\rm ins}$ is listed in column 7, which also corresponds to the uncertainty on $M_{\rm std}$. For completeness, we also list the quantities $f_{\rm ref}$, $f_{\rm diff}$ and p from Eq. 2.11 in columns 8, 10 and 12, along with the uncertainties $\sigma_{\rm ref}$ and $\sigma_{\rm diff}$ in columns 9 and 11. This is an extract from the full table, which is available with the electronic version of the articles Figuera Jaimes et al. (2016b) and Figuera Jaimes et al. (2016a) at the CDS.

Cluster	var id	Filter	HJD (d)	$M_{\rm std}$ (mag)	$M_{\rm ins}$ (mag)	σ_m (mag)	$f_{\rm ref}$ (ADU s^{-1})	$\sigma_{\rm ref}$ (ADU s^{-1})	$f_{\rm diff}$ (ADU s^{-1})	$\sigma_{\rm diff}$ (ADU s^{-1})	p
NGC104	PC1-V12	I	2456472.93210	15.846	6.777	0.014	24971.015	9644.446	-30350.989	1425.567	5.5131
NGC104	PC1-V12	I	2456476.94184	15.729	6.659	0.012	24971.015	9644.446	-16234.626	1138.337	4.9447
⋮	⋮	⋮	⋮	⋮	⋮	⋮	⋮	⋮	⋮	⋮	⋮
NGC5139	V457	I	2456432.58154	15.735	6.649	0.007	20096.379	0684.928	+08409.333	0673.724	4.6618
NGC5139	V457	I	2456438.70588	15.832	6.746	0.005	20096.379	0684.928	-00312.498	0432.554	4.5021
⋮	⋮	⋮	⋮	⋮	⋮	⋮	⋮	⋮	⋮	⋮	⋮
NGC5286	V37	I	2456445.53773	15.978	6.951	0.005	18451.916	1202.455	-08631.145	0385.937	4.6006
NGC5286	V37	I	2456446.53053	15.744	6.717	0.003	18451.916	1202.455	+09806.700	0232.129	4.6341
⋮	⋮	⋮	⋮	⋮	⋮	⋮	⋮	⋮	⋮	⋮	⋮

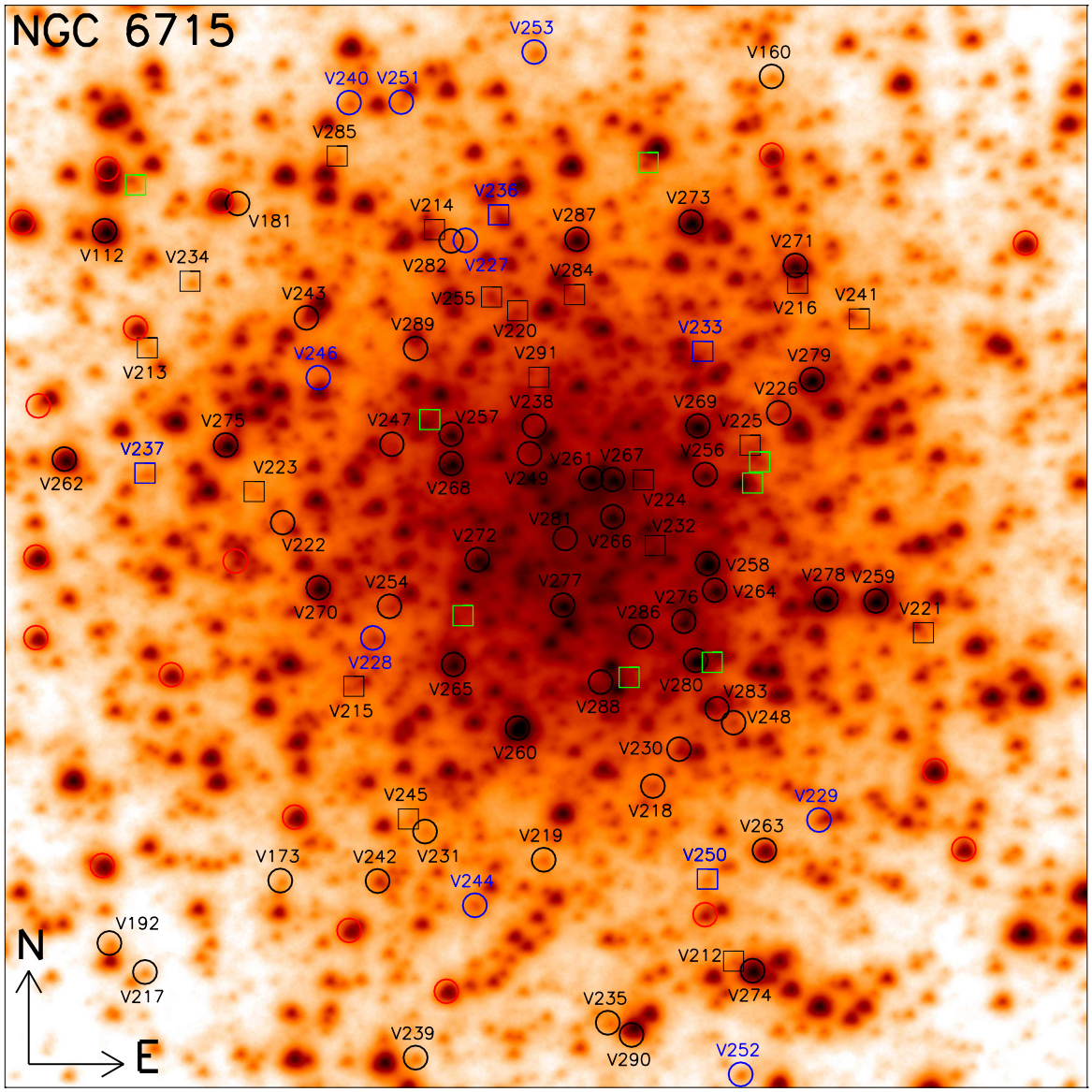

Figure 2.6: Finding chart for the globular cluster NGC 6715. The image used corresponds to the reference image constructed during the reduction. All known variables and new discoveries are labeled with their V numbers. Known variables, or new variables discovered in this work, are plotted with black symbols. Variables discovered by the OGLE survey are plotted with blue symbols. Those variables that were candidate variables from Montiel & Mighell (2010) are plotted using squares. Otherwise, symbols are circles. Green squares and red circles, both without labels, are candidate variables from Montiel & Mighell (2010) and McDonald et al. (2014) respectively for which we do not detect variability in our survey. Image size is $\sim 40 \times 40 \mathrm{arcsec}^2$.

Chapter 3

New Variables in Globular Clusters

To exploit the benefits of using Electron-Multiplying CCDs and the shift-and-add technique using globular clusters it was necessary to select a group of globular cluster candidates to be observed. The criteria used in the selection are explained in the next sections.

3.1 Selection of Clusters

In the Milky Way galaxy there are 157 globular clusters so far known. As commented before, their main physical properties and characteristics are listed in (Harris 1996, 2010 version) and their variable star population known in Clement et al. (2001). Due to limitation in observational time and telescopes facilities the next steps to chose a sample of clusters was employed:

- Geographical position of the telescope. A visibility graphic with all globular clusters considering the geographical position of the telescope was done as not all globular clusters can be observed from the same altitude and longitude. We also considered into account pointing restrictions of the telescope.
- Globular cluster density. As part of testing the camera and the technique employed we selected globular clusters with different concentration of stars, to do so we used as reference the central luminosity density ρ_0 ($L_\odot \mathrm{pc}^{-3}$) listed in Harris (1996). We selected clusters with a high density such as NGC 6752 ($\log(\rho_0)$=5.04), clusters with intermediate density as NGC 5139 ($\log(\rho_0)$=3.15), and clusters not so dense as NGC 6723 ($\log(\rho_0)$=2.79).
- Bibliography review. We did an extense review about previous studies done on these globular clusters particularly in their variable stars known. To do this review we used the SAO/NASA Astrophysics Data System[1] (ADS) and the Catalogue of Variable Stars in Galactic Globular Clusters Clement et al. (2001) and made sure to include in our sample globular clusters with variable stars known to test the reliability of our techniques and tools used.
- Review of known colour-magnitude diagrams (CMD). As all the stars in the globular clusters depending of their evolutive stages are occuping a well defined position in the CMD, we also selected clusters with a high concentration of stars in the regions where variable stars are expected to be. This is, the top of the red giant branch, instability strip of the horizontal branch, and blue straggler region, with the aim of finding semi-regular, RR Lyrae, and SX Phoenicis variable stars, between others. The magnitude and colour information used to built the diagrams were taken from the ACS survey of Galactic globular clusters[2] and also used the Galactic globular cluster database[3].

[1] http://adswww.harvard.edu/
[2] http://www.astro.ufl.edu/~ata/public_hstgc/
[3] http://gclusters.altervista.org/

- Exposure times. As globular clusters have different types of luminosities, we decided to use the known V magnitude of the horizontal branch as a reference to chose the right exposure time to be used with the EMCCD and grouped the clusters in 3 different levels as follow:

$$6 \text{ min for } V_{\rm HB} < 14 \text{ mag},$$
$$8 \text{ min for } 14 \text{ mag} < V_{\rm HB} < 17 \text{ mag},$$
$$10 \text{ min for } V_{HB} > 17 \text{ mag}.$$

  The reader might have noticed that our selection of exposure times for the fainter horizontal branch magnitudes does not follow the same proportion as the exposure times selected for the brighter horizontal branches in order to have the same signal-to-noise ratio for all the clusters at different distances. The observing time at the Danish telescope was originally assigned to cover extra-solar planets candidates through the MiNDSTEp consortium using the microlensing technique, this is the main programme to which most of the observing time is assigned. Thus, our observations were limited to windows of time when no microlensing events were available.

Finally, we chose the 11 clusters studied in the present work. Their positions in the Galactic plane are given in Figure 3.1 and in Table 3.2 we sumarize someof the physical properties available in the Harris (1996) catalog. Along this thesis we use as reference the globular cluster NGC 6715 to illustrates and to explains all the techiques and procedures implemented in the detection and extraction of the variables stars, however plots and tables for the remaining clusters studied are given in Chapter 4. If any particular figure of a given cluster needs an explaination in the text the proper citation will be done to the figure will be done. Also, in Table 3.1 we supply the colour and symbols adopted to mark the variables stars in figures and diagrams.

Table 3.1: Convention used in the variable star classification of this work based on the definitions of the General Catalogue of Variable Stars (Samus et al. 2009a). Column 1 corresponds to the type of variability, Column 2 is the abbreviated name for the specific variability type, Column 3 is the shape of the point used to plot the variable, and Column 4 is the colour used to plot the point.

Type	Id	Point style	Colour
Pulsating Variables			
SX Phoenicis	SX Phe	Filled triangle	Cyan
RR Lyrae (RRL)	RR0	Filled circle	Red
	RR1	Filled circle	Green
	RR01	Filled circle	Blue
W Virginis	CWA	Inverted triangle	Green
Semi-regular	SR	Filled square	Red
Long-period irregular	L	Filled square	Blue
Cataclysmic Variables			
In general	DN, Novae	Filled five pointed star	Green
Eclipsing Binaries			
In general	E	Filled five pointed star	Blue
Unclassified Variables			
In general	NC	Filled square	Yellow

3.2 Time-Resolved Imaging Observations

The globular cluster observational programme was done as part of the studies carried out by the Microlensing Network for the Detection of Small Terrestrial Exoplanets (MiNDSTEp) consortium. Observations were

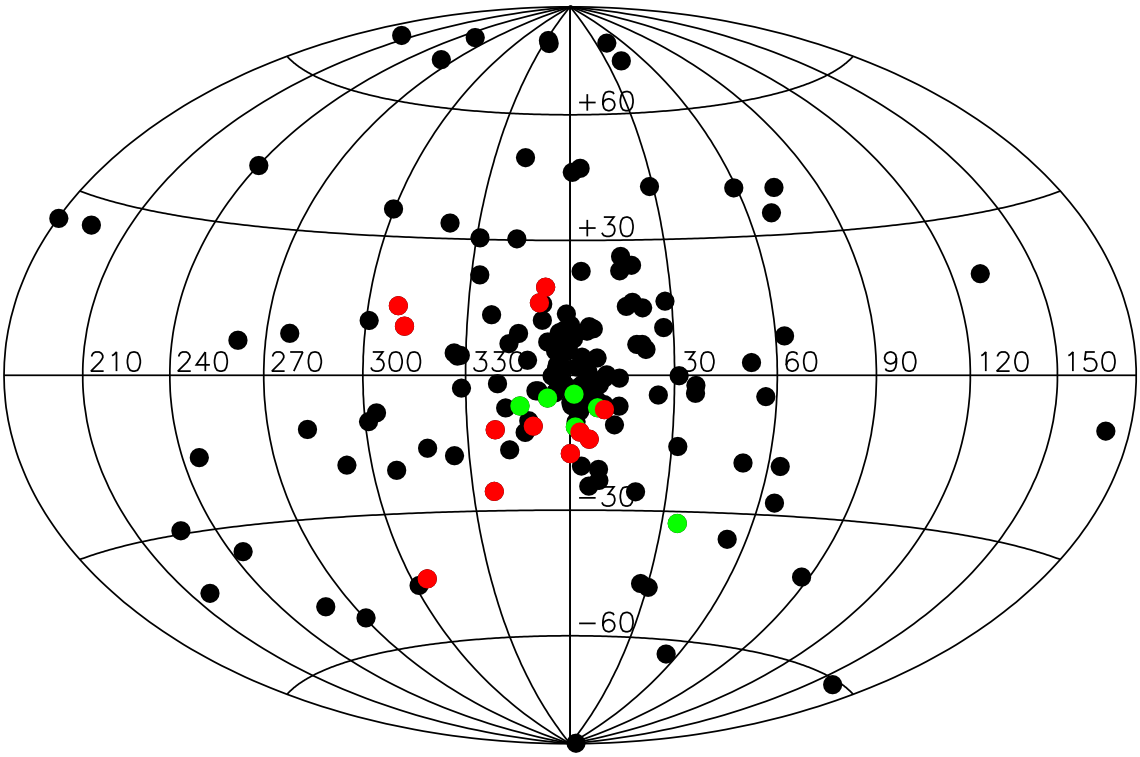

Figure 3.1: Plot in galactic coordinates showing the 157 globular clusters (black points) so far known in our Galaxy. The clusters in colour correspond to those studied in this work.

Table 3.2: Some of the physical properties of the globular clusters studied in this work. Column 1, is the name of the cluster as it is defined in the New General Catalogue, Columns 2 and 3 are the celestial coordinates (right ascension and declination), Column 4 is the distance from the Sun, Column 5 is distance from the Galactic centre, Column 6 is metallicity, Column 7 is reddening, Column 8 is V magnitude level of the horizontal branch, Column 9 is V distance modulus, Column 10 is King-model central concentration c = $\log(r_t/r_c)$, Column 11 is central luminosity density $\log_{10}(L_\odot \mathrm{pc}^{-3})$, Column 12 is the mean full-width half-maximum (arcsec) measured in the reference image and Column 13 is the exposure time in the reference image.

Cluster	RA	Dec	$D_\odot$	D_{gc}	[Fe/H]	E(B-V)	V_{HB}	$V - M_V$	c	ρ_0	FWHM	t_{exp}
NGC	J2000	J2000	kpc	kpc		mag	mag	mag			arcsec	s
104	00:24:05.67	-72:04:52.6	4.5	7.4	-0.72	0.04	14.06	13.37	2.07	4.88	0.61	302.4
5139	13:26:47.24	-47:28:46.5	5.2	6.4	-1.53	0.12	14.51	13.94	1.31	3.15	0.38	312.0
5286	13:46:26.81	-51:22:27.3	11.7	8.9	-1.69	0.24	16.63	16.08	1.41	4.10	0.37	316.8
6093	16:17:02.41	-22:58:33.9	10.0	3.8	-1.75	0.18	16.10	15.56	1.68	4.79	0.45	302.4
6121	16:23:35.22	-26:31:32.7	2.2	5.9	-1.16	0.35	13.45	12.82	1.65	3.64	0.49	180.0
6541	18:08:02.36	-43:42:53.6	7.5	2.1	-1.81	0.14	15.35	14.82	1.86	4.65	0.56	340.8
6656	18:36:23.94	-23:54:17.1	3.2	4.9	-1.70	0.34	14.15	13.60	1.38	3.63	0.50	297.6
6681	18:43:12.76	-32:17:31.6	9.0	2.2	-1.62	0.07	15.55	14.99	2.50	5.82	0.49	312.0
6715	18:55:03.33	-30:28:47.5	26.5	18.9	-1.49	0.15	18.16	17.58	2.04	4.69	0.44	348.0
6723	18:59:33.15	-36:37:56.1	8.7	2.6	-1.10	0.05	15.48	14.84	1.11	2.79	0.51	360.0
6752	19:10:52.11	-59:59:04.4	4.0	5.2	-1.54	0.04	13.70	13.13	2.50	5.04	0.59	198.0

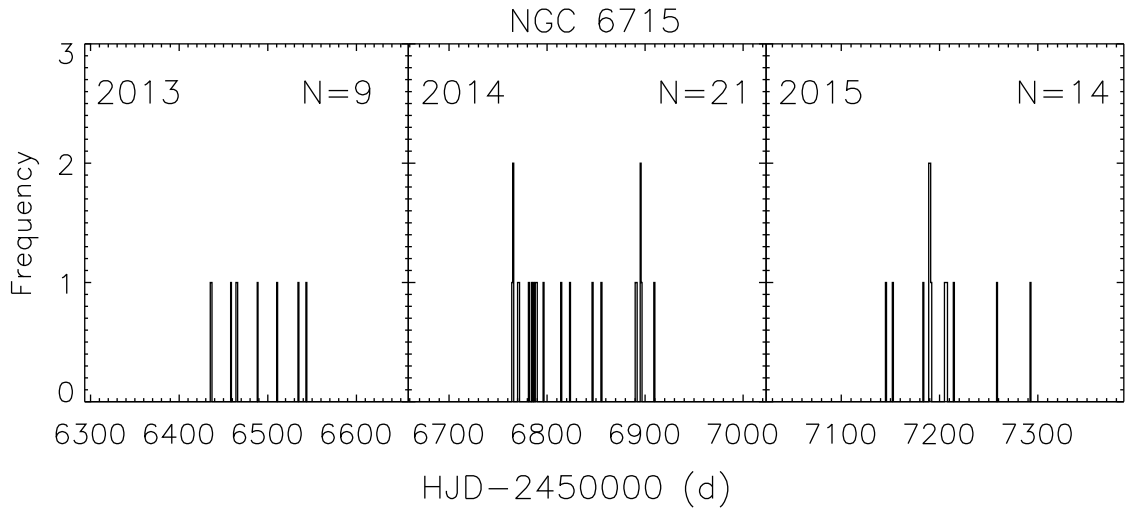

Figure 3.2: Each box represents the histograms with the number of data taken during each year for the globular cluster NGC 6715. Thus, on the left is the 2013, in the middle 2014, and on the right 2015.

taken during April to September in the years 2013-2015 for a sample of 11 globular clusters. In Figure 3.2 the histogram with the number of observations taken per year for the globular cluster NGC 6715 is shown. Histograms for all globular clusters observed in this work are shown in Figure A.1.

The data was taken using the 1.54 m Danish telescope at the ESO observatory at La Silla in Chile.

The telescope is located at an elevation of 2340 m at 70°44′07.662W 29°15′14.″235S and is equipped with an Andor Technology iXon+897 EMCCD camera that is formed by an array of 512 × 512 where each pixel has a size of 16 μm and a scale of 0″.09 covering a total field of view of ~45×45 arcsec^2. In this research, the camera was configured to work at a frame rate of 10 Hz and an EM gain of 300e$^-$/photon. It is located behind a dichroic mirror that works as a long-pass filter. This is, the mirror and camera cover a wavelength range of between 650 nm to 1050 nm, which is roughly a combination of SDSS i′+z′ filter (Bessell 2005).

3.3 Photometric calibration

The photometric transformation of instrumental magnitudes to the standard system was accomplished using information available in the ACS Globular Cluster Survey, which provides calibrated magnitudes for selected stars in the fields of 50 globular clusters extracted from images taken with the *Hubble* Space Telescope (HST) instruments ACS and WFPC.

By matching the positions of the stars in the field of the HST images with those in our reference image, we obtained the photometric transformation shown in Figure 3.3. The I magnitude obtained from the ACS (see Sirianni et al. 2005) is plotted versus the instrumental i′+z′ magnitude obtained in this study. The red line is a linear fit with slope unity yielding the zero point labelled in the title where *N* is the number of stars used in the fit and *R* is the correlation coefficient obtained. Due to the substantial differences between the i′+z′ and standard I wavebands, there are non-linear colour terms in the transformation that we have not accounted for. However, we have opted for an approximate absolute photometric calibration since variable star discovery and classification do not require a precise calibration. Furthermore, our non-standard i′ + z′ waveband precludes the possibility of using our RR Lyrae light curves for physical parameter estimation. Similar photometric calibration were obtained for all the clusters listed in Table 3.2 and are shown in Figure B.1.

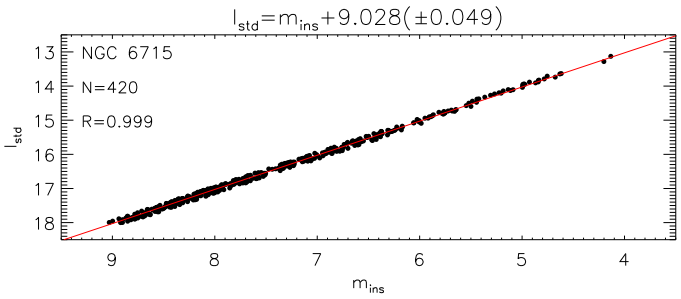

Figure 3.3: Standard I magnitude taken from the HST observations as a function of the instrumental i′ + z′ magnitude. The red line is the fit that best matches the data and it is described by the equation in the title. The correlation coefficient is 0.999.

3.4 Astrometry and finding chart

To create a reference image with the astrometric information for each star in the field covered in NGC 6715, we used the celestial coordinates available in the ACS Globular Cluster Survey[4] (see Anderson et al. 2008) which were uploaded for the field of the cluster through GAIA (Graphical Astronomy and Image Analysis Tool; Draper 2000). An (x,y) shift to match their respective stars in our reference image was applied. Stars lying outside the field of view and those without a clear match were removed, and the (x, y) shift was refined by minimising the squared coordinate residuals. A total of 305 stars over the entire field was used to guarantee that the astrometric solution applied to the reference image considered enough stars. The radial Root Mean Square (RMS) scatter obtained in the residuals was ∼0″.028 (∼ 0.3 pixels). This astrometrically calibrated reference image was used to produce a finding chart for NGC 6715 on which we marked the positions and identifications of all variable stars studied in this work (Fig. 2.6). Finally, a table with the equatorial J2000 celestial coordinates of all variables is given in Table 4.1. Similar astrometric solutions were applied to the reference frames of each of the globular cluster studied in this work. Their finding charts are shown along this thesis.

3.5 Known and new variables

To do the detection and extraction of known variables and new discoveries, due to the high amount of data needed to be analysed, it was necessary to employ several automatic (or semi-automatic) techniques. The DanDIA pipeline detected ∼14000 stars in the core of the eleven globular clusters which were manipulated through three different techniques, the root mean square (rms), the S B statistic, and the stacked difference images.

3.5.1 Root mean square

By constructing the root mean square (rms) magnitude deviation against mean I magnitude for each of the globular clusters it was possible to quantify the photometric scatter in each of the stars in those stellar systems and also the intrinsic variation of the variable stars over time. In Figure 3.4 (top) is possible to see the rms for NGC 6715. In this globular cluster we covered the range in magnitudes between ∼12 to 18.5 mag. and the scatter obtained is less than 0.01 for the brighter stars that are not variables. The points in colour correspond to the variable stars in this globular cluster following the convention adopted in Table 3.1.

It is interesting to see that the brightest stars show an exponential increase (which appears as linear on log-scale) even for none variable stars. This feature can be explained by considering that the brightest stars

[4]http://www.astro.ufl.edu/~ata/public_hstgc/

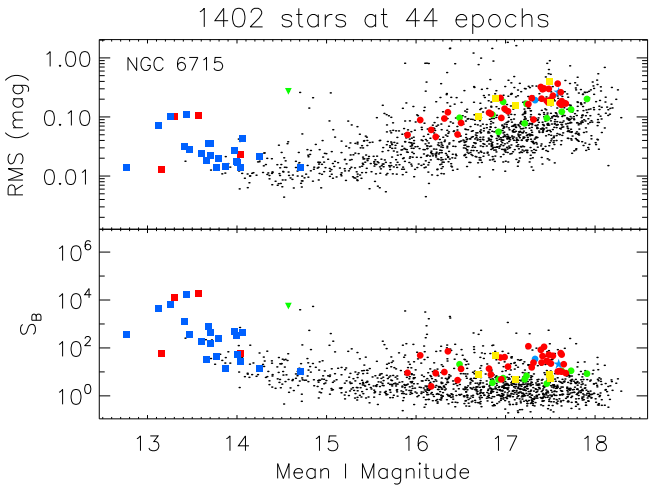

Figure 3.4: Root mean square (RMS) magnitude deviation (top) and S_B statistic (bottom) versus the mean I magnitude for the 1402 stars detected in the field of view of the reference image for NGC 6715. Coloured points follow the convention adopted in Table 3.1 to identify the types of variables found in the field of this globular cluster.

are dominated by systematic errors that exist at some level in all light curves while the fainter stars are dominated by pure Gaussian noise. A similar behavior can be seem in the S_b diagram shown below.

It is also possible to notice that variable stars are located mainly toward the edges of the diagrams leaving the middle region free of variables. This is because the x-axis corresponds to the magnitude of the stars, thus indirectly their positions resemble those in the color-magnitude diagram, in which brighter variable stars are at the top of the red giant branch and fainter stars towards the blue straggler region. The lack of variables, unless they are extrinsic variables such as eclipsing binaries, in the middle of the RMS is related to the position of the stars in the upped end of the main sequence where they are still in a stable stage of their life-time.

3.5.2 S_B statistic

In our effort to detect and extract the variable stars in the observed fields, we aimed to implement a technique that was not magnitude dependent and weighted our data using the uncertainties and residuals. During the literature review done to accomplish this purpose we found the Tamuz et al. (2006) paper which uses an algorithm to analyse a large number of light curves for automatic detection of binary stars through an alarm statistic $\mathscr{A}$ (see their Equation 3). Thus we adapted this equation to better weigh our light curves for variable star detection which we defined as S_b index in (Figuera Jaimes et al. 2013). To apply this index, first we need to calculate the mean or median magnitude (light curve model if the star was not variable) for the star under study. There will be data points that will fall below or above the model. If the star is not variable, the data points will be closer to the model while if the star is variable then there will be data points further from the model. This information is very useful to weigh the variability of a star (or lack thereof) through the residuals obtained by subtracting the magnitudes observed to the model, in addition, we also take into account the number of data points that fall above or below our model to also weigh the variability of the star. Our procedure is defined in Equation 3.1

$$S_b = \left(\frac{1}{NM}\right)\sum_{i=1}^{M}\left(\frac{r_{i,1}}{\sigma_{i,1}} + \frac{r_{i,2}}{\sigma_{i,2}} + \ldots + \frac{r_{i,k_i}}{\sigma_{i,k_i}}\right)^2, \tag{3.1}$$

where N is the number of data points for a given light curve and M is the number of groups formed of time-consecutive residuals of the same sign from a constant-brightness light curve model (e. g. mean or median).

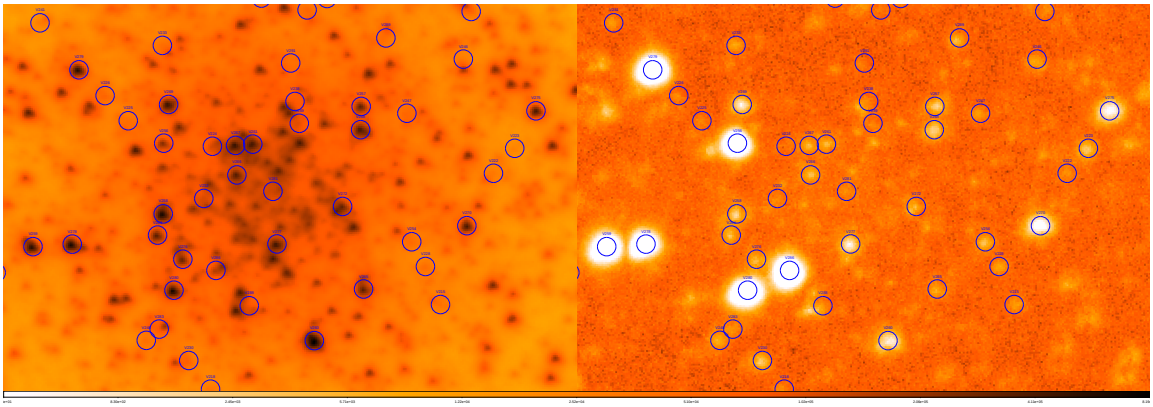

Figure 3.5: Zoom in to the central region of the globular cluster NGC 6715. On the left all the stars in the field covered are shown and variables stars are labeled in blue. On the right the stacked image is shown. Similarly, the position of the variable stars is given in blue. The spots at their positions correspond to the sum of the differential fluxes as given in Equation 3.2.

The residuals $r_{i,1}$ to r_{i,k_i} correspond to the ith group of k_i time-consecutive residuals of the same sign with corresponding uncertainties $\sigma_{i,1}$ to σ_{i,k_i}. The S_b statistic is larger in value for light curves with long runs of consecutive data points above or below the mean, which is the case for variable stars with periods longer than the typical photometric cadence.

In Figure 3.4 (bottom) the S_b diagram obtained for NGC 6715 is shown. In colour all the variable stars studied in this cluster are marked following the convention adopted in Table 3.1. To select candidates to variable stars in this cluster we chose a threshold of 3 times above the model S_b which is the median (50%) curve determined from our simulations. Any star over the threshold were selected as candidates to be variables. S_b diagrams for the remaining 10 globular cluster studied in this work are also shown along the thesis.

3.5.3 Stacked difference image

Based on the results obtained using the DanDIA pipeline, a stacked difference image was built for NGC 6715 with the aim of detecting the difference fluxes that correspond to variable stars in the field of the reference image. The stacked image is the result of summing the absolute values of the difference images divided by the respective pixel uncertainty

$$S_{ij} = \sum_k \frac{|D_{kij}|}{\sigma_{kij}}, \tag{3.2}$$

where S_{ij} is the stacked image, D_{kij} is the kth difference image, σ_{kij} is the pixel uncertainty associated with each image k and the indexes i and j correspond to pixel positions.

In Figure 3.5, a zoom in to the centre of the reference image (left) used during the reductions and the stacked of the difference images (right) obtained for NGC 6715 are shown. Both images cover the same field of the globular cluster and in blue circles the variable stars are marked. In the stacked image the sum of the difference fluxes given in Equation 3.2 at the position of variable stars are shown. In this way is also possible to detect variable stars in the fields observed.

3.6 Classification

After the detection of known variables and new discoveries in all the globular clusters studied in this work, their light curves were analysed to classified them based on the physical nature of their variations. To do so,

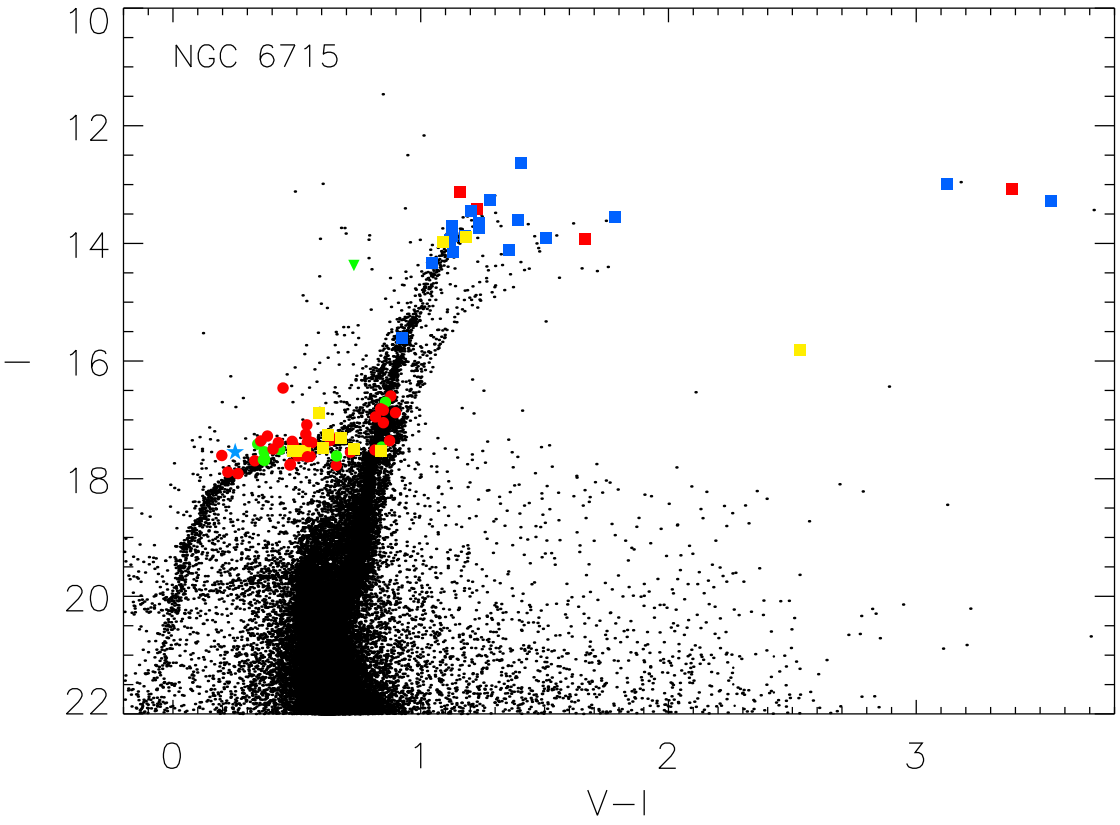

Figure 3.6: Colour magnitude diagram for the globular cluster NGC 6715 built with V and I magnitudes available in the ACS globular cluster survey extracted from HST images. The variable stars are plotted in colour following the convention adopted in Table 3.1.

several procedures were implemented as explained in the next sections.

3.6.1 Colour-magnitude diagram

During the campaing in which our observations were taken, it was only possible to use the EMCCD camera as a long-pass filter (See Section 3.2). Due to this we employed the magnitudes and colour available from the HST images at the "ACS Globular Cluster Survey"[5]. The magnitudes used correspond to the V and I Johnson obtained in Sirianni et al. (2005).

In Figure 3.6, the colour-magnitude diagram (CMD) for NGC 6715 is shown. The colour points correspond to the variable stars detected in this work. Their positions in the diagram was done by matching the celestial coordinates (See Section 3.4) of the variables obtained with our reference image and the coordinates given in Sirianni et al. (2005). As is seen in the figure variable stars are occuping well defined zones in the diagram. It gave of the first clue about their classification. Thus variable stars in the horizontal branch are more likely to be RR Lyrae stars and variable stars in the red giant branch are more likely to be long-period or semi-regular variables, variables in the blue straggler zone are more likely to be SX Phoenicis. Finally, their positions in the CMD in combination with the periods found for each of the variables were used to decide the type of variable the stars are. It was also useful to decide the cluster membership of these stars.

[5]http://www.astro.ufl.edu/ãta/public_hstgc/

3.6.2 Period search

Depending on the physical nature of the variable stars they can have periodic, semi-periodic, and aperiodic variations. To do a period search in all the variable stars studied in this work we mainly employed the traditional Lafler & Kinman method (Lafler & Kinman 1965). The method measures the length of the curve produced by the light curve for a range of trial periods. To do so, the phase of the star is calculated in each of the trial periods. Once the light curve is phased the programme measures the difference between two successive magnitudes and adds it to the difference obtained from the next two magnitudes in the phased light curve, and so forth for the whole number of magnitudes in the the entire light curve as shown in Equation 3.3

$$\theta = \frac{\sum_{i=1}^{N-1}(m_i - m_{i+1})^2}{\sum_{i=1}^{N-1}(m_i - \overline{M})^2}, \tag{3.3}$$

where $\overline{M}$ is the mean magnitude, N is the number of data points, and θ is the total length of the light curve obtained by the sum of each of the straight lines defined between consecutive magnitudes for each trial period. Thus the period with the minimum value of θ (or shortest curve) is the best probable correct period of the star (Lafler & Kinman 1965). Similar string-length minimization approaches are also found in Burke et al. (1970) and Dworetsky (1983).

The uncertainties ΔP in the periods P obtained for each variable star (see Section 11.4 Warner 2006) were done considering the time span T of our observations which is the difference between the maximum and minimum Heliocentric Julian Day (hjd)

$$T = max(hjd) - min(hjd). \tag{3.4}$$

Finally, it was possible to calculate the uncertainty as

$$\frac{\Delta P}{P} = 0.1P/T. \tag{3.5}$$

3.6.3 Variable star classification

Once we had detected all the variable stars in the globular clusters and their period calculation was done it was necessary to define the type of variable star. This was done in two steps. First, we plotted the variables in the CMD, we already commented that variable stars are in a well defined section of the CMD. RR Lyrae are in the instability strip of the HB, SX Phoenicis are in the blue straggler zone, and so on. Second, we compared the periods and light curve shapes with catalogues and information already available in the literature describing the variability of the stars as presented in the introduction of this thesis. Only variables showing a clear pattern during these two steps were given a classification, otherwise they were labeled as unclassified variable (NC).

Chapter 4

Summary of Results

4.1 NGC 6715 / C1851-305 / Messier 54

The details of all variable stars in our FoV that are discussed in this section are listed in Table 4.1, and all light curves are plotted in Figure 4.2.

4.1.1 Known variables

This globular cluster has of the order of 200 known variable stars listed in the Catalogue of Variable Stars in Galactic Globular Clusters (**CVSGGC;** Clement et al. 2001). Most of them are of the RR Lyrae type but a few are long-period irregular, semi-regular, W Virginis, eclipsing binaries, and SX Phoenicis. To date four studies report variable star discoveries in this globular cluster: V1-V28 from Rosino (1952), V29-V82 from Rosino & Nobili (1958), V83-V117 from Layden & Sarajedini (2000b), and V118-V211 from Sollima et al. (2010).

In the field of view covered by our reference image there are only five known variable stars (V112, V160, V173, V181, V192). All of them lie towards the edges of the image as can be seen in Figure 2.6. The star V112 was previously classified as long-period irregular. However, we were able to find a period of ~ 100 days in the variability of this star and due to this we have reclassified it as a semi-regular variable. For V160, we were not able to produce a good phased light curve using the published period of 0.6194848 d. The discovery observations by Sollima et al. (2010) cover a time baseline of only 6 days. With our time baseline of more than two years, our derived periods are much more precise and the period found is in agreement with that found by the Optical Gravitational Lensing Experiment (OGLE, Udalski et al. 1992, see below). For V160, we list the OGLE period of 0.62813716 d in Table 4.1. For V173, we improved the period estimate over that from Sollima et al. (2010). For V181, we find a very different period with respect to the one estimated by Sollima et al. (2010). The new period of 0.877072 d makes this RR Lyrae the one with the longest period in the cluster. The phased light curve in Figure 4.2 is somewhat noisy because this variable is highly blended with a brighter star. The case of V192 is particularly interesting because the star was classified as RR1 with a period of 0.3986799 d. However, at the astrometric position reported for this star we found a RR Lyrae type RR0 with a period of 0.600373 d. This is also in agreement with the period and classification found by OGLE (see below) which we list in Table 4.1. Again, the phased light curve of this variable is noisy because of blending with a brighter star. It is clear then that the Sollima et al. (2010) periods and RR Lyrae classifications are not robust based on relatively few observations. We will discuss the consequences of this later on.

Recently, Montiel & Mighell (2010) announced 50 RR Lyrae candidates based on observations taken with the HST. However, the data obtained consist of 12 epochs covering only 8 hours, which made the study unsuitable for a period search and certainly some RR Lyrae stars will have been missed with such a short time baseline. No light curves were presented in their paper. Of these 50 candidate variable stars, 17 lie

outside of our field of view (VC2, VC11-VC18, VC22, VC24, VC38, VC44, VC45, VC47-VC49). As pointed out in the Catalogue of Variable Stars in Galactic Globular Clusters (Clement et al. 2001), 11 of these candidates are previously known variables, thus VC2=V127, VC11=V162, VC12=V163, VC13=V95, VC14=V164, VC15=V142, VC17=V129, VC18=V179, VC44=V46, VC45=V148, and VC47=V76 (see also Appendix C). For 8 of their candidates in our field of view, we could not detect variations in our difference images at their coordinates (VC3, VC6, VC19, VC21, VC29, VC42, VC43, VC50), and we therefore cannot confirm their variability. We plot their positions in Figure 2.6 with a green square[1]. Three of their candidates in our field of view, VC28, VC34 and VC46, are the known variables V181, V160 and V192, respectively. We confirm the variable nature of the remaining 22 candidates in our field of view, and we have assigned them "V" numbers as part of our study (see Section 4.1.2). Table 4.1 lists their VC identification in Column 2. We classify 18 of them as RR Lyrae stars, one as an eclipsing binary, and are unable to classify VC27, VC32, and VC33. We plot their positions in Figure 2.6 with a square symbol.

The study by McDonald et al. (2014) using the *VISTA*[2] surveys[3] also covered the cluster and presents candidate variables based on typically ∼12-13 epochs spread over ∼100-200 days, which was insufficient to derive periods for many of them. Of the short period candidate variables listed in their Table 1, 18 are inside the field of view covered by our reference image. None of the bright long-period variables listed in their Table 2 and faint candidates listed in their Table 3 are inside the field covered in our study. Positions of these stars inside our field of view are plotted in Figure 2.6 with a red circle. It is worth noting that all of these candidates are located more toward the edges of the reference image. We detect variability in only two of the McDonald et al. (2014) candidates within our field of view (SPVSgr18550405-3028580 and SPVSgr18550386-3028593, which we assign V identifications as V229 and V263, respectively -see Section 4.1.2).

Similarly, the field of this cluster was also covered by OGLE, particularly with their OGLE-IV survey (Udalski et al. 2015). We found in this survey 15 of the variable stars studied in our work of which two are previously known variables (V160 and V192) and 13 are new discoveries by OGLE (we assigned the following V identifications: V227-V229, V233, V236, V237, V240, V244, V246, V250-V253). The OGLE light curves for these stars have typically ∼150 epochs covering a baseline of ∼2.5 years and OGLE derived precise periods for them. With our data we were also able to find the same periods and type of classification assigned by OGLE. The positions of these stars are plotted in Figure 2.6 with a blue colour. Again, it is worth noticing that all of these variables are located more toward the edges of the reference image. In the particular case of V229, V244, and V246, the pipeline was not able to detect these stars in the reference image but their variation is clear in the difference images. Their differential fluxes against phase are plotted in Figure 4.2. Finally, epochs, periods, mean magnitudes, amplitudes, and classifications for these three stars were taken from the OGLE database, although the number of data points listed in Table 4.1 correspond to our light curves.

In Appendix C (Table C.1), we provide the cross identifications for the previously known RR Lyrae stars in NGC 6715 between the CVSGGC (Clement et al. 2001), the variable star candidates from Montiel & Mighell (2010), and the OGLE RR Lyrae stars (Udalski et al. 2015).

4.1.2 New variables

After employing the methods described in Section 3.5, we were able to extract 67 new variable stars in the core of NGC 6715 of which 30 are RR Lyrae, 1 is a W Virginis star (CWA), 21 are long-period irregular, 3 are semi regular, 1 is an eclipsing binary, and 11 remain without classification.

[1]The Montiel & Mighell (2010) coordinates differ by RA∼0.3″ and Dec∼0.8″ from our coordinates, and we have corrected for this in Figure 2.6

[2]https://www.eso.org/public/teles-instr/paranal-observatory/surveytelescopes/vista/

[3]https://www.eso.org/public/spain/teles-instr/paranal-observatory/surveytelescopes/vista/surveys/

RR Lyrae

V213-V226, V230-V232, V234-V235, V238-V239, V241-V243, V245, V247-V249, V254-V255: These 30 newly discovered variable stars are clear RR Lyrae variables. Their positions in the CMD, light curve shapes, periods, and amplitudes corroborate their variability type. We found that 17 are pulsating in the fundamental mode (RR0); 8 are pulsating in the first overtone (RR1); 1 is a double-mode pulsator (RR01) and 4 RR Lyrae remain with an uncetain subtype (3 RR0? and 1 RR1?). As shown in Table 4.1, their periods range from ∼0.28 d to ∼0.76 d with amplitudes between 0.06 and 1.69 mag.

The periodogram analysis for V221 showed two predominant frequencies typical of double mode RR Lyrae stars, one equivalent to the fundamental period $P_0 = 0.459608$ d and one equivalent to the first overtone period $P_1 = 0.343828$ d giving a period ratio $P_1/P_0 = 0.748$ which falls in the expected ratio range of ∼ 0.725 to ∼ 0.748 for this type of pulsating RR Lyrae stars (Netzel et al. 2015; Moskalik 2013; Cox et al. 1983).

W Virginis

V256: Particularly interesting is the case of this star as its variation (and position in the CMD) do not follow the pattern found for the other variable stars studied and classified in this work. We found a very well phased light curve with a period of ∼14.771 d and an amplitude of 0.71 mag. This is the only bright variable star on the blue side of the colour-magnitude diagram far away from the red giant branch.

The properties found in the variation of this star and its position in the CMD match very well with the W Virginis type of variable star described in Samus et al. (2009a), particularly with the subtype CWA which have periods longer than 8 days (see also Wallerstein 2002). Although these types of stars have not been commonly found in globular clusters in contrast to RR Lyrae stars, they are not entirely uncommon. In the statistics of variable stars in Galactic globular clusters reported by Clement et al. (2001) it is possible to notice that 60 variable stars are Cepheids, which include Population II Cepheids, anomalous Cepheids, and RV Tauri stars. V256 is the first CWA star discovered in this cluster.

Long-period irregular

V260-V280: These 21 stars are located at the top of the red giant branch as shown with blue squares in Figure 3.6. Their amplitudes range from 0.05 to 0.46 mag. We found no clear periods for these stars. Due to this and also their position in the colour-magnitude diagram we classified them as long-period irregular. Light curves for all these variables are found in Figure 4.2.

Semi regular

V257-V259: Based on the position of these 3 stars in the colour-magnitude diagram (see Fig. 3.6), their periods, and the shape of their light curves, we have classified them as semi-regular. Light curves for these variables may be found in Figure 4.2. Their amplitudes range from ∼0.04 to ∼0.45 mag and their periods span between ∼20 and ∼150 d.

Eclipsing Binary

V212: The light curve variations for this star are very similar to those presented in eclipsing binary systems. We found that the amplitude of the deeper eclipse is of the order of ∼0.8 mag and the amplitude of the secondary eclipse is ∼0.5 mag. The phased light curve shown in Figure 4.2 represented a period of P = 0.202144 d. This binary system is located on the blue side of the horizontal branch in color-magnitude diagram given in Figure 3.6 and more likely a cluster member.

Other variable stars

V281-V285: These 5 stars are clear variable stars. They show clear variability by blinking the difference images. They have amplitudes between 0.45 and 0.94 mag. Several attempts to determine periods for these stars were done without success. Due to this their light curves in Figure 4.2 are plotted against HJD. We note that the variable source V281 is ony ∼0.24 arcsec from the photometric centre of the cluster as measured by Goldsbury et al. (2010).

V286: Towards the beginning of the 2013 data, we found that the flux of this star was increasing to a maximum at ∼2456464.9081 d of about ∼39400 ADU/s on the flux scale of the reference image, corresponding to a peak magnitude of ∼15.04 mag. After that, its flux strongly decreased during the rest of the observational campaign. During 2014 and 2015, we found that the object seems to be at baseline and it is not detected in the original images.

The centre of NGC 6715 is ∼4.45 arcseconds from this source. Also, at a distance of 3.73 arcseconds, there is a X-ray source studied by Wrobel et al. (2011) using data from *Chandra* and *Hubble* Space Telescope. Given the relatively small astrometric uncertainties in these positions, V286 is not associated with either. The nature and classification of this variable will need further studies, and it will remain without classification in this work.

V287-V291: These 5 stars were not detected by the pipeline in the reference image. Unfortunately, there are no light curves available in the OGLE database for these stars, but their variations are clear in the difference images. In Figure 4.2 their differential fluxes against HJD are plotted. As we were not able to produce phased light curves for them, they will remain without classification until future studies are done.

4.2 Oosterhoff dichotomy

In this work we discovered 30 new RR Lyrae, and OGLE also discovered 17 more (of which 13 are inside our FoV). After removing the stars without a secure classification, there are 33 new RR0 and 9 new RR1 stars, which represent a significant increase in the known RR Lyrae population. The vast majority of these new RR Lyrae stars are cluster members since we have studied the core of NGC 6715. Hence it is pertinent to recalculate the mean periods and number ratios of the RR Lyrae stars to see if it modifies the current conclusions about the Oosterhoff type of NGC 6715.

However, we note that NGC 6715 lies projected against the Sagittarius Dwarf Spheroidal galaxy and behind the Galactic bulge. Therefore, the sample of RR Lyrae stars in the field of the cluster is a mixture of cluster members, Bulge stars, and Sgr dSph stars. Towards the centre of NGC 6715, the cluster member RR Lyraes dominate, but limiting our sample to the cluster core also reduces the number of RR Lyraes that can be used to calculate the mean periods and number ratios. Hence, in Figure 4.1, we have plotted the total number of RR Lyrae stars, the mean period of the RR0 stars, the mean period of the RR1 stars, and the number ratio of the RR1 to all RR Lyrae stars (nRR1/(nRR0 + nRR1)), all as a function of distance from the cluster centre (RA(J2000) = 18:55:03.33; Dec(J2000)=−30:28:47.5; Goldsbury et al. 2010). To convert angles on the sky into distances in parsecs we used the distance from the Sun to NGC 6715 of 26500 pc (Harris 1996, 2010 version). The inner and outer red vertical lines are the tidal radii estimated by McLaughlin & van der Marel (2005) based on King (1966) and Wilson (1975) models, respectively. The horizontal black lines correspond to the OoI (solid) and OoII (dashed) types given by (Smith 1995) in his Table 3.2. We only used RR Lyrae stars with certain classifications (i.e. published phased light curves with reliable period estimates).

Figure 4.1 clearly shows that within the range of the two estimates of the tidal radii, where the RR Lyrae stars from the cluster still dominate, the values of $\langle P_{\rm RR0}\rangle$, $\langle P_{\rm RR1}\rangle$ and nRR1/(nRR0 + nRR1) are intermediate between those expected for OoI and OoII clusters. We obtain $\langle P_{\rm RR0}\rangle$=0.613529 d, $\langle P_{\rm RR1}\rangle$=0.334107 d, and nRR1/(nRR0 + nRR1)= 0.24 when calculated for the 79 RR Lyraes within the outer estimate of the tidal radius (i.e. 380 pc). The contaminating RR Lyrae populations have ($\langle P_{\rm RR0}\rangle$, $\langle P_{\rm RR1}\rangle$)=(0.556 d, 0.310 d) and ($\langle P_{\rm RR0}\rangle$,$\langle P_{\rm RR1}\rangle$)=(0.574 d, 0.322 d) for the Bulge and Sgr dSph, respectively (Soszyński et al. 2011; Cseresnjes 2001), placing them in the OoI region in the $\langle P_{\rm RR0}\rangle$-metallicity diagram of Catelan (2009). This

explains why the values of $\langle P_{\rm RR0} \rangle$ and nRR1/(nRR0 + nRR1) tend towards the OoI values beyond the outer estimate of the tidal radius. The value of $\langle P_{\rm RR1} \rangle$ is hardly influenced though because there are only 6 RR1 stars beyond the outer estimate of the tidal radius. Hence the new RR Lyrae discoveries in this paper have served to confirm that NGC 6715 is of intermediate Oosterhoff type.

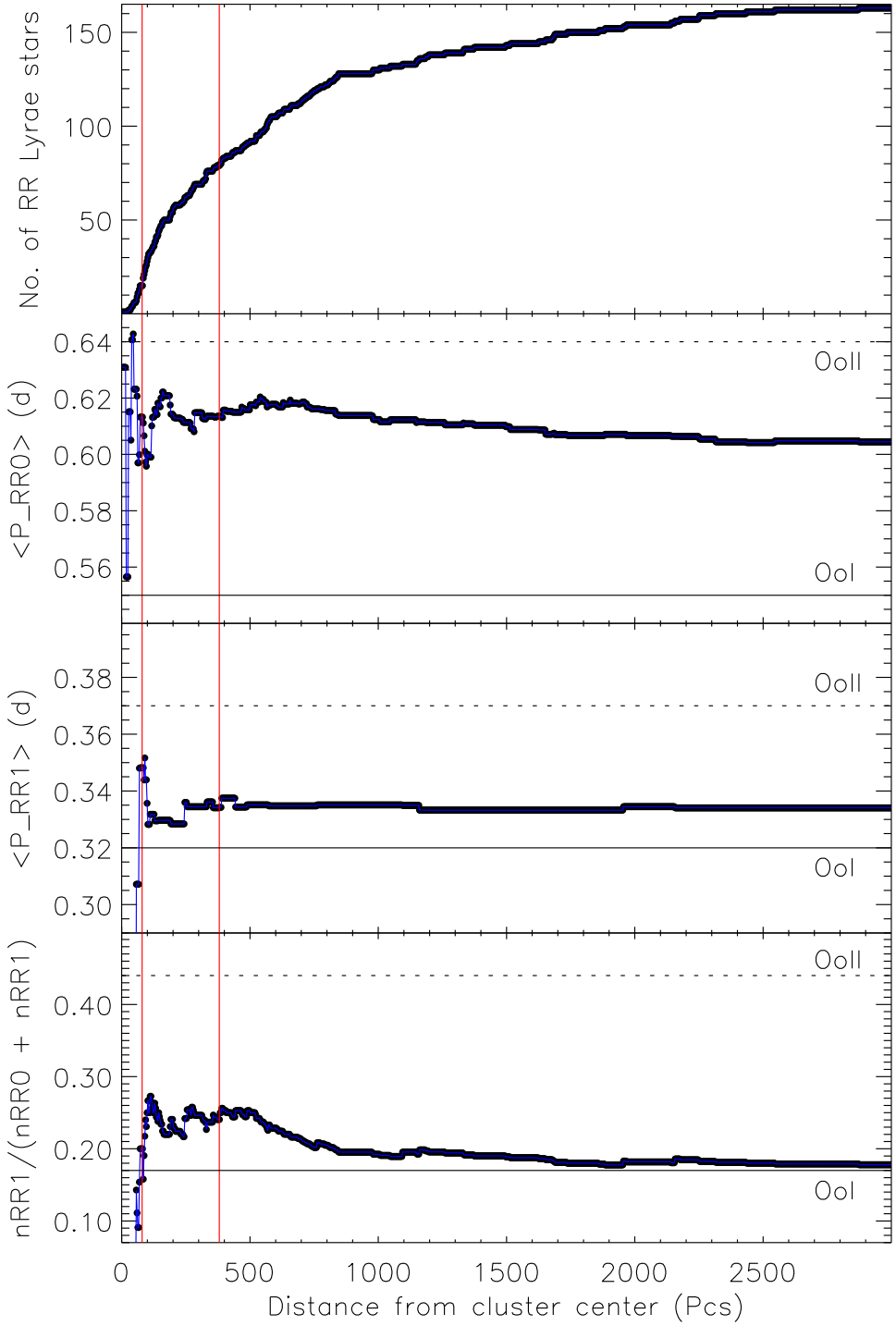

Figure 4.1: The number of RR Lyraes, mean periods, and number ratios as a function of the distance from the cluster centre. The red lines correspond to the tidal radii calculated by McLaughlin & van der Marel (2005).

Table 4.1: Ephemerides and main characteristics of the variable stars in the field of globular cluster NGC 6715. Column 1 is the id assigned to the variable star, Column 2 is a previously known id assigned to the stars (5 digit numbers correspond to OGLE identifications of the form OGLE-BLG-RRLYR-*NNNNN*), Columns 3 and 4 correspond to the right ascension and declination (J2000), Column 5 is the epoch used, Column 6 is the period measured in this work unless the variable is an OGLE star in which case we use their period, Column 7 is median magnitude, Column 8 is the peak-to-peak amplitude in the light curve, Column 9 is the number of epochs and Column 10 is the classification of the variable. The numbers in parentheses indicate the uncertainty on the last decimal place of the period.

Var id (1)	Other id (2)	RA J2000 (3)	Dec J2000 (4)	Epoch HJD (5)	P d (6)	I_{median} mag (7)	$A_{i'+z'}$ mag (8)	N (9)	Type (10)
V112	-	18:55:02.010	-30:28:35.13	2457190.7419	100(1)	13.63	0.34	44	SR
V160	VC34; 37595	18:55:03.954	-30:28:29.83	2457189.7725	0.62813716(382)	17.65	0.75	40	RR0
V173	-	18:55:02.473	-30:29:00.04	2457206.6555	0.360284(152)	17.69	0.30	44	RR1
V181	VC28	18:55:02.395	-30:28:34.20	2457145.9107	0.877072(898)	17.60	0.87	42	RR0
V192	VC46; 37568	18:55:01.973	-30:29:02.27	2456784.9179	0.60035438(1060)	17.63	0.60	44	RR0
V212	VC35	18:55:03.777	-30:29:03.51	2457214.8470	0.202144(48)	17.59	0.79	42	E
V213	VC40	18:55:02.126	-30:28:39.63	2456771.8623	0.286053(96)	17.95	0.64	44	RR1
V214	VC39	18:55:02.964	-30:28:35.37	2456765.9179	0.305386(109)	16.97	0.45	44	RR1
V215	VC25	18:55:02.701	-30:28:52.71	2456789.8857	0.307160(110)	17.45	0.34	44	RR1
V216	VC9	18:55:04.011	-30:28:37.73	2457292.6392	0.331073(128)	16.49	0.20	44	RR1
V217	-	18:55:02.070	-30:29:03.41	2457205.7553	0.331556(128)	17.76	0.35	44	RR1
V218	-	18:55:03.556	-30:28:56.77	2456891.5200	0.348450(142)	16.92	0.20	44	RR1
V219	-	18:55:03.233	-30:28:59.48	2457183.7770	0.382637(171)	17.21	0.24	44	RR1
V220	VC4	18:55:03.197	-30:28:38.54	2456765.9102	0.388893(177)	16.86	0.27	44	RR1
V221	VC8	18:55:04.353	-30:28:51.16	2456846.9179	0.459608(247)	17.39	0.71	44	RR01
V222	-	18:55:02.504	-30:28:46.40	2456765.9179	0.465653(253)	17.70	0.70	44	RR0?
V223	VC10	18:55:02.425	-30:28:45.20	2456823.8857	0.471901(260)	17.63	0.81	44	RR0
V224	VC20	18:55:03.549	-30:28:45.09	2457292.6392	0.482336(272)	16.16	0.27	44	RR0?
V225	VC37	18:55:03.862	-30:28:43.86	2456464.9081	0.483029(272)	17.28	0.35	44	RR1?
V226	-	18:55:03.948	-30:28:42.65	2456784.9179	0.497941(289)	16.39	0.36	44	RR0?
V227	37582	18:55:03.050	-30:28:35.81	2457190.7991	0.50805795(495)	17.66	0.90	44	RR0
V228	37575	18:55:02.757	-30:28:50.88	2456534.6709	0.52522562(844)	16.87	0.41	44	RR0
V229[a]	37597; [b]	18:55:04.033	-30:28:58.20	2456788.9321	0.52679780(281)	16.38	0.28	41	RR0
V230	-	18:55:03.637	-30:28:55.39	2456465.8700	0.532617(331)	16.04	0.29	44	RR0
V231	-	18:55:02.894	-30:28:58.30	2457189.8090	0.534194(333)	17.80	0.83	44	RR0
V232	VC41	18:55:03.581	-30:28:47.60	2456543.5260	0.556536(362)	16.35	0.29	44	RR0
V233	VC30; 37591	18:55:03.735	-30:28:40.24	2456846.9179	0.55752742(766)	17.41	0.93	44	RR0
V234	VC7	18:55:02.255	-30:28:37.13	2457206.6400	0.559765(366)	17.72	0.60	44	RR0
V235	-	18:55:03.411	-30:29:05.75	2457292.6392	0.566711(375)	17.41	0.69	43	RR0
V236	VC36; 37585	18:55:03.149	-30:28:34.86	2457152.8500	0.56847125(715)	16.53	0.28	44	RR0
V237	VC31; 37570	18:55:02.112	-30:28:44.40	2456435.8882	0.57985290(735)	17.57	0.65	44	RR0
V238	-	18:55:03.242	-30:28:42.94	2456846.9179	0.584918(399)	17.63	1.69	44	RR0
V239	-	18:55:02.848	-30:29:06.91	2457189.8090	0.596179(432)	17.57	0.69	39	RR0
V240	37576	18:55:02.725	-30:28:30.46	2456909.5275	0.59629933(890)	17.06	0.54	43	RR0
V241	VC1	18:55:04.190	-30:28:39.15	2456896.5087	0.602588(424)	17.79	0.65	44	RR0
V242	-	18:55:02.756	-30:29:00.15	2456891.4700	0.604762(427)	16.23	0.16	44	RR0
V243	-	18:55:02.587	-30:28:38.62	2456770.8691	0.610170(435)	16.97	0.36	44	RR0
V244[a]	37581	18:55:03.031	-30:29:01.15	2456891.4945	0.61517949(819)	16.90	0.27	44	RR0
V245	VC26	18:55:02.849	-30:28:57.81	2456771.8623	0.626797(459)	17.68	0.47	44	RR0

[a]Epochs, periods, mean magnitudes, amplitudes, and classifications taken from OGLE database
[b]=SPVSgr18550405-3028580; [c]=SPVSgr18550386-3028593; [d]=Peak magnitude

Continued on next page

Continued from previous page

Var id (1)	Other id (2)	RA J2000 (3)	Dec J2000 (4)	Epoch HJD (5)	P d (6)	I_{median} mag (7)	$A_{i'+z'}$ mag (8)	N (9)	Type (10)
V246[a]	37573	18:55:02.616	-30:28:40.91	2457207.8691	0.62879467(894)	16.11	0.06	42	RR0
V247	-	18:55:02.826	-30:28:43.51	2456846.9179	0.650946(495)	16.86	0.42	44	RR0
V248	-	18:55:03.795	-30:28:54.42	2457258.7147	0.668967(522)	17.05	0.46	44	RR0
V249	-	18:55:03.226	-30:28:43.99	2457191.7238	0.673703(530)	15.91	0.21	44	RR0
V250	VC23; 37590	18:55:03.705	-30:29:00.36	2456543.5260	0.68064951(790)	17.54	0.58	44	RR0
V251	37579	18:55:02.876	-30:28:30.48	2457189.7725	0.68928616(716)	17.54	0.88	43	RR0
V252	37593	18:55:03.792	-30:29:07.83	2457189.8090	0.72866844(702)	17.28	0.50	17	RR0
V253	37586	18:55:03.268	-30:28:28.69	2457206.6555	0.74391157(1160)	17.32	0.29	17	RR0
V254	-	18:55:02.808	-30:28:49.69	2456436.8969	0.747628(652)	17.06	0.71	44	RR0
V255	VC5	18:55:03.123	-30:28:37.99	2456765.8300	0.760088(674)	16.48	0.19	44	RR0
V256	-	18:55:03.730	-30:28:44.94	2456784.9179	14.771(25)	14.72	0.71	44	CWA
V257	-	18:55:02.996	-30:28:43.18	2456823.8857	20.747(50)	14.04	0.09	44	SR
V258	-	18:55:03.732	-30:28:48.34	2457224.5000	37.980(168)	13.16	0.04	44	SR
V259	-	18:55:04.216	-30:28:49.91	2456464.9081	154(3)	13.30	0.45	44	SR
V260	-	18:55:03.170	-30:28:54.44	–	–	12.76	0.06	44	L
V261	-	18:55:03.399	-30:28:44.99	–	–	13.78	0.07	44	L
V262	-	18:55:01.876	-30:28:43.79	–	–	13.99	0.07	40	L
V263	[c]	18:55:03.877	-30:28:59.31	–	–	14.71	0.07	44	L
V264	-	18:55:03.753	-30:28:49.36	–	–	13.87	0.08	44	L
V265	-	18:55:02.987	-30:28:51.96	–	–	14.00	0.08	44	L
V266	-	18:55:03.458	-30:28:46.47	–	–	14.04	0.08	44	L
V267	-	18:55:03.463	-30:28:45.05	–	–	13.66	0.09	44	L
V268	-	18:55:02.998	-30:28:44.30	–	–	13.79	0.09	44	L
V269	-	18:55:03.712	-30:28:43.08	–	–	13.62	0.10	44	L
V270	-	18:55:02.603	-30:28:48.92	–	–	13.70	0.11	44	L
V271	-	18:55:04.004	-30:28:37.05	–	–	13.97	0.12	44	L
V272	-	18:55:03.065	-30:28:47.99	–	–	14.25	0.05	44	L
V273	-	18:55:03.708	-30:28:35.30	–	–	13.40	0.15	44	L
V274	-	18:55:03.833	-30:29:03.89	–	–	13.47	0.08	44	L
V275	-	18:55:02.346	-30:28:43.40	–	–	13.67	0.16	44	L
V276	-	18:55:03.659	-30:28:50.52	–	–	14.06	0.16	44	L
V277	-	18:55:03.309	-30:28:49.79	–	–	13.71	0.19	44	L
V278	-	18:55:04.070	-30:28:49.79	–	–	13.13	0.33	44	L
V279	-	18:55:04.045	-30:28:41.41	–	–	13.42	0.34	44	L
V280	-	18:55:03.692	-30:28:52.01	–	–	13.25	0.46	44	L
V281	-	18:55:03.324	-30:28:47.26	–	–	16.71	0.45	44	NC
V282	-	18:55:03.010	-30:28:35.82	–	–	17.52	0.74	44	NC
V283	-	18:55:03.747	-30:28:53.88	–	–	16.97	0.76	44	NC
V284	VC32	18:55:03.367	-30:28:37.97	–	–	17.14	0.94	44	NC
V285	VC33	18:55:02.686	-30:28:32.48	–	–	17.52	0.55	44	NC
V286	-	18:55:03.536	-30:28:51.06	–	–	15.04[d]	–	43	NC
V287	-	18:55:03.373	-30:28:35.86	–	–	–	–	44	NC
V288	-	18:55:03.412	-30:28:52.76	–	–	–	–	44	NC
V289	-	18:55:02.904	-30:28:39.89	–	–	–	–	42	NC
V290	-	18:55:03.475	-30:29:06.23	–	–	–	–	39	NC
V291	VC27	18:55:03.258	-30:28:41.09	–	–	–	–	42	NC

[a]Epochs, periods, mean magnitudes, amplitudes, and classifications taken from OGLE database
[b]=SPVSgr18550405-3028580; [c]=SPVSgr18550386-3028593; [d]=Peak magnitude

Concluded

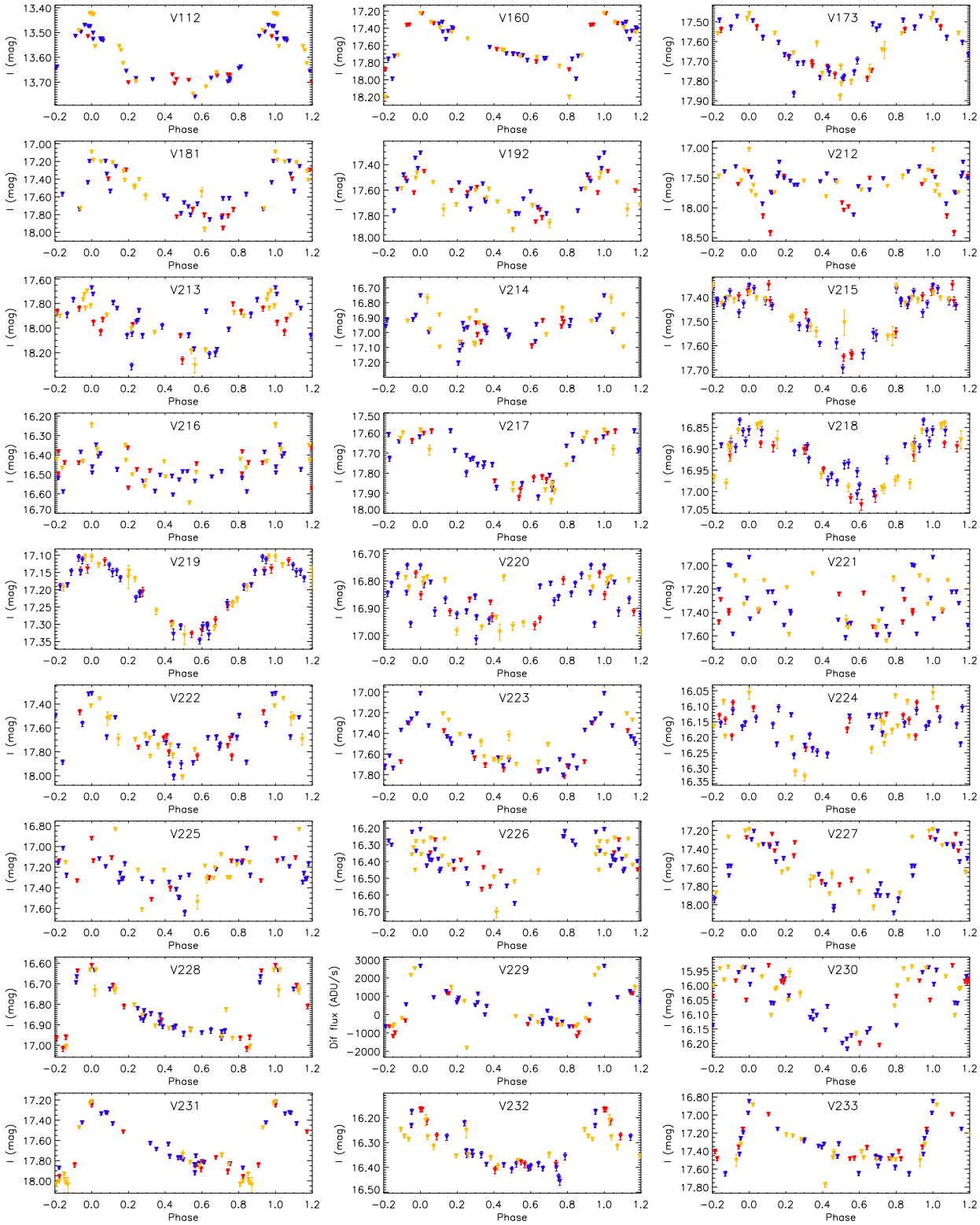

Figure 4.2: (a) Light curves of the known and new variables discovered in globular cluster NGC 6715. Red, blue, and yellow triangles correspond to the data obtained during the years 2013, 2014, and 2015, respectively. For V229, V244, V246, V286-V291, we plot the quantity $f_{\rm diff}(t)/p(t)$ since a reference flux is not available.

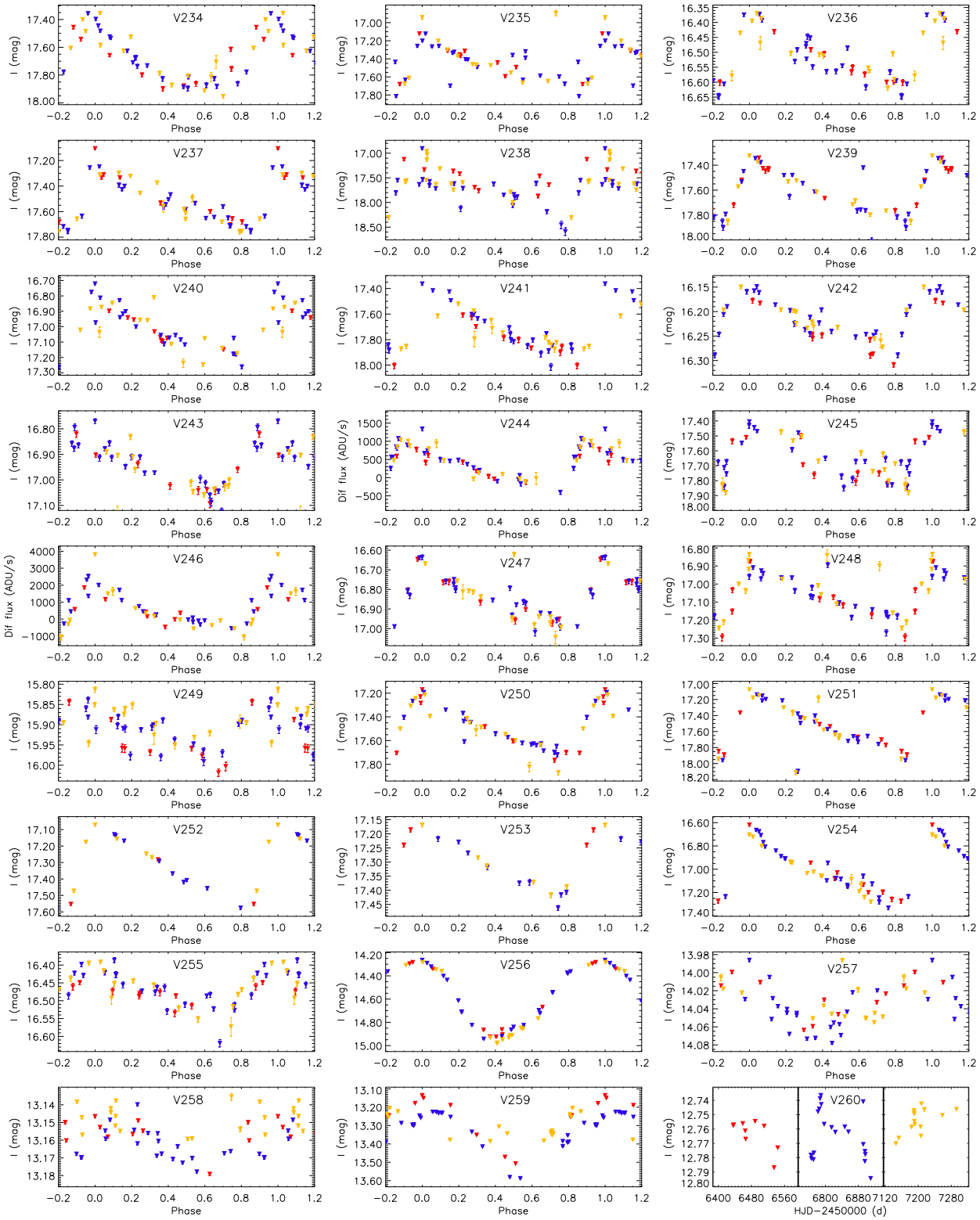

Figure 4.2: (b) Light curves of the known and new variables discovered in globular cluster NGC 6715. Red, blue, and yellow triangles correspond to the data obtained during the years 2013, 2014, and 2015, respectively. For V229, V244, V246, V286-V291, we plot the quantity $f_{\rm diff}(t)/p(t)$ since a reference flux is not available.

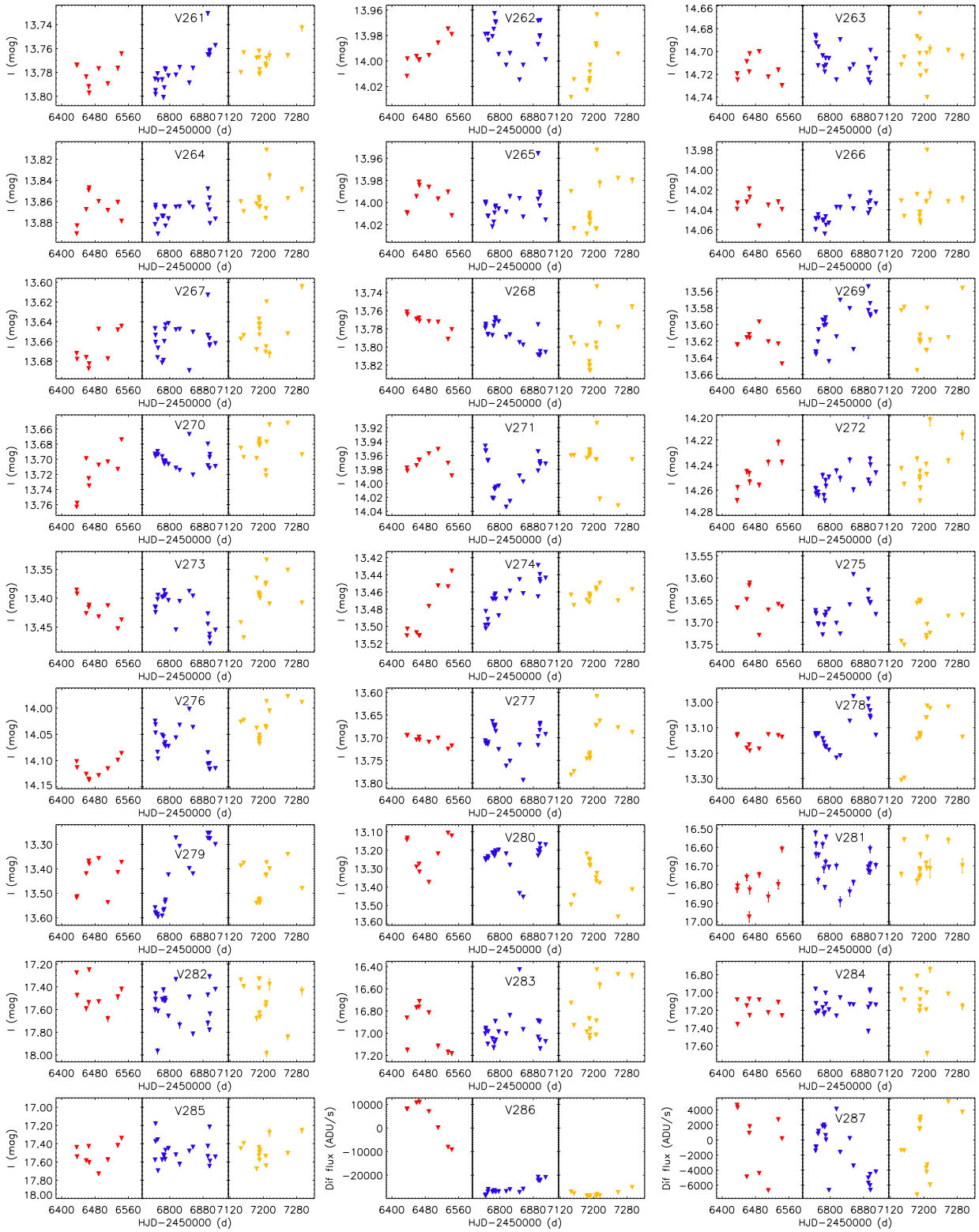

Figure 4.2: (c) Light curves of the known and new variables discovered in globular cluster NGC 6715. Red, blue, and yellow triangles correspond to the data obtained during the years 2013, 2014, and 2015, respectively. For V229, V244, V246, V286-V291, we plot the quantity $f_{\rm diff}(t)/p(t)$ since a reference flux is not available.

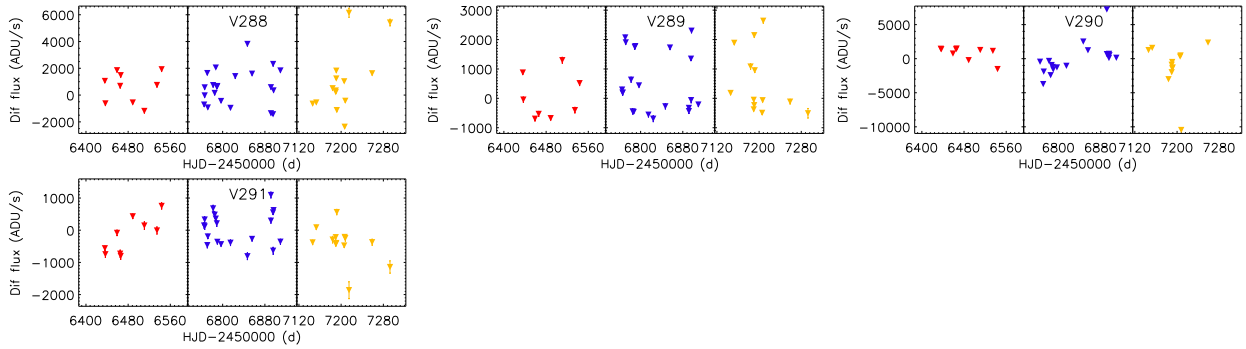

Figure 4.2: (d) Light curves of the known and new variables discovered in globular cluster NGC 6715. Red, blue, and yellow triangles correspond to the data obtained during the years 2013, 2014, and 2015, respectively. For V229, V244, V246, V286-V291, we plot the quantity $f_{\rm diff}(t)/p(t)$ since a reference flux is not available.

4.3 NGC 104 / C0021-723 / 47 Tucanae

This globular cluster was catalogued by Nicholas Louis de Lacaille in 1751[4]. The cluster is in the constellation of Tucana at a distance of 4.5 kpc from the Sun and 7.4 kpc from the Galactic centre. It has a metallicity of [Fe/H]=−0.72 dex and a distance modulus of $(m-M)_V$=13.37 mag. The magnitude of its horizontal branch is V_{HB}=14.06 mag.

Table 4.2: NGC 104: Ephemerides and main characteristics of the variable stars in the field of this globular cluster. Column 1 is the id assigned to the variable star, Columns 2 and 3 correspond to the right ascension and declination (J2000), Column 4 is the epoch used, Column 5 is the period, Column 6 is median of the data, Column 7 is the peak-to-peak amplitude in the light curve, Column 8 is the number of epochs and Column 9 is the classification of the variable. The numbers in parentheses indicate the uncertainty on the last decimal place of the period.

Var id	RA	Dec	Epoch	P	I_{median}	$A_{i'+z'}$	N	Type
	J2000	J2000	HJD	d	mag	mag		
PC1-V12	00:24:05.921	-72:04:45.20	–	–	15.62	1.10	149	NC
WF2-V34	00:24:08.406	-72:04:35.91	–	–	10.98	0.03	139	L
LW10	00:24:02.490	-72:05:07.45	–	–	9.60	0.24	108	L
LW11	00:24:03.145	-72:04:50.60	2456920.7253	19.37(8)	10.18	0.08	141	SR
LW12	00:24:03.982	-72:05:10.06	–	–	9.57	0.09	41	L
EM1	00:24:03.065	-72:04:55.02	2456491.9380	20.28(9)	10.26	0.05	145	SR
EM2	00:24:06.269	-72:04:45.36	2456530.7986	31.50(22)	9.98	0.08	140	SR
EM3	00:24:08.310	-72:04:50.69	2456847.9667	33.41(24)	10.07	0.05	134	SR
EM4	00:24:07.203	-72:04:46.45	2456498.9086	68.07(102)	13.89	0.14	149	SR
EM5	00:24:05.087	-72:04:54.38	–	–	10.34	0.06	145	L
EM6	00:24:02.733	-72:05:02.80	–	–	10.60	0.07	147	L
EM7	00:24:07.885	-72:05:02.00	–	–	–	–	146	NC

In Fig. 4.3, the root mean square magnitude deviation (top) and S_B statistic (bottom) are plotted versus the mean I magnitude for a total of 575 light curves extracted in this analysis. The marked coloured points correspond to the variable stars studied in this work in comparison with the stars where no variation is found (normal black points).

[4]http://messier.seds.org/xtra/ngc/n0104.html

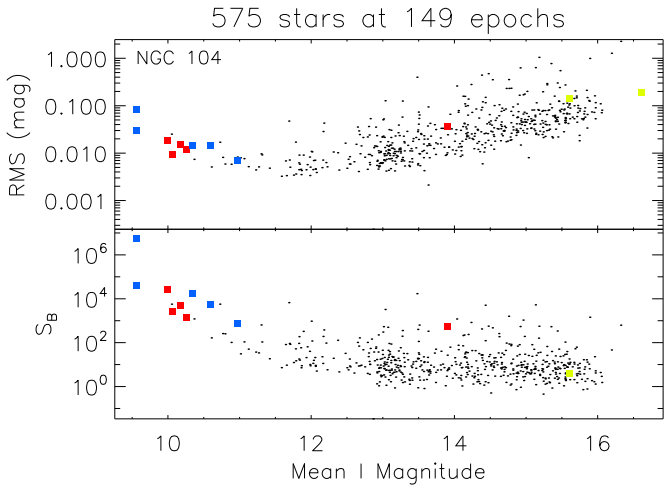

Figure 4.3: Root mean square (RMS) magnitude deviation (top) and S_B statistic (bottom) versus the mean I magnitude for the 575 stars detected in the field of view of the reference image for NGC 104. Coloured points follow the convention adopted in Tab. 3.1 to identify the types of variables found in the field of this globular cluster.

4.3.1 Known variables

This globular cluster has of the order of 300 known variable sources in the Catalogue of Variable Stars in Galactic Globular Clusters (version of summer 2007; Clement et al. 2001) which include long-period irregular variables, SX Phoenicis, RR Lyrae and binary systems. Most were found by Albrow et al. (2001), Weldrake et al. (2004) and Lebzelter & Wood (2005). There are also 20 millisecond pulsars listed in the literature for this cluster (Freire et al. 2001). However, no visual counterparts have been found at their positions.

In the field of view covered by the reference image (Fig. 4.5) there are 49 previously known variables. However, for this cluster we were only able to detect stars brighter than I=16.1 mag (see RMS in Fig. 4.3). Due to this, 5 known variable stars brighter than this limit were detected. These stars are labelled in the literature as PC1-V12, WF2-V34, LW10, LW11 and LW12. Our light curves for these variables can be found in Fig. 4.6.

PC1-V12: This star was discovered by Albrow et al. (2001) and classified as a Blue Straggler star (BSS) with an average magnitude of V=16.076 mag. No period was reported in this case and it was not possible to find a period for this star in the present work.

WF2-V34: The variability of this star was found by Albrow et al. (2001) and was classified as a semi-regular variable with a period of P=5.5 d. However, using this period it was not possible to produce a good phased light curve and it was not possible to find another period for this star. Based on this, we classified this star as long-period irregular variable.

LW10-LW12: These three stars were discovered by Lebzelter & Wood (2005). Their positions in the colour-magnitude diagram (Fig. 4.4) confirm their cluster membership. Lebzelter & Wood (2005) classified them as long-period irregular variables and suggested periods for these stars to be LW10: 110 d or 221 d; LW11: 36.0 d, and LW12 : 61 d or 116 d. However, LW10 and LW12 are clearly irregular variables (see our Fig. 7, and Fig. 1 from Lebzelter & Wood (2005)). For LW11 we found a period of 19.37 d and we classify it as semi-regular.

4.3.2 New variables

After extracting and analysing all possible variable sources in the field of our images, a total of 7 new variables (EM1-EM7) were found of which 4 are semi-regular variables, 2 are long-period irregular variables

and 1 is unclassified.

For this cluster, the nomenclature employed for most of the variable stars discovered in previous works does not correspond to the typical numbering system (e. g. V1, V2, V3, ..., Vn). For example, variables discovered by Lebzelter & Wood (2005) and Weldrake et al. (2004) are numbered using their initials LW and W, respectively; Albrow et al. (2001) used a PC or WF nomenclature making reference to the instrument employed during the observations. Due to this, we did not find it practical to assign the typical numbering system to the new variable stars discovered in this work and we decided to use as reference the EMCCD camera used in the observations. That is, new variables are numbered as EM1-EM7.

EM1-EM4: These variable stars are placed at the top of the colour magnitude diagram (Fig. 4.4), their light curve shape, amplitudes and periods found suggest that these stars are semi-regular variables. Periods found for these variables are listed in Tab. 4.2. The star EM1 is not over the red giant branch in Fig. 4.4 but instead it is more toward the asymptotic giant branch, it appears at the top on the left. Finally the star EM4 is located at the bottom part of the red giant branch just below the starting point of the horizontal branch.

EM5-EM6: These stars have amplitudes of ~0.06 and 0.07 mag, respectively. They are located at the top of the red giant branch. We were not able to determine a proper period for these stars. Due to this, we classified them as long-period irregular variables.

EM7: This star is placed in the Blue Straggler region. The variation in the difference images is clear for this star. However, the pipeline did not find this star in the reference image and no reference flux is available to convert the difference fluxes to magnitudes. The difference fluxes are plotted in Fig. 4.6. We were unable to determine a period.

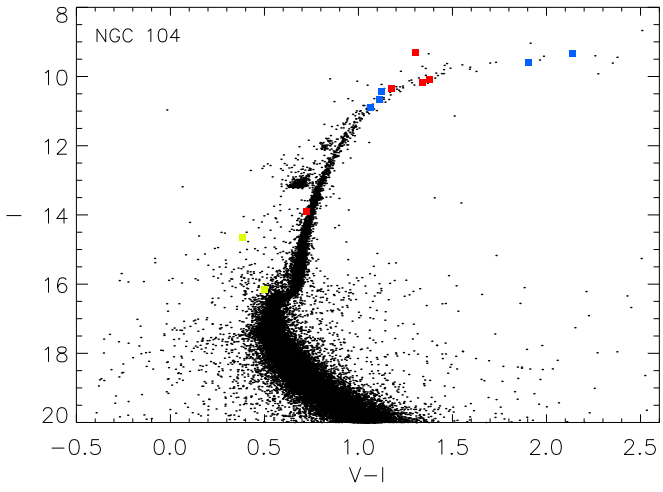

Figure 4.4: Colour magnitude diagram for the globular cluster NGC 104 built with V and I magnitudes available in the ACS globular cluster survey extracted from HST images. The variable stars are plotted in colour following the convention adopted in Tab. 3.1.

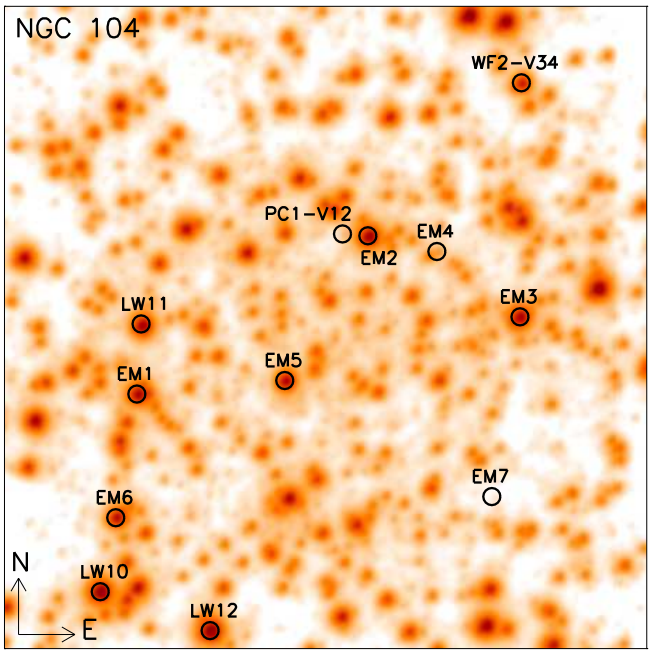

Figure 4.5: Finding chart for the globular cluster NGC 104. The image used corresponds to the reference image constructed during the reduction. All known variables and new discoveries are labelled. Image size is $\sim 41 \times 41$ arcsec^2.

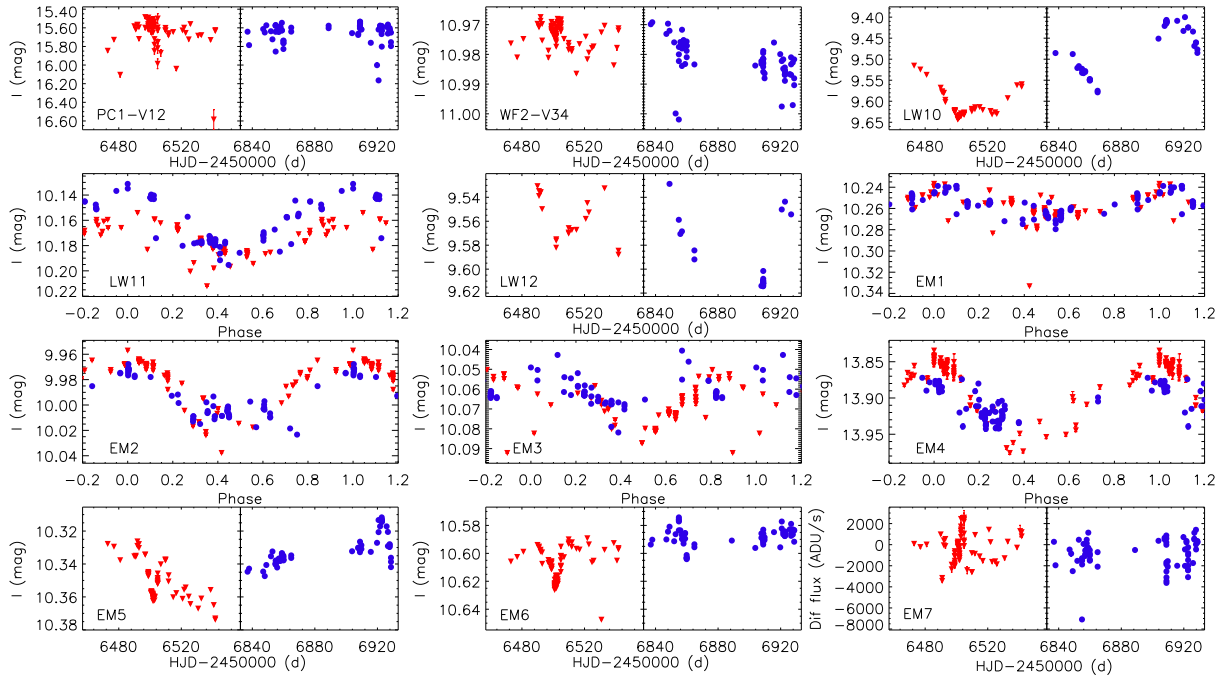

Figure 4.6: NGC 104: Light curves of the known and new variables discovered in this globular cluster. Red triangles correspond to the data obtained during the year 2013 and blue circles correspond to the data obtained during the year 2014. For EM7, we plot the quantity $f_{\rm diff}(t)/p(t)$ since a reference flux is not available.

4.4 NGC 5139 / C1323-472/ Omega Centauri

This globular cluster was catalogued by Edmond Halley in 1677[5]. The cluster is in the constellation of Centaurus at 5.2 kpc from the Sun and 6.4 kpc from the Galactic centre. It has a metallicity of [Fe/H]=-1.53 dex, a distance modulus of $(m\text{-}M)_V$=13.94 mag and the level of the horizontal branch is at V_{HB}=14.51 mag.

Table 4.3: NGC 5139: Ephemerides and main characteristics of the variable stars in the field of this globular cluster. Columns are the same as in Tab. 4.2.

Var id	RA	Dec	Epoch	P	I_{median}	$A_{i'+z'}$	N	Type
	J2000	J2000	HJD	d	mag	mag		
V457	13:26:46.246	-47:28:44.81	–	–	15.82	0.15	78	NC
V458	13:26:46.103	-47:28:57.05	–	–	10.21	0.04	78	L
V459	13:26:46.313	-47:28:40.33	–	–	10.98	0.06	78	L

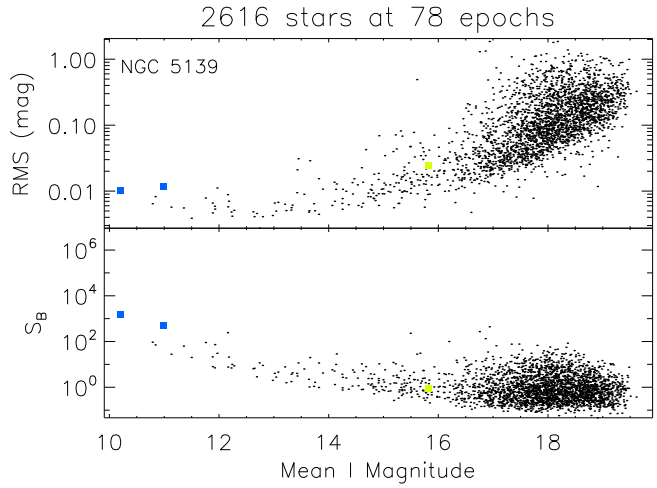

Figure 4.7: Root mean square (RMS) magnitude deviation (top) and S_B statistic (bottom) versus the mean I magnitude for the 2616 stars detected in the field of view of the reference image for NGC 5139. Coloured points follow the convention adopted in Tab. 3.1 to identify the types of variables found in the field of this globular cluster.

4.4.1 Known variables

In the Catalogue of Variable Stars in Galactic Globular Clusters (Clement et al. 2001) there are of the order of 400 variable stars for this globular cluster. Most of these variables were discovered by Bailey (1902), Kaluzny et al. (2004) and Weldrake et al. (2007). All of the known variables are outside the field of view of our reference image. Most recently, Navarrete et al. (2015) made an updated analysis of the variables in this cluster but the variables in their study are also located outside the field of view of our reference image.

4.4.2 New variables

We have found 3 new variables in this globular cluster. Two are long-period irregular variables and one is unclassified.

The new variable stars are plotted in the RMS diagram and S_B statistic (see Fig. 4.7). Based on the position of the stars in Figs. 4.7 and 4.8 there is no evidence of RR Lyrae in the field covered by this work neither in the inspection of the difference images obtained in the reductions.

[5]http://messier.seds.org/xtra/ngc/n5139.html

V457: This variable star has an amplitude of ~0.15 mag with a median magnitude I =15.82 mag. It lies on the RGB and we were unable to find a period.

V458, V459: Theses two stars are at the top of the red giant branch in Fig. 4.8 and have amplitudes of ~0.04 and ~0.06 mag, respectively. No periods were found in this work. V459 is on the red side of the main red giant branch. We classify them as long-period irregular variables.

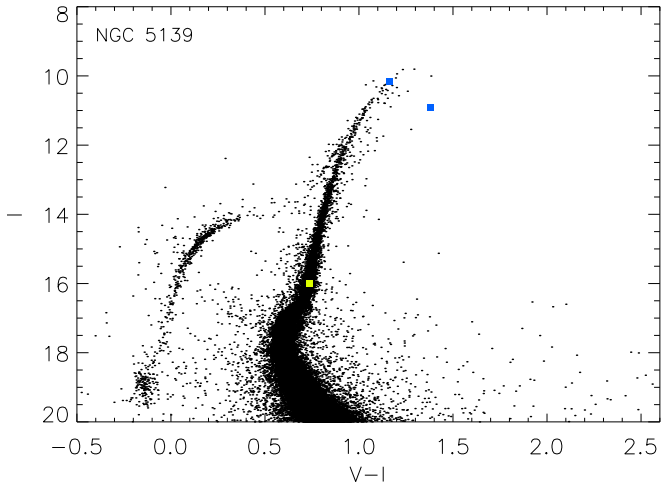

Figure 4.8: Colour magnitude diagram of the globular cluster NGC 5139 built with V and I magnitudes available in the ACS globular cluster survey extracted from HST images. The variable stars are plotted in colour following the convention adopted in Tab. 3.1.

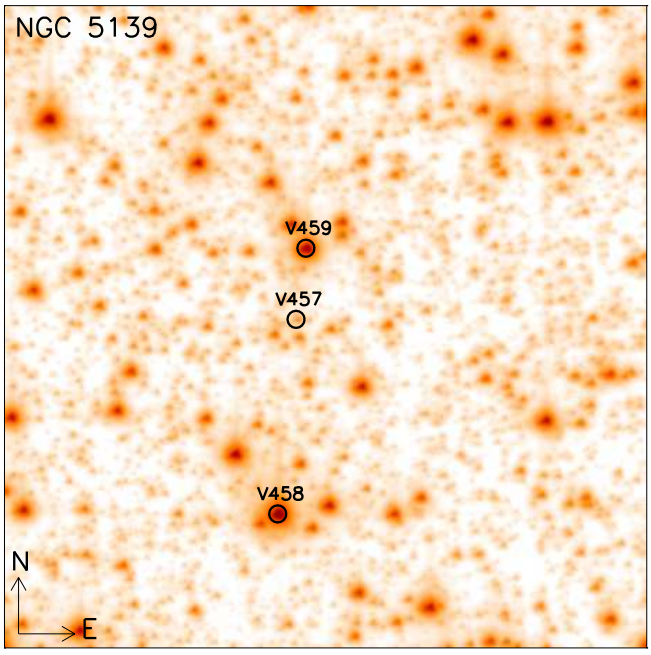

Figure 4.9: Finding chart for the globular cluster NGC 5139. The image used corresponds to the reference image constructed during the reduction. The new variables discovered are labelled. Image size is $\sim 41 \times 41$ arcsec^2.

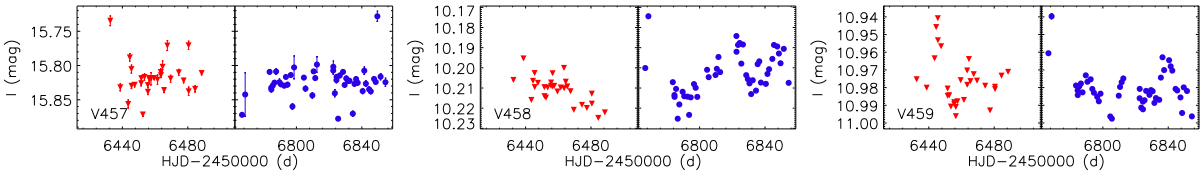

Figure 4.10: NGC 5139: Light curves of the 3 new variables discovered in this globular cluster. Symbols are the same as in Fig. 4.6.

4.5 NGC 5286 / C1343-511 / Caldwell 84

This globular cluster was catalogued by James Dunlop in 1827 (O'Meara 2002). It is in the constellation of Centaurus at 11.7 kpc from the Sun and 8.9 kpc from the Galactic centre. It has a metallicity of [Fe/H]=-1.69 dex, a distance modulus of $(m\text{-}M)_V$=16.08 mag and the magnitude level of the horizontal branch is at V_{HB}=16.63 mag.

In Fig. 4.11, the RMS diagram and the S_B statistic are shown for the sample of 1903 stars analysed in this globular cluster. Most of them have 74 epochs. All variable stars studied in this work are plotted using the colour classification given in Tab. 3.1.

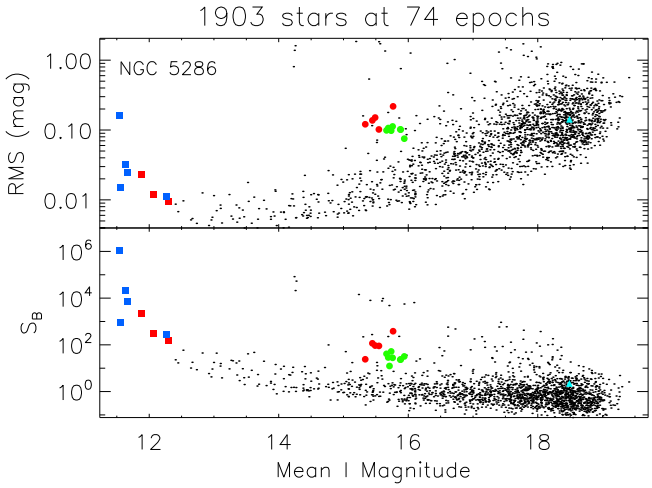

Figure 4.11: Root mean square (RMS) magnitude deviation (top) and S_B statistic (bottom) versus the mean I magnitude for the 1903 stars detected in the field of view of the reference image for NGC 5286. Coloured points follow the convention adopted in Tab. 3.1 to identify the types of variables found in the field of this globular cluster.

Table 4.4: NGC 5286: Ephemerides and main characteristics of the variable stars in the field of this globular cluster. Columns are the same as in Tab. 4.2.

Var id	RA	Dec	Epoch	P	I_{median}	$A_{i'+z'}$	N	Type
	J2000	J2000	HJD	d	mag	mag		
V37	13:46:27.275	-51:22:51.63	2456847.4835	0.583886(85)	15.92	0.81	52	RR0
V39	13:46:25.458	-51:22:46.81	2456768.6823	0.742099(136)	15.57	0.36	74	RR0
V40	13:46:26.917	-51:22:44.21	2456455.5615	0.365961(33)	15.76	0.30	74	RR1
V41	13:46:26.577	-51:22:42.92	2456822.5630	0.322262(26)	15.88	0.42	74	RR1
V43	13:46:26.730	-51:22:38.08	2456447.5363	0.658478(107)	15.47	0.50	74	RR0
V46	13:46:27.470	-51:22:33.93	2456831.5372	0.682690(115)	15.52	0.56	74	RR0
V50	13:46:25.984	-51:22:30.32	2456457.5131	0.365145(33)	15.71	0.41	74	RR1
V55	13:46:25.403	-51:22:25.79	2456841.5096	0.288925(21)	15.91	0.30	74	RR1
V56	13:46:25.112	-51:22:24.34	2456783.6351	0.283202(20)	15.97	0.22	74	RR1
V57	13:46:27.785	-51:22:20.69	2456833.6352	0.294964(22)	15.75	0.40	74	RR1
V58	13:46:26.627	-51:22:19.29	2456463.5240	0.367064(33)	15.65	0.30	74	RR1
V63	13:46:25.405	-51:22:44.92	2456811.5275	0.0486320(10)	18.52	0.55	74	SXPhe
V64	13:46:26.780	-51:22:26.60	2456833.6900	0.369783(34)	15.72	0.41	74	RR1
V65	13:46:26.763	-51:22:28.93	2456461.4946	0.619491(95)	15.35	**0.36**	74	RR0
V66	13:46:27.166	-51:22:40.14	2456833.7152	17.55(08)	12.06	0.05	74	SR
V67	13:46:26.121	-51:22:23.76	2456822.5630	21.20(11)	12.29	0.04	74	SR
V68	13:46:26.190	-51:22:26.55	2456844.4857	32.95(27)	11.87	0.10	74	SR
V69	13:46:25.869	-51:22:16.18	–	–	12.26	0.05	74	L
V70	13:46:24.334	-51:22:47.14	–	–	11.57	0.07	63	L
V71	13:46:27.668	-51:22:35.25	–	–	11.66	0.09	74	L
V72	13:46:27.364	-51:22:16.22	–	–	11.64	0.14	74	L
V73	13:46:27.008	-51:22:29.88	–	–	11.51	0.52	74	L

4.5.1 Known variables

This globular cluster has 58 known variable stars listed in the Catalogue of Variable Stars in Galactic Globular Clusters (Clement et al. 2001) of which 52 are RR Lyrae stars. There are only 11 previously known variable stars in the field of view of our reference image (V37, V39, V40, V41, V43, V46, V50, V55, V56, V57, V58). All of them are RR Lyrae discovered by Zorotovic et al. (2010) using DIA on imaging data from a one-week observing run.

The celestial coordinates given in Tab. 1 of Zorotovic et al. (2010) do not match the positions of the known variable stars in the field of our images. We therefore used the finding chart given in their Fig. 1 to do a visual matching of the variables. As pointed out in the Catalogue of Variable Stars in Galactic Globular Clusters (Clement et al. 2001), there is a difference in the position of the variables studied by Zorotovic et al. (2010) with respect to the position of the variables in Samus et al. (2009b) which is ∼6 arcseconds in declination and $\lesssim$1 arcsecond in right ascension. This difference is corroborated by the position of the variables in our reference image. Celestial coordinates of the positions we used are given in Tab. 4.4.

Our extended observational baseline has allowed us to greatly improve the periods of the variables discovered by Zorotovic et al. (2010). Our period estimates are listed in Tab. 4.4 and have typical errors of 0.00002 - 0.00010 d. We confirm the variable star classifications made by Zorotovic et al. (2010).

Note that V41 is a strong blend with a brighter star that is only just resolved in our high-resolution reference image.

4.5.2 New variables

In this globular cluster we found 11 previously unknown variables where 5 are long-period irregular variables, 3 are semi-regular variables, 2 are RR Lyrae, and 1 is a SX Phoenicis.

V63: The star has a median magnitude of I ~18.52 mag and it is in the blue straggler region. Its amplitude is $A_{i'+z'}$ ~0.49 mag and it has a period of P=0.0486320 d. The star is clearly a SX Phoenicis. The variation of this star was not detected using the RMS or S_B statistic, although it is very clear in the difference images.

V64: This star is an RR Lyrae pulsating in the first overtone (RR1) with a period of 0.369783 d and an amplitude of 0.41 mag. In Fig. 4.13, notice that V64 is **very close** to a bright star (6.808 pixels or 0.613 arcsec). This could be the reason why this variable was not discovered before and makes a good example of the benefits of using the EMCCD cameras and the shift-and-add technique along with DIA.

V65: This star is another RR Lyrae which is pulsating in the fundamental mode (RR0) with a period of 0.619491 d and an amplitude of ~0.36 mag.

V66-V68: These stars are semi-regular variables. As it is seen in Fig. 4.12, they are at the top of the red giant branch. They have amplitudes that range between 0.04 to 0.10 mag. They have periods between ~17 to 33 d. Ephemerides for these stars can be found in Tab. 4.4.

V69-V73: These five stars are also positioned at the top of the red giant branch with amplitudes of 0.05 to 0.52 mag. It was not possible to find periods for these stars in this work. Due to this, they were classified as long-period irregular variables.

In Fig. 4.15 the amplitude-period diagram for the RR Lyrae stars studied in this cluster is shown. The filled lines correspond to the Oosterhoff type I (OoI) and the dashed lines correspond to the Oosterhoff type II (OoII) models defined by Kunder et al. (2013). All RR0 variables (with exception of V65) fall on the model for OoII type while the RR1 stars scatter around both models. In this diagram the RR0 stars suggest an OoII type classification for NGC 5286 which is in agreement with the study done by Zorotovic et al. (2010) where they found that their research pointed to an OoII status as well.

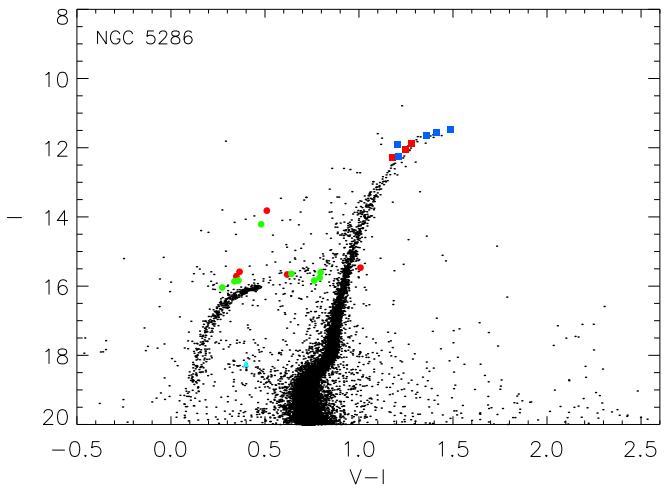

Figure 4.12: Colour magnitude diagram for the globular cluster NGC 5286 built with V and I magnitudes available in the ACS globular cluster survey extracted from HST images. The variable stars are plotted in colour following the convention adopted in Tab. 3.1.

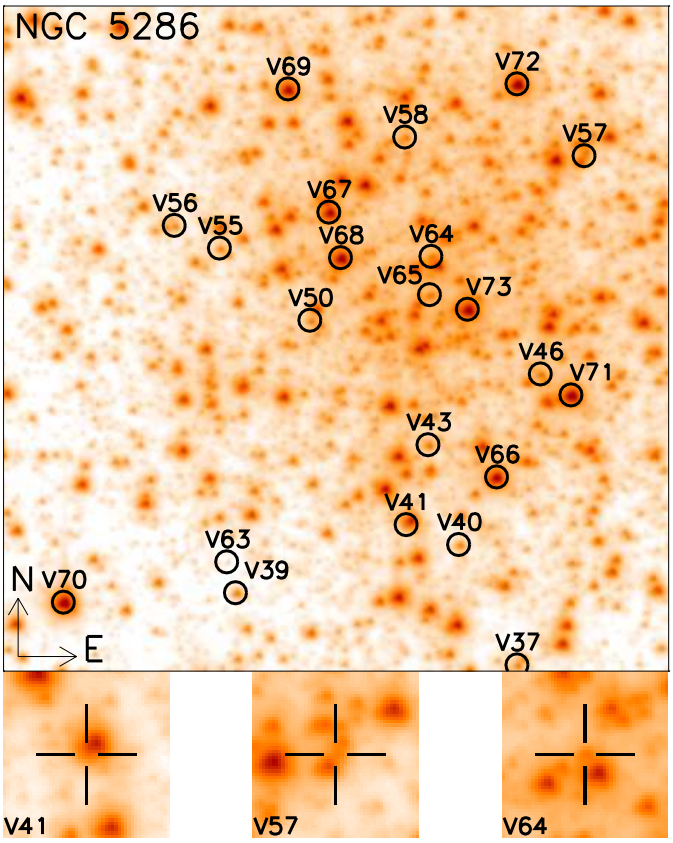

Figure 4.13: Finding chart for the globular cluster NGC 5286. The image used corresponds to the reference image constructed during the reduction. All known variables and new discoveries are labelled. Image size is $\sim 41 \times 41$ arcsec^2. The image stamps are of size $\sim 4.6 \times 4.6$ arcsec^2.

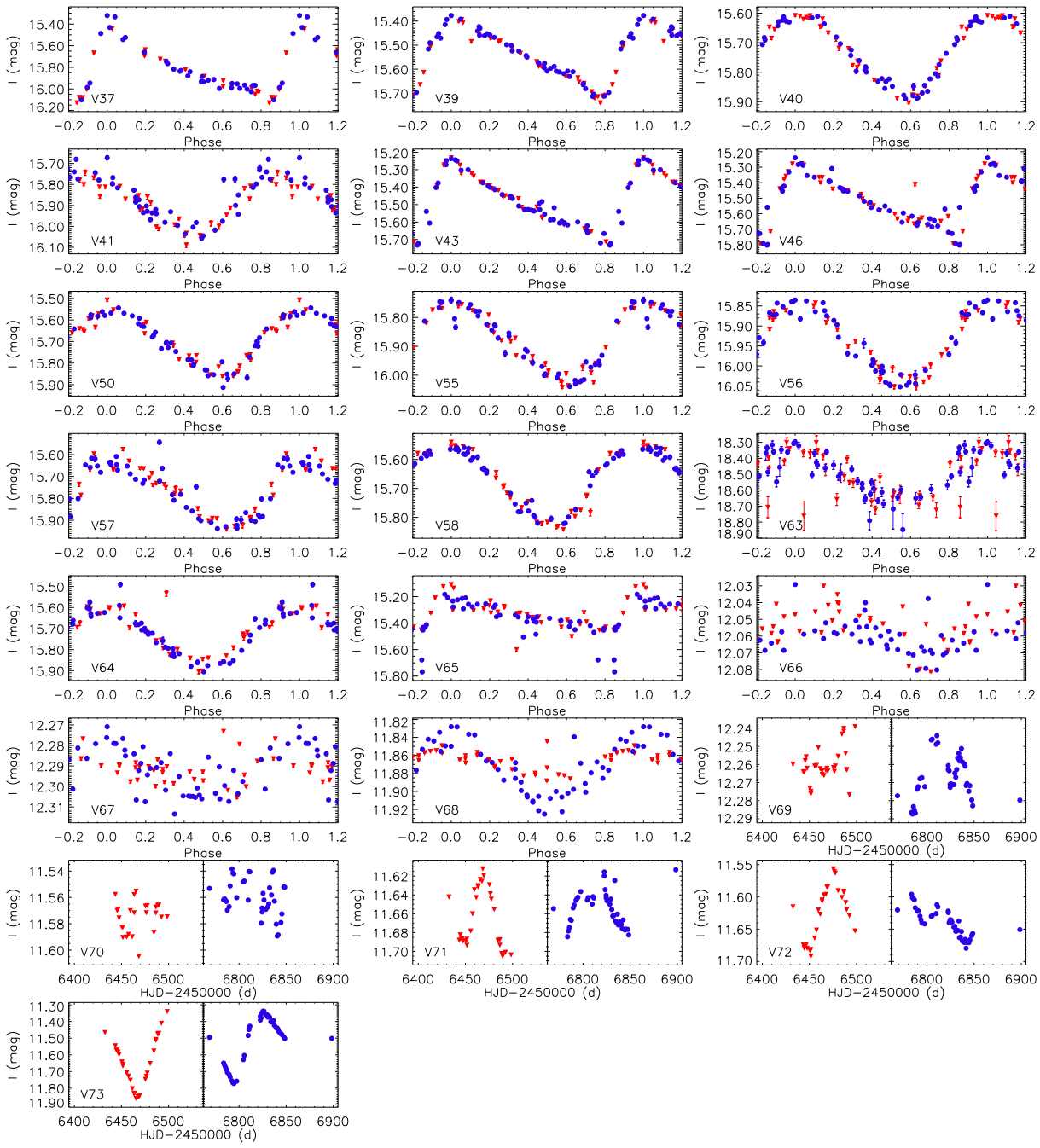

Figure 4.14: NGC 5286: Light curves of the known and new variables discovered in this globular cluster. Symbols are the same as in Fig. 4.6.

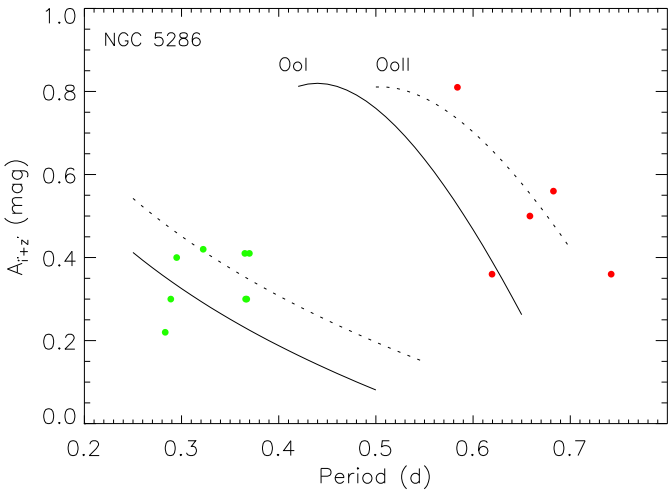

Figure 4.15: Amplitude-period diagram for the RR Lyrae stars in the globular cluster NGC 5286.

4.6 NGC 6093 / C1614-228 / M 80

This globular cluster was catalogued by Charles Messier in 1781[6]. This cluster is in the constellation of Scorpius at 10.0 kpc from the Sun and 3.8 kpc from the Galactic centre. Its has a metallicity of [Fe/H]=-1.75 dex, a distance modulus of $(m - M)_V$=15.56 mag and the position of its horizontal branch is at V=16.10 mag.

Table 4.5: NGC 6093: Ephemerides and main characteristics of the variable stars in the field of this globular cluster. Columns are the same as in Tab. 4.2.

Var id	RA	Dec	Epoch	P	I_{median}	$A_{i'+z'}$	N	Type
	J2000	J2000	HJD	d	mag	mag		
V10	16:17:01.163	-22:58:34.57	2456805.5870	0.614154(92)	14.25	0.29	52	RR0
V17	16:17:02.864	-22:58:32.55	2456831.5535	0.415081(42)	15.31	0.31	62	RR1
V19	16:17:02.107	-22:58:29.10	2456844.5144	0.596064(87)	15.28	0.54	62	RR0
V20	16:17:03.263	-22:58:37.49	2456831.5535	0.745207(136)	15.31	0.46	62	RR0
V34	16:17:02.820	-22:58:33.80	–	–	16.44	0.36	62	CV(Nova)
V35	16:17:03.313	-22:58:33.15	–	–	11.40	0.09	62	L
V36	16:17:03.145	-22:58:41.92	–	–	11.50	0.12	62	L
V37	16:17:02.320	-22:58:30.48	–	–	11.51	0.09	62	L
V38	16:17:03.263	-22:58:34.96	–	–	11.70	0.04	62	L
V39	16:17:02.201	-22:58:34.49	–	–	11.75	0.07	62	L
V40	16:17:03.042	-22:58:25.72	–	–	12.36	0.13	62	L

A total of 1220 light curves were extracted in the field covered by the reference image for the globular cluster NGC 6093. Most of the stars have 58 epochs in their light curves and variable stars studied in this work are plotted with colour in the RMS and S_B diagrams shown in Fig. 4.16.

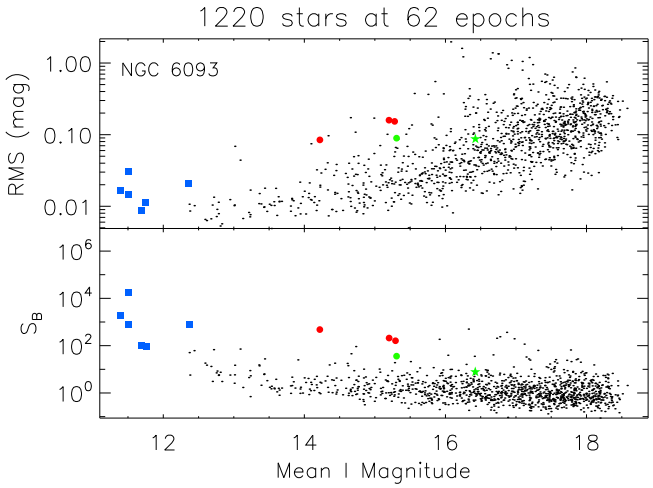

Figure 4.16: Root mean square (RMS) magnitude deviation (top) and S_B statistic (bottom) versus the mean I magnitude for the 1220 stars detected in the field of view of the reference image for NGC 6093. Coloured points follow the convention adopted in Tab. 3.1 to identify the types of variables found in the field of this globular cluster.

[6]http://messier.seds.org/m/m080.html

4.6.1 Known variables

This globular cluster has 34 known variable sources in the Catalogue of Variable Stars in Galactic Globular Clusters (Clement et al. 2001). Only 7 are in the field of view covered by these observations. There is no visual detection of V11 in our images (discovered by Shara et al. 2005, and classified as a possible U Geminorum-type cataclysmic variable). This is to be expected since it has a U mean magnitude of 19.5 mag. The star V33 was discovered by Dieball et al. (2010) in an ultraviolet survey using the Hubble Space Telescope. They reported a UV magnitude for this target of about 19.8 mag. Again it was not possible to obtain a light curve for this faint target.

For the remaining variable stars in the field of view, three of them are RR0 (V10, V19 and V20), one is a RR1 (V17), and V34 is a Nova. Light curves for these stars are presented in Fig. 4.19. We have improved on the period estimates published by Kopacki (2013) for the four RR Lyrae variables since we observed them using a time baseline of over 1 year, whereas Kopacki (2013) analysed observations spanning only one week.

V34: This is the nova discovered by Arthur von Auwers at Koenigsberg Observatory on May 21, 1860 (Luther 1860). As pointed out in the Catalogue of Variable Stars in Galactic Globular Clusters (Clement et al. 2001), an account of its discovery was given by Sawyer (1938) in which a maximum visual apparent magnitude of 6.8 mag was reported using the data taken by von Auwers and Luther. Another review can also be found in Wehlau et al. (1990). However, no observations of the nova in outburst have been made until the present study. During our 2013 observing campaign, we caught an outburst of amplitude ~0.36 mag starting at around HJD~2456500 d which lasted for ~50 days. In our 2014 data the nova continued at its baseline magnitude at ~16.44 mag.

Dieball et al. (2010) in their ultraviolet survey assigned the label CX01 to an X-ray source that was found to be associated with the position of the nova at the coordinates RA(J2000)=16:17:02.817 and DEC(J2000)=-22:58:33.92. These coordinates match with the position of the outburst found in this work and details are given in Tab. 4.5.

The position in the colour magnitude diagram shown in Fig. 4.17 suggests that this system is a cluster member. It is located at the bottom part of the red giant branch. Its position is plotted with a green five pointed star.

As the nova with its outburst has shown variability, we have assigned the label V34 to this object.

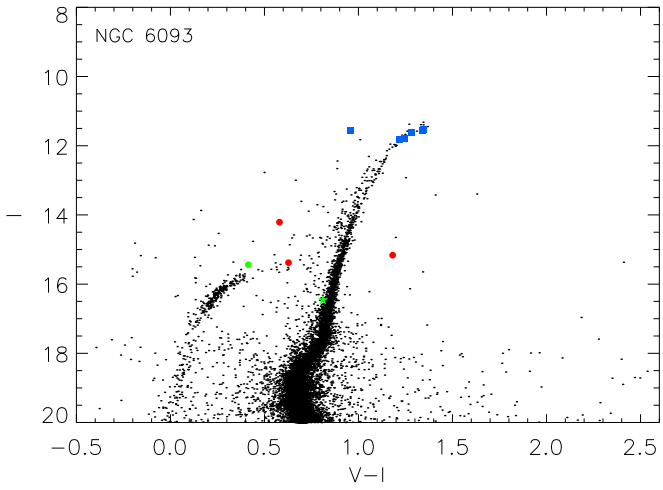

Figure 4.17: Colour magnitude diagram for the globular cluster NGC 6093 built with V and I magnitudes available in the ACS globular cluster survey extracted from HST images. The variable stars are plotted in colour following the convention adopted in Tab. 3.1.

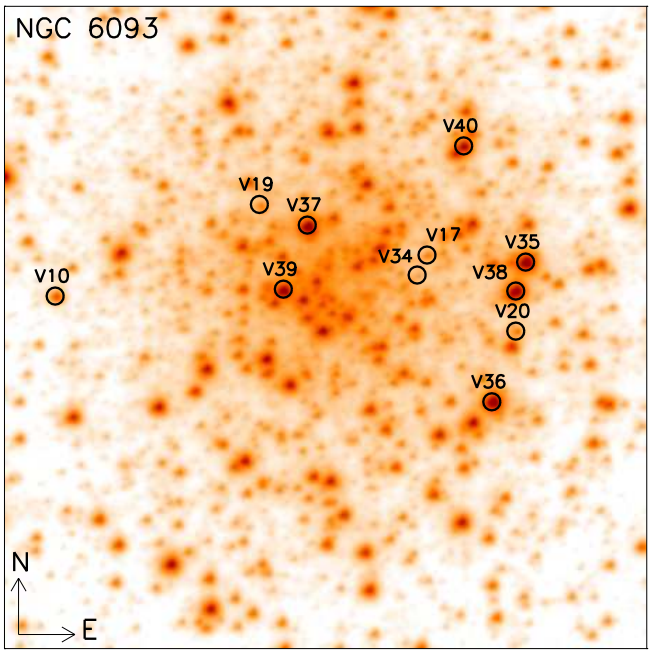

Figure 4.18: Finding chart for the globular cluster NGC 6093. The image used corresponds to the reference image constructed during the reduction. All known variables and new discoveries are labelled. Image size is $\sim 41 \times 41$ arcsec^2.

4.6.2 New variables

A total of 6 new variables were found in this work. All of them are long-period irregular variables.

V35-V40: These stars are long-period irregular variables. They are located at the top of the red giant branch (see Fig. 4.17). Their amplitudes go from ~0.04 to 0.13 mag. The star V40 is the one placed at the blue side of the red giant branch. We did not find any kind of regular periodicity in the variation of these stars.

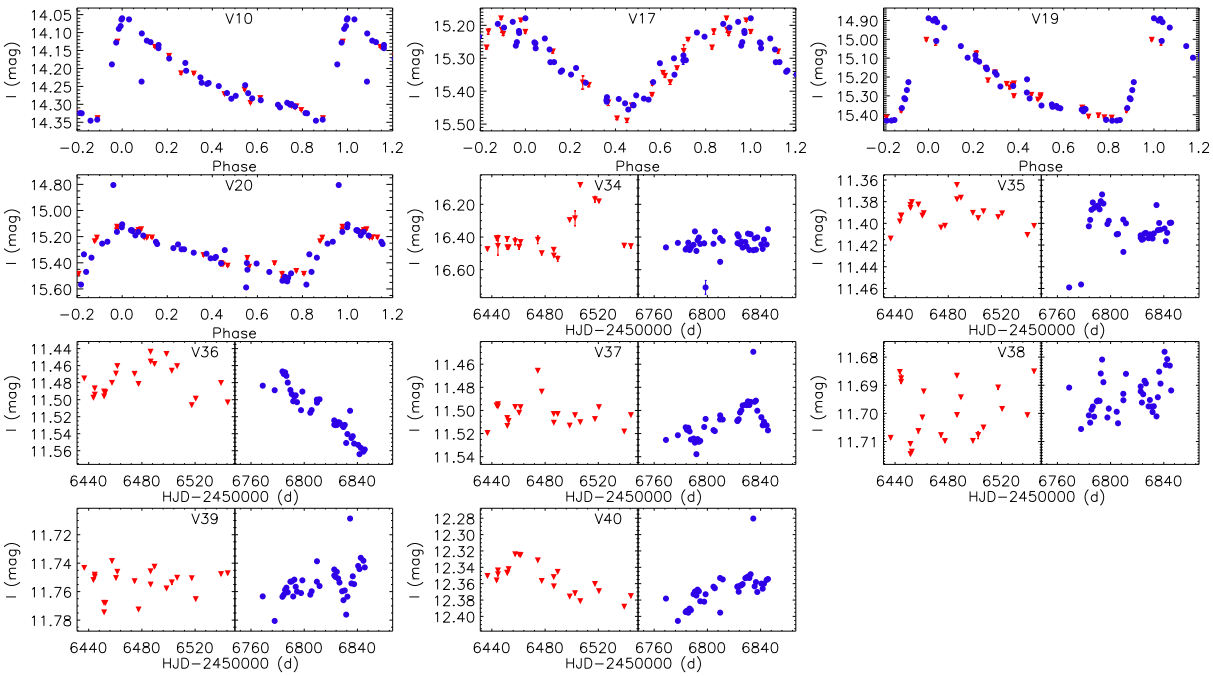

Figure 4.19: NGC 6093: Light curves of the known and new variables discovered in this globular cluster. Symbols are the same as in Fig. 4.6.

4.7 NGC 6121 / C1620-264 / M4

This globular cluster was catalogued by Philippe Loys de Chéseaux in 1746[7]. This cluster is in the constellation of Scorpius at a distance of 2.2 kpc from the Sun and 5.9 kpc from the Galactic centre. It has a metallicity of [Fe/H]=-1.16 dex and a distance modulus of $(m\text{-}M)_V$=12.82 mag. Its horizontal branch level is at V_{HB}=13.45 mag.

Table 4.6: NGC 6121: Ephemerides and main characteristics of one variable star in the field of this globular cluster. Columns are the same as in Tab. 4.2.

Var id	RA J2000	Dec J2000	Epoch HJD	P d	I_{median} mag	$A_{i'+z'}$ mag	N	Type
V21	16:23:35.903	-26:31:33.68	2456477.5041	0.472008(56)	12.55	0.92	64	RR0

This globular cluster has of the order of 100 known variables in the Catalogue of Variable Stars in Galactic Globular Clusters (Clement et al. 2001) and only three are in the field of view of the reference image; namely V21, V81 and V101. Furthermore, only V21 is bright enough to be detected. The light curve for this RR0 star is shown in Fig. 4.21. The known period P=0.4720 d produces a very well phased light curve and it is in agreement with the period P=0.472008 d found in the analysis of this star.

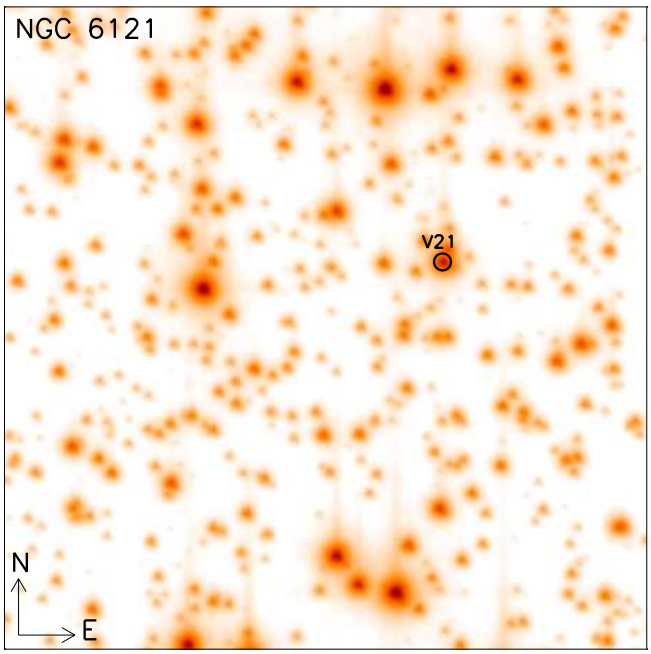

Figure 4.20: Finding chart for the globular cluster NGC 6121. The image used corresponds to the reference image constructed during the reduction. The only known variable in the field is labelled. Image size is $\sim 41 \times 41$ arcsec^2.

No new variable stars were found in the field covered by the reference image for this globular cluster.

[7] http://messier.seds.org/m/m004.html

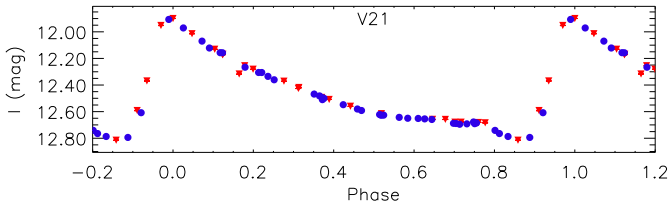

Figure 4.21: NGC 6121: Light curve of the variable V21 in this globular cluster. Symbols are the same as in Fig. 4.6.

4.8 NGC 6541 / C1804-437

This globular cluster was catalogued by N. Cacciatore in 1826[8]. It is in the constellation of Corona Australis at 7.5 kpc from the Sun and 2.1 kpc from the Galactic centre. The cluster has a metallicity of [Fe/H]=-1.81 dex, a distance modulus of $(m - M)_V$=14.82 mag and the level of the horizontal branch is at V_{HB}=15.35 mag.

Table 4.7: NGC 6541: Ephemerides and main characteristics of the variable stars in the field of this globular cluster. Columns are the same as in Tab. 4.2.

Var id	RA J2000	Dec J2000	Epoch HJD	P d	I_{median} mag	$A_{i'+z'}$ mag	N	Type
V14	18:08:01.670	-43:42:52.26	2456908.7354	0.064669(1)	16.38	0.27	43	SXPhe
V21	18:08:02.180	-43:42:52.91	2456782.8812	0.596000(76)	14.39	0.59	43	RR0
V22	18:08:03.743	-43:42:34.46	–	–	10.74	0.17	29	L

A total of 843 light curves were extracted in this globular cluster. Most of them have 42 epochs. RMS diagram and S_B statistic are shown in Fig. 4.22.

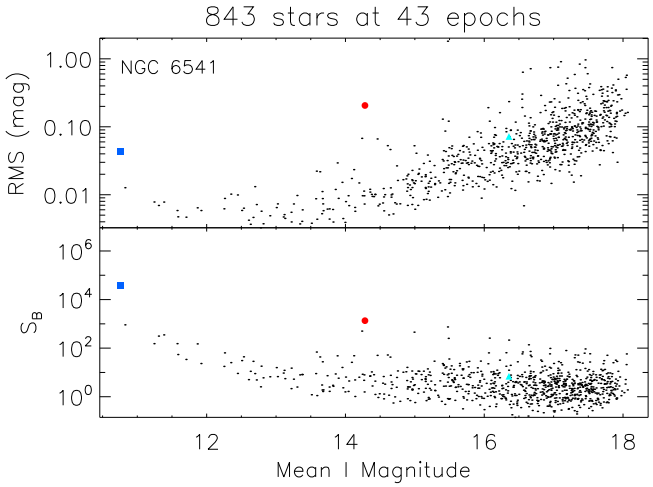

Figure 4.22: Root mean square (RMS) magnitude deviation (top) and S_B statistic (bottom) versus the mean I magnitude for the 843 stars detected in the field of view of the reference image for NGC 6541. Coloured points follow the convention adopted in Tab. 3.1 to identify the types of variables found in the field of this globular cluster.

4.8.1 Known variables

This globular cluster has 20 known variables. Four of them are in the field of view of our reference image: V12, V14, V15, and V17. Fiorentino et al. (2014) discovered and classified these stars as SX Phoenicis in their study carried out using observations with the HST. We were only able to recover V14 in our data around 2 arcseconds in declination from the reported position for this star in Fiorentino et al. (2014). We did not detect variability at the positions given for V12, V15 and V17 neither in their surrounding areas, more likely due to the fact that the stars are too faint to be detected in our reference image. A reference image with higher signal to noise ratio might be needed in future studies of this globular cluster and longer exposure times for each observation.

[8]http://spider.seds.org/spider/MWGC/n6541.html

V14: For this star we refined the period estimate to 0.064669 d from the previously listed value of 0.0649 d in Fiorentino et al. (2014).

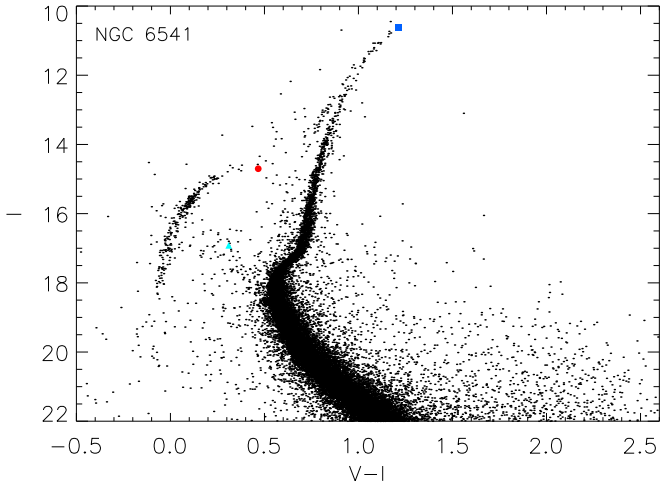

Figure 4.23: Colour magnitude diagram for the globular cluster NGC 6541 built with V and I magnitudes available in the ACS globular cluster survey extracted from HST images. The variable stars are plotted in colour following the convention adopted in Tab. 3.1.

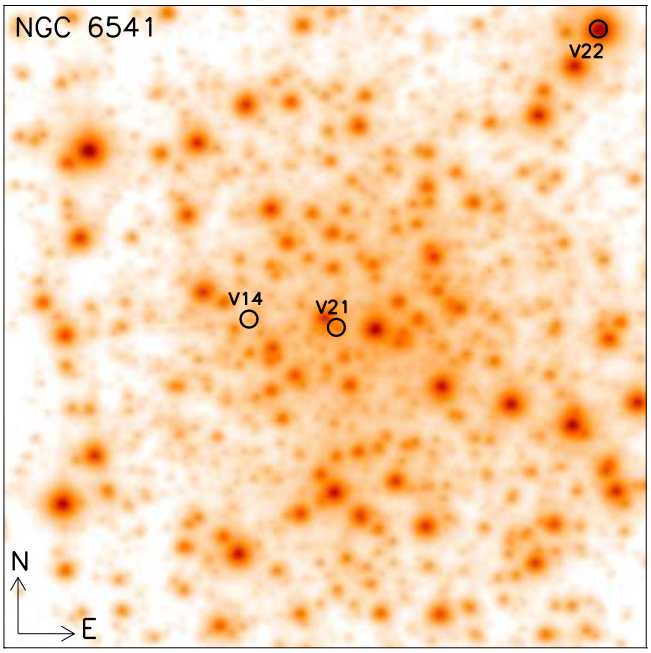

Figure 4.24: Finding chart for the globular cluster NGC 6541. The image used corresponds to the reference image constructed during the reduction. All known variables and new discoveries are labelled. Image size is $\sim 41 \times 41$ arcsec^2.

4.8.2 New variables

A total of two new variable stars were found in this globular cluster: one RR Lyrae and one long-period irregular variable.

V21: This star is a RR Lyrae pulsating in the fundamental mode. In the colour-magnitude diagram (Fig. 4.23) for this cluster it falls exactly in the instability strip of the horizontal branch. It is next to a brighter star

(∼1.039 arcsec) and this may be why it was not discovered before.

V22: This star is at the top of the red giant branch in the colour-magnitude diagram of the globular cluster (Fig. 4.23). From the light curve obtained it was possible to measure an amplitude of $A_{i'+z'}$=0.17 mag. We classified this star as a long-period irregular variable as it was not possible to find a period.

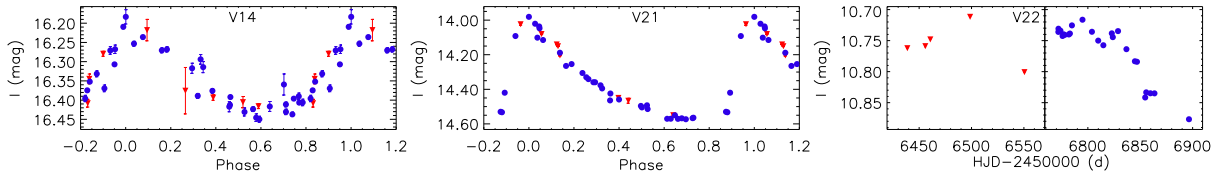

Figure 4.25: NGC 6541: Light curves of the known and new variables discovered in this globular cluster. Symbols are the same as in Fig. 4.6.

4.9 NGC 6656 / C1833-239 / M 22

This globular cluster was catalogued by Abraham Ihle in 1665[9]. It is in the constellation of Sagittarius at 3.2 kpc from the Sun and 4.9 kpc from the Galactic centre. The cluster has a metallicity of [Fe/H]=-1.70 dex, a distance modulus of (m-M)$_V$=13.60 mag and the horizontal branch level is at V$_{HB}$=14.15 mag.

Table 4.8: NGC 6656: Ephemerides and main characteristics of the variable stars in the field of this globular cluster. Columns are the same as in Tab. 4.2.

Var id	RA	Dec	Epoch	P	I_{median}	$A_{i'+z'}$	N	Type
	J2000	J2000	HJD	d	mag	mag		
V35	18:36:24.051	-23:54:29.53	2456472.8818	141(5)	9.43	0.13	19	SR
PK-06	18:36:25.228	-23:54:37.44	2456789.8239	0.140851(4)	17.08	0.65	51	EW
CV1	18:36:24.696	-23:54:35.60	2456877.6355	–	17.87	3.28	51	CV(DN)

4.9.1 Known variables

There are of the order of 100 variable sources known for this globular cluster. Only 4 of these are inside the field of view of the reference image (V35, PK-06, PK-08 and CV1). PK-08 is too faint for us to extract a light curve.

V35: This star is the brightest star in our field of view and it is classified as a semi-regular variable. The star is at the top of the red giant branch in the colour-magnitude diagram shown in Fig. 4.28. Sahay et al. (2014) found a period of ∼56 d. However, we found a period of 141 ± 5 d.

PK-06: This star is classified as an EW eclipsing variable. It was discovered by Pietrukowicz & Kaluzny (2003) and it is their star M22_06. They found a period P=0.239431 d. However, it does not produce a good phased light curve in our data. In the analysis of this variable we found a period of P=0.140851 d which produces a better phased light curve (See Fig. 4.27). However, our phased light curve is still not as clear as that of Pietrukowicz & Kaluzny (2003).

CV1: The variability of this star was first detected by Sahu et al. (2001a) as a suspected microlensing event, but it was not until Anderson et al. (2003) that it was classified as a dwarf nova outburst. The analysis of our light curve for this source shows that it undergoes an outburst of ∼3 mag around HJD ∼2456877 which decays over ∼20d. It is in agreement with previous studies. Anderson et al. (2003) found that an earlier outburst lasted ∼20-26d with an amplitude of ∼3 mag peaking at I ≈15 mag. Alonso-Garcia et al. (2015) also observed the 2014 outburst seen in our data and reported a Ks-band brightening of 1 mag. In Fig. 4.27, we have plotted the light curve for this star.

[9]http://messier.seds.org/m/m022.html

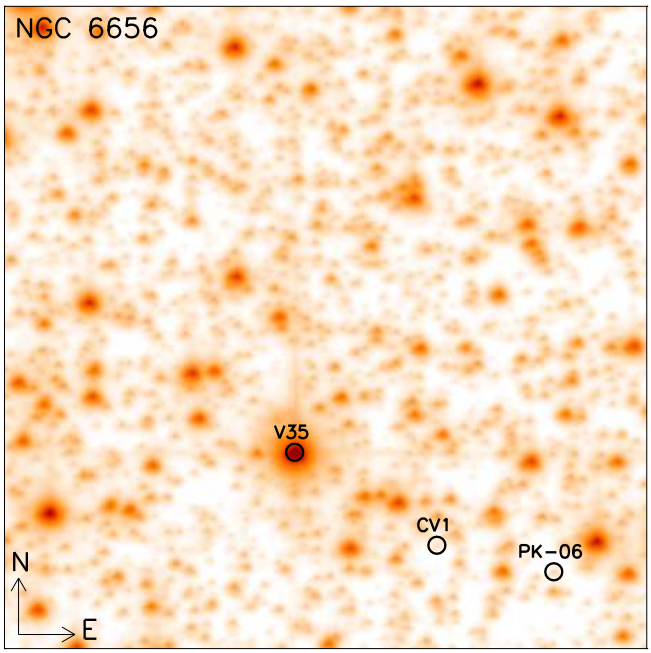

Figure 4.26: Finding chart for the globular cluster NGC 6656. The image used corresponds to the reference image constructed during the reduction. All known variables and new discoveries are labelled. Image size is $\sim 41 \times 41$ arcsec^2.

Our search for new variable sources in this cluster did not yield any.

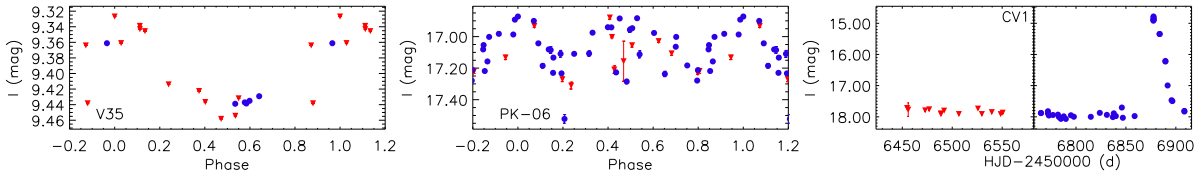

Figure 4.27: NGC 6656: Light curves of the known variables found in this globular cluster. Symbols are the same as in Fig. 4.6.

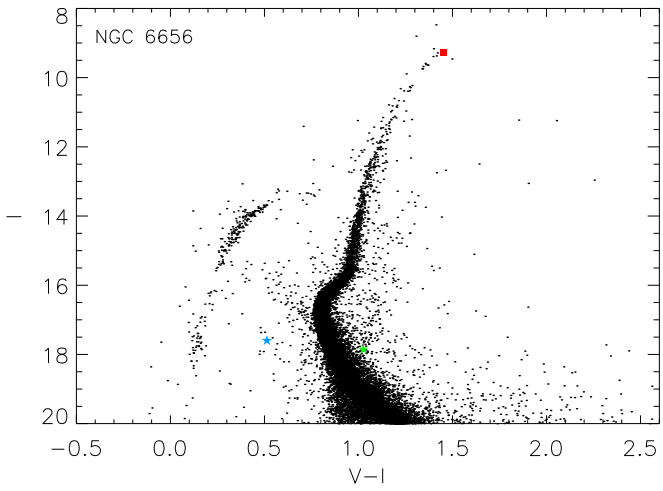

Figure 4.28: Colour magnitude diagram for the globular cluster NGC 6656 built with V and I magnitudes available in the ACS globular cluster survey extracted from HST images. The variable stars are plotted in colour following the convention adopted in Tab. 3.1.

4.10 NGC 6681 / C1840-323 / M70

This globular cluster was catalogued by Charles Messier in 1780[10]. The globular cluster is in the constellation of Sagittarius at 9.0 kpc from the Sun and 2.2 kpc from the Galactic centre. It has a metallicity of [Fe/H]=-1.62 dex, a distance modulus of $(m\text{-}M)_V$=14.99 mag and the horizontal branch level is at V_{HB}=15.55 mag.

Table 4.9: NGC 6681: Ephemerides and main characteristics of one variable star in the field of this globular cluster. Columns are the same as in Tab. 4.2.

Var id	RA J2000	Dec J2000	Epoch HJD	P d	I_{median} mag	$A_{i'+z'}$ mag	N	Type
V6	18:43:12.015	-32:17:29.70	2456814.8334	0.341644(25)	15.09	0.23	50	RR1

There are a total of 1315 light curves available for this cluster to be analysed. Most of them have 50 epochs. The RMS and S_B diagrams can be found in Fig. 4.29. Variable stars studied in this work are plotted in colour.

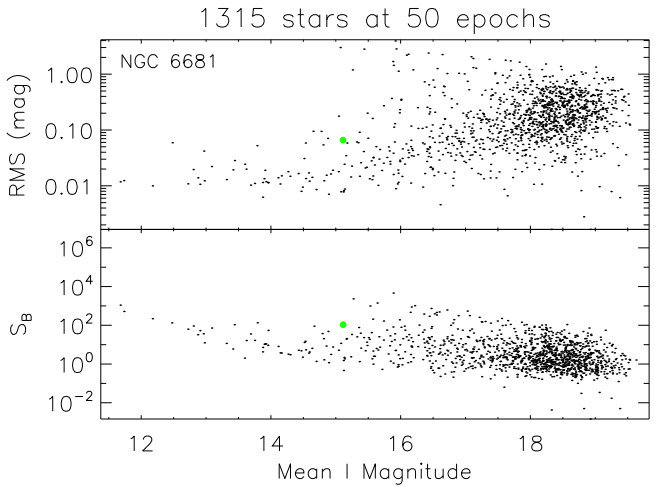

Figure 4.29: Root mean square (RMS) magnitude deviation (top) and S_B statistic (bottom) versus the mean I magnitude for the 1315 stars detected in the field of view of the reference image for NGC 6681. The coloured point follows the convention adopted in Tab. 3.1 to identify the types of variables found in the field of this globular cluster.

4.10.1 Known variables

This globular cluster has only 5 known variables, none of which are in the field of view of our reference image.

Kadla et al. (1996) reported several RR Lyrae candidates based on the position of the stars in the instability strip of the horizontal branch but none of them matched the position of the only variable star found in the field of view covered by our reference image which is the new variable V6 explained in the next section.

[10]http://messier.seds.org/m/m070.html

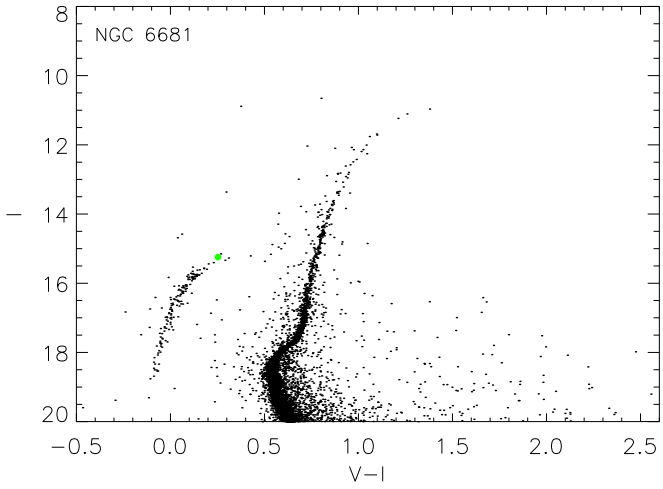

Figure 4.30: Colour magnitude diagram for the globular cluster NGC 6681 built with V and I magnitudes available in the ACS globular cluster survey extracted from HST images. One variable star is plotted in colour following the convention adopted in Tab. 3.1.

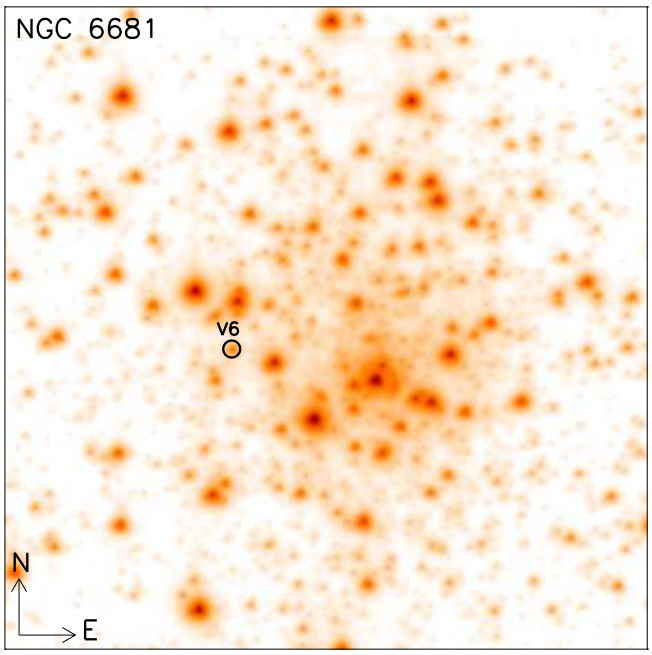

Figure 4.31: Finding chart for the globular cluster NGC 6681. The image used corresponds to the reference image constructed during the reduction. All known variables and new discoveries are labelled. Image size is $\sim 41 \times 41$ arcsec^2.

4.10.2 New variables

One new RR Lyrae was discovered in this globular cluster.

V6: This star has an amplitude of 0.23 mag and a period of P=0.341644d. The star is placed just at the instability strip of the horizontal branch (see Fig. 4.30). It is clearly a previously unknown RR Lyrae of type RR1. The light curve for this variable is shown in Fig. 4.32.

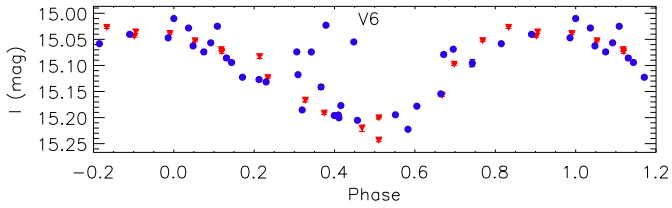

Figure 4.32: NGC 6681: Light curve of the new variable discovered in this globular cluster. Symbols are the same as in Fig. 4.6.

4.11 NGC 6723 / C1856-367

This globular cluster was catalogued by James Dunlop in 1826[11]. It is in the constellation of Sagittarius at a distance of 8.7 kpc from the Sun and 2.6 kpc from the Galactic centre. It has a metallicity of [Fe/H]=-1.10 dex, a distance modulus of $(m\text{-}M)_V$=14.84 mag and the horizontal branch level is at V_{HB}=15.48 mag.

Table 4.10: NGC 6723: Ephemerides and main characteristics of the variable stars in the field of this globular cluster. Columns are the same as in Tab. 4.2.

Var id	RA J2000	Dec J2000	Epoch HJD	P d	I_{median} mag	$A_{i'+z'}$ mag	N	Type
V8	18:59:34.678	-36:37:42.33	2456908.5573	0.480278(49)	15.08	0.71	16	RR0
V34	18:59:33.189	-36:37:58.04	2456435.8962	0.531414(60)	14.85	0.84	56	RR0
V35	18:59:32.963	-36:38:01.46	2456524.8178	0.606451(78)	14.80	0.32	56	RR0
V44	18:59:32.347	-36:37:51.96	2456454.9399	0.440075(41)	15.08	0.93	56	RR0

In Fig. 4.33, the RMS and S_B statistic diagrams for 1258 stars in the globular cluster NGC 6723 are shown. Most of the light curves have 56 epochs. Variable stars analysed in this work are plotted in colour following the convention adopted in Tab. 3.1.

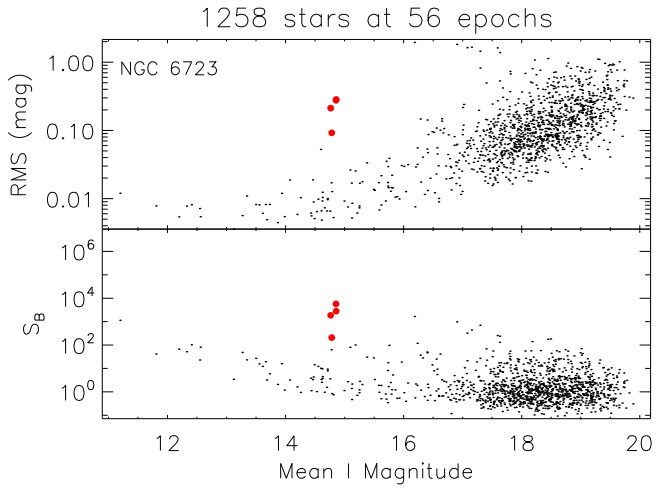

Figure 4.33: Root mean square (RMS) magnitude deviation (top) and S_B statistic (bottom) versus the mean I magnitude for the 1258 stars detected in the field of view of the reference image for NGC 6723. Coloured points follow the convention adopted in Tab. 3.1 to identify the types of variables found in the field of this globular cluster.

4.11.1 Known variables

This globular cluster has 47 known variables stars in the Catalogue of Variable Stars in Galactic Globular Clusters (Clement et al. 2001). 43 are classified as RR Lyrae, two as semi-regular variables, one as a T Tauri star that does not seem to be a cluster member and one as a SX Phoenicis. Four of the known RR Lyrae are in the field of our reference frame (V8, V34, V35 and V44). They are RR0 pulsating stars. The star V8 was discovered by Bailey (1902) and although it is close to the reference image border, it was possible to obtain 16 data points. V34, V35 and V44 were discovered by Lee et al. (2014).

In the colour magnitude diagram for this globular cluster (see Fig. 4.35) these variables are placed just in the instability strip of the horizontal branch. Light curves for these variables are shown in Fig. 4.37.

[11] http://spider.seds.org/spider/MWGC/n6723.html

The four RR Lyrae in the field of our images are plotted in the period-amplitude diagram shown in Fig. 4.34. It is possible to see that even though V34 and V35 have the Blazhko effect, all of them are following the model of fundamental mode pulsating stars for Oosterhoff type I which is consistent with the Oosterhoff classification for this cluster (see Lee et al. 2014; Kovacs et al. 1986, and references therein).

The periods that we derive for the 4 RR Lyrae stars are perfectly consistent with those derived by Lee et al. (2014) using a 10 year baseline. Furthermore, the Blazhko effect in V34 and V35 is also evident in our light curves.

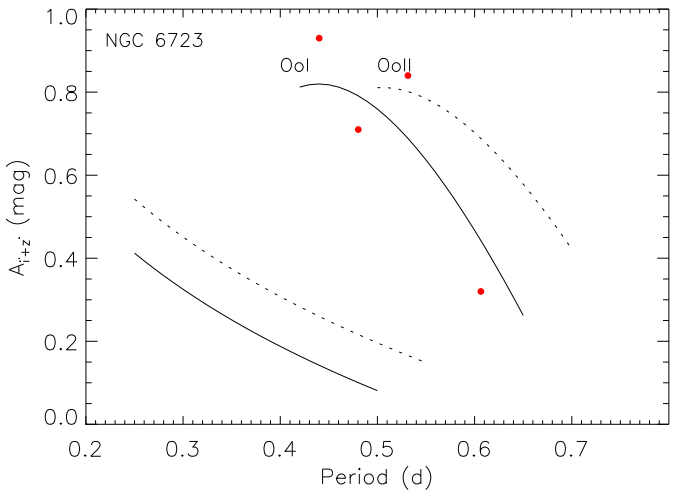

Figure 4.34: Period-amplitude diagram for the globular cluster NGC 6723. The previously known RR Lyrae are plotted.

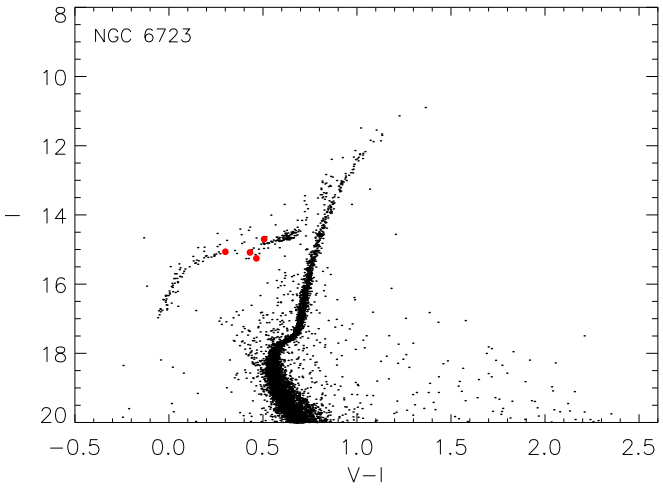

Figure 4.35: Colour magnitude diagram for the globular cluster NGC 6723 built with V and I magnitudes available in the ACS globular cluster survey extracted from HST images. The variable stars are plotted in colour following the convention adopted in Tab. 3.1.

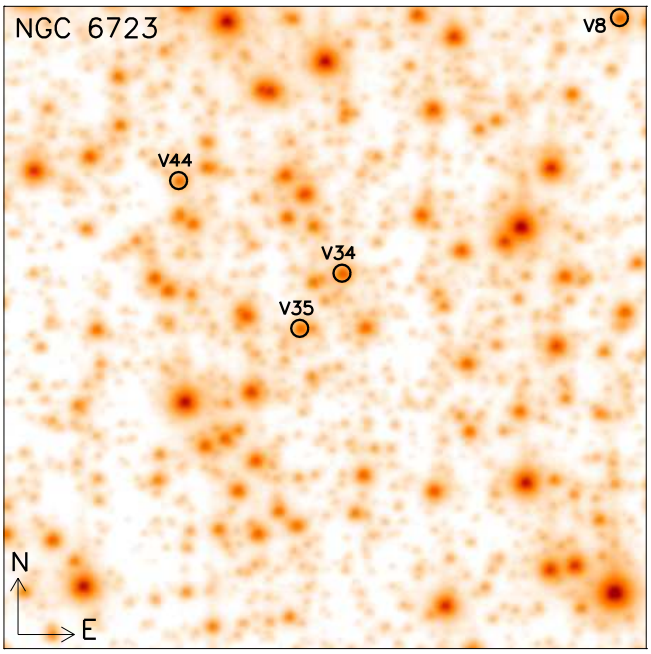

Figure 4.36: Finding chart for the globular cluster NGC 6723. The image used corresponds to the reference image constructed during the reduction. All known variables and new discoveries are labelled. Image size is $\sim 41 \times 41$ arcsec^2.

No new variable stars were found in the field covered by the reference image for this globular cluster.

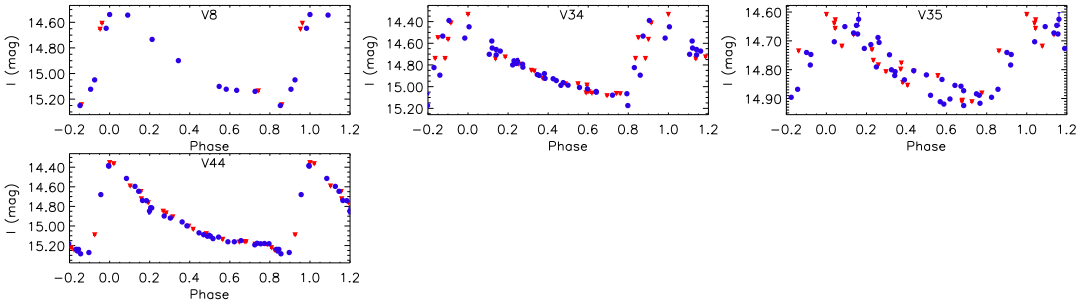

Figure 4.37: NGC 6723: Light curves of the known variables in this globular cluster. Symbols are the same as in Fig. 4.6.

4.12 NGC 6752 / C1906-600 / C93

This globular cluster was catalogued by James Dunlop in 1826[12]. It is in the constellation of Pavo with a distance of 4.0 kpc from the Sun and 5.2 kpc from the Galactic centre. It has a metallicity of [Fe/H]=-1.54 dex, a distance modulus of (m-M)$_V$=13.13 mag and the level of its horizontal branch is at V$_{HB}$=13.70 mag.

Table 4.11: NGC 6752: Ephemerides and main characteristics of one variable star in the field of this globular cluster. Columns are the same as in Tab. 4.2.

Var id	RA J2000	Dec J2000	Epoch HJD	P d	I_{median} mag	$A_{i'+z'}$ mag	N	Type
V26	19:10:51.494	-59:58:56.67	–	–	–	–	78	CV(DN)

4.12.1 Known variables

There are 32 known variable sources in this globular cluster which are listed in the Catalogue of Variable Stars in Galactic Globular Clusters (Clement et al. 2001). Six of them are in the field of view of our reference image. Three are millisecond pulsars (PSRB, PSRD and PSRE) discovered by D'Amico et al. (2001) and D'Amico et al. (2002). We could not find an optical counterpart in our reference image. Three more are Dwarf Novae (V25, V26, V27) discovered by Thomson et al. (2012) of which V26 is the only object in which we could detect variability.

V26: This star is classified as a Dwarf Nova. A finding chart for V26 is already available in Thomson et al. (2012). It was not possible to detect this star in the reference image in its quiescent state. However, it was possible to clearly detect one outburst in the difference images. Due to this, in Fig. 4.38 the difference fluxes measured for this star are plotted against Heliocentric Julian Day. It is possible to see that in the 2013 campaign the star was in its quiescent state. In 2014 observing season, the outburst started around HJD 2456840 with a maximum at HJD ~2456858.8532 and lasted ~80 d.

We did not find any evidence in our data for new variable stars in this globular cluster.

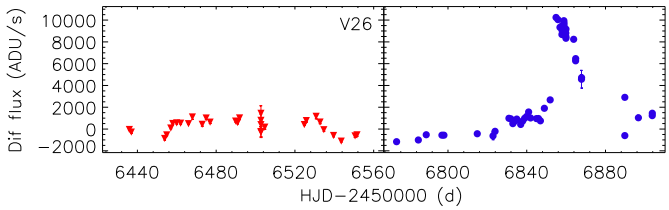

Figure 4.38: NGC 6752: Light curve of the variable V26 in this globular cluster. Symbols are the same as in Fig. 4.6. We plot the quantity $f_{\rm diff}(t)/p(t)$ since a reference flux is not available.

[12]http://spider.seds.org/spider/MWGC/n6752.html

Chapter 5

Discussions and Conclusions

During this research we explored a wide and diverse number of topics. In the introduction, we supplied the basic knowledge familiarization with the different topics covered in this thesis. We discussed the benefits obtained when astronomy moved to technologies such as CCDs. We commented about the constraints that an astronomer has to deal with when observing using ground-based telescopes such as blurring in the images due to atmospheric turbulence and we pointed out possible ways to overcome this effect by using space telescopes, adaptive optics, new cameras such as EMCCDs and strategies for co-adding images like the shift-and-add technique.

We talked about the challenges to overcome when observing highly crowded fields such as the Milky Way center and globular clusters. For globular clusters, these crowded fields will have stars at different evolutionary stages and different magnitudes. For observations with conventional CCDs it is very difficult (if not impossible) to register all of the incoming fluxes without saturating the brightest stars and without giving enough signal-to-noise ratio for the faintest stars. Saturated pixels of the brightest stars can affect the subtraction of the fluxes of their neighbor stars (e. g. Skottfelt et al. 2013). A proper subtraction of the fluxes among blended stars might also not be possible, and if one of the blended stars is a variable, the variability information could be lost entirely. These are some of the reasons why EMCCDs have become so useful for astronomy. We saw that by using these devices, with their ability to take frames at 10 Hz, it is possible to define exposure times for the final science images to obtain enough signal-to-noise ratio for the faintest stars without worrying about saturating the brightest. Additionally, due to the high frame rates, it was possible to mitigate the effect caused by the turbulence in the atmosphere which causes the blurring of the images.

We briefly explored the color-magnitude diagram for globular clusters, from the blue stragglers zone with main sequence stars that suffered collisions and increased their masses after their formation and from the main sequence where stars are burning hydrogen in the core and moving to the turn-off point when their hydrogen is exhausted.

Once this occurs, stars evolve to the red giant branch with a helium core and a hydrogen burning shell and they start the fusion of helium with the helium-flash and evolve to the horizontal branch perhaps to the blue or the red horizontal branch or even the instability strip and when the helium is exhausted in their core they will occupy stage in the asymptotic giant branch with a carbon-oxygen core plus a helium shell and more externally a hydrogen shell. At this stage, the star will produce stellar winds and lose their mass to finally end up as a white dwarf surrounded by a planetary nebula, ending parallel to and fainter than the main sequence.

As part of the different evolutionary stages found in the color-magnitude diagram, we pointed out the presence and vast diversity of variable stars that can be found in globular clusters and that they occupy specific zones in the CMD, and the importance of studying these stars.

5.1 The DanDIA pipeline

The DanDIA pipeline is based on difference image analysis, which is a powerful tool for performing image reduction and photometry extraction especially in crowded fields. We have tested it in several previous studies of globular clusters using conventional CCDs (see e. g. Figuera Jaimes et al. 2013; Kains et al. 2012; Bramich et al. 2011; Figuera Jaimes et al. 2011) and it has been widely used in large programmes such as those carried out by microlensing teams in the search for extrasolar planets, like MINDSTEp and RoboNet, to do reductions of massive amounts of astronomical images (see e. g. Ryu et al. 2018; Ciceri et al. 2016; Southworth et al. 2015; Street et al. 2014). The entire reduction procedure is done in eight steps which we briefly describe in continuation as a quick-guide and feedback for future users and developers. However detailed instructions can be found directly in the user manual:

Preprocess: In this step, all of the images to be reduced are verified to be sure they have the right format, in this case FITS files, and that the headers in the images contain the necessary information to be used during the reductions such as type of images used, the filter, date of observation, universal time, exposure time, right ascension, and declination. In Table 5.1, we summarize the correct format for these input parameters. Images are also corrected by calibrations frames (bias, dark, flats) if the user enables these options. The code also calculates, from the date and the hour of observation, the Julian date and does the respective heliocentric correction for each of the images. After that, images are grouped into bias, dark, flat, and science images for each filter. Finally, the code creates trend-log files with relevant information related to each of the images such as sky values, exposure times, FWHM, ellipticity, and number of stars detected.

Table 5.1: Fields that are needed in the headers of FITS files to be used by the DanDIA pipeline to be considered during the reduction procedure.

Field	Format	Comments
TARGET	‘object’; ‘bias’; ‘dark’; ‘flat’	String between quotation marks
FILTER	‘V’; ‘R’; ‘I’, ‘u’, ...	String between quotation marks
DATE-OBS	‘YYYY-MM-DD’	String between quotation marks
UT	‘HH:MM:SS.SSS’ or hours	String in HH:MM:SS or float in hours
EXPTIME	‘300’; ‘60’; ‘180’	String between quotation marks
RA	‘HH:MM:SS.SSS’	String between quotation marks
DEC	‘DD:MM:SS.SSS’	String between quotation marks

Cosmic: The cosmic ray correction applied by DanDIA to the images is based on the Laplacian Edge Detection method given in van Dokkum (2001). This method convolves each image with the kernel given in Equation 5.1

$$\nabla^2 f = \frac{1}{4}\begin{pmatrix} 0 & -1 & 0 \\ -1 & 4 & -1 \\ 0 & -1 & 0 \end{pmatrix}. \tag{5.1}$$

The kernel amplifies sharp features and smooth features are deamplified. They allowing cosmic ray events to be detected and removed. From our previous experience, in under-sampled or crowded fields, occasionally this method could detect a star as a cosmic ray, so the user must be careful to not be losing important stars in their research.

Reference: A reference frame is built using the sharpest images available during the observations. The user can define to use a single frame or to combine a group of them to produce a reference frame with a high exposure time and gain. The best images are selected based on best seeing calibrated frames which are registered (as commented below) and stacked to produce the reference frame. Sky background, PSF FWHM, and ellipticity are estimated for the resulting frame. The procedure finds stars in each of the images using the algorithm described in Stetson (1987).

Starfit: This step measures the positions and fluxes of the stars in the reference frame. The procedure is based on the algorithm defined in Diolaiti et al. (2000b). To do so, PSF models are created to represent the stars. These PSF models can be optimized, through a polynomial degree, to better represent the stars observed in the images (spatial variation of the PSF model). Thus if the polynomial degree is zero, the same PSF model is applied to the whole image. If the polynomial degree is linear, a PSF model with linear spatial variance is applied. If it is quadratic, a PSF model with quadratic spatial variance is applied and if it is cubic, a PSF model with cubic spatial variance is applied.

Once the PSF models are determined, the program creates a reference image model, a residual image which is the difference between the model and the reference frame, a sky background image, a list with all the stars detected, their fluxes and positions, and a table with the PSF models used.

Register: In this stage of the reductions, all of the images are aligned (registered) with the reference frame. To do so, DanDIA implements the extended Delaunay triangulation technique explained in Pál & Bakos (2006) which creates a mathematical triangle space and compares triangles formed by the position of the stars between the reference frame and each of the images. Once the triangles are matched, then a linear transformation is fitted and applied to line up the image with the reference.

Subtract: This code determines the kernel model that best matches the reference frame to each of the registered science images to produce the difference images. The method implemented in this step is defined by the very owner of this pipeline in Bramich (2008). The technique, rather than considering a kernel as a linear combination of Gaussian functions, it considers it as a discrete pixel array and solves for the kernel pixel values directly using linear least squares. Several improvements can be obtained using this technique rather than the traditional difference image analysis (see Bramich 2008, for an entire description of the procedure and explanations). The procedure can take into account both spatially invariant and spatially variant kernel solutions, spatially variable differential background and photometric scale factor, and can divide the images into sub-frames to define a grid of kernel solutions.

Once the kernel is created, DanDIA builds a model of each science image by convolving the reference frame with the kernel solution which is multiplied by the photometric scale factor and the differential background solution is added. It also builds a difference image, which is the difference between the science image and the image model created above. Finally, a normalized residual image is created as the normalization of the difference image by the pixel sigmas obtained from the CCD noise model.

Trend-log files are created with information such as the photometric scale factor and differential sky background.

Diphot: The difference fluxes are measured, at the position of the stars obtained from the reference frame, in each of the difference images. This is done by optimally scaling the PSF model of each star to the difference image. In detail this requires interpolation of the local PSF model (obtained from starfit) at the position of a given star with the local kernel solution (obtained in subtract). It is this step where light curves for each of the stars are generated by the pipeline, the total fluxes, magnitudes and their uncertainties are calculated as we previously showed in Equations 2.11, 2.12, and 2.23. The final light curve has 28 columns with the relevant information calculated at the different stages employed during the reductions and photometry extraction. In Table 5.2 they are shown.

Postprocess: Finally, in this stage, the pipeline creates a root mean square versus mean magnitude diagram for all of the stars extracted during the reductions.

5.2 The EMCCD implementation

In the previous chapters, we have covered different aspects of EMCCDs, from their electronics to how they work, the benefits that can be obtained, and how this type of technology can help to improve the quality of the astronomical images and thus the research. Even though this technology has been proven to be very fruitful it is not commonly used yet. From my personal experience in meetings and conferences, people have been insecure about the fact that the read noise can be higher than in CCDs or the fact that it could be also

Table 5.2: Parameters written in the light curve files for each of the stars detected by the DanDIA pipeline.

Column	Parameter
1	Image name
2	Geocentric Julian day
3	Heliocentric Julian day
4	Difference flux (psf)
5	Error on difference flux (psf)
6	Background (psf)
7	Error on background (psf)
8	χ^2
9	Number of good pixels
10	Number of pixels used
11	Star reference flux
12	Star reference flux error
13	Reference frame exposure time
14	Magnitude PSF
15	Error on magnitude PSF
16	Exposure time
17	Background level (flux)
18	Seeing (pixels)
19	Photometric scale factor
20	χ^2 per pixel
21	X position in the CCD
22	Y position in the CCD
23	ΔX in the X position
24	ΔY in the Y position
25	a Image transformation parameter
26	b Image transformation parameter
27	c Image transformation parameter
28	d Image transformation parameter

amplified in the extended register gain. As we already explained in Chapter 2, this occurs when the EMCCD is used in conventional mode when the gain is not amplified and the EMCCD is used as a conventional CCD. Remember that this type of device was not originally created to be used as a CCD but instead to exploit their capabilities using the amplification gain which makes the readout negligible.

We also saw in this thesis how the EMCCD can be used properly and that in fact, it is possible to produce reliable photometry for stars even in crowded fields. Due to the very short exposures times, we do not have to worry about the saturation of the brightest stars, we can co-add as many frames as we would like to produce reference frames with enough signal-to-noise ratio for the fainter stars, and the blurring effect produced by the turbulence atmosphere is mitigated on the images to the point of producing images with the highest angular resolution so far taken with ground-based telescopes. Figure 5.1 illustrates the field of globular cluster NGC 4590 taken with different instruments. In (a) the globular cluster is observed with the ACS instrument at the HST covering $202'' \times 202''$ field of view and a pixel scale of 0.050arcsec/pixel. The small green box, which is zoomed-in in (d) is the field covered by our EMCCD. (b) is a zoomed-in Bessell V-image taken as part of our globular cluster programme with Las Cumbres Observatory/RoboNet 1 m telescope. The CCD camera is a Kodak KAF-16803 models with 4096×4096 pixels and a pixel scale of $0.23''$ per pixel, giving a 15.7×15.7 arcmin^2 field of view. The image was binned to 2048×2048 pixels, meaning that the effective pixel scale of our images is $0.47''$ per pixel. Finally, in (c), we show the same field but observed with our EMCCD camera installed on the Danish 1.54m telescope at La Silla, Chile. As already pointed out, the camera is an Andor Technology iXon+ model 897 EMCCD, with 512×512 16 μm pixels and a pixel scale of $0.09''$ per pixel, giving a field of view of 45×45 arcsec^2. In the images, it is possible to notice how the quality of the image has been greatly improved with the EMCCD in comparison with that taken with CCD approaching the quality of the HST image. Blending among stars is clearly minimized and the background/fainter stars are clearly seem in the EMCCD image contrary to the case of the CCD. The handbook for the ACS instrument suggests that well-dithered observations with the WFC should result in a reconstructed PSF FWHM of $0.1''$ to $0.14''$[1]. The PSF FWHM for our CCD image was $1.49''$ while $0.40''$ with our EMCCD.

Even though the PSF FWHM of $0.40''$ measured in the reference frame for NGC 4590 with the EMCCD and similar values measured in the clusters studied in this thesis (see Table 5.3 in next section) is a great improvement in comparison with the PSF FWHM measured for conventional CCDs, it is important to notice that the quality of the images can still be improved by an important factor to the point of reaching the same quality as those obtained with space telescopes (e. g. HST). During our analysis we employed the shift-and-add technique to produce reference frames usually stacking the 1%, 2%, and 5% layer-frames. However, it is possible to collect a higher number of short-exposure frames to increase the number of better quality images and only consider images from the 1% layer-frames to build the reference images similar to how this is done with lucky imaging. Thus it is possible to obtain resolutions in the range 0.1-0.2 arc seconds under relatively good conditions (Mackay et al. 2004; Law et al. 2006) or even better than that of the HST (Mackay 2013).

The combination of EMCCDs and the shift-and-add technique can still go far further than the analysis we did in this thesis enabling astronomers to continue reaching frontiers that using the conventional CCDs might not be possible to achieve. As pointed out in Mackay et al. (2004), wide-field surveys and resolutions of the order of 0.1-0.2 arc seconds and smaller are fundamental in the study of the systematic distortions of galaxy shapes because their light is bent around concentrations of dark matter in the universe. The diameter of distant galaxies are only a few arc seconds so high signal-to-noise ratios are needed to be able to detect such distortions. They also point out that EMCCD technologies can help to detect mass distribution in three dimensions through weak gravitational lensing which is extremely important in the understanding of the early stages and evolution of the universe. In a similar vein, Law et al. (2006) consider that galactic studies such as binary candidates, brown dwarfs, globular cluster cores and extragalactic studies as quasar host galaxies, damped Lyman-α can be highly benefited by this technology and its techniques. Finally, Mackay et al. (2004) and Tulloch & Dhillon (2011) consider that wide field surveys in both photometry and

[1] http://www.stsci.edu/hst/proposing/documents/primer/Ch_42.html

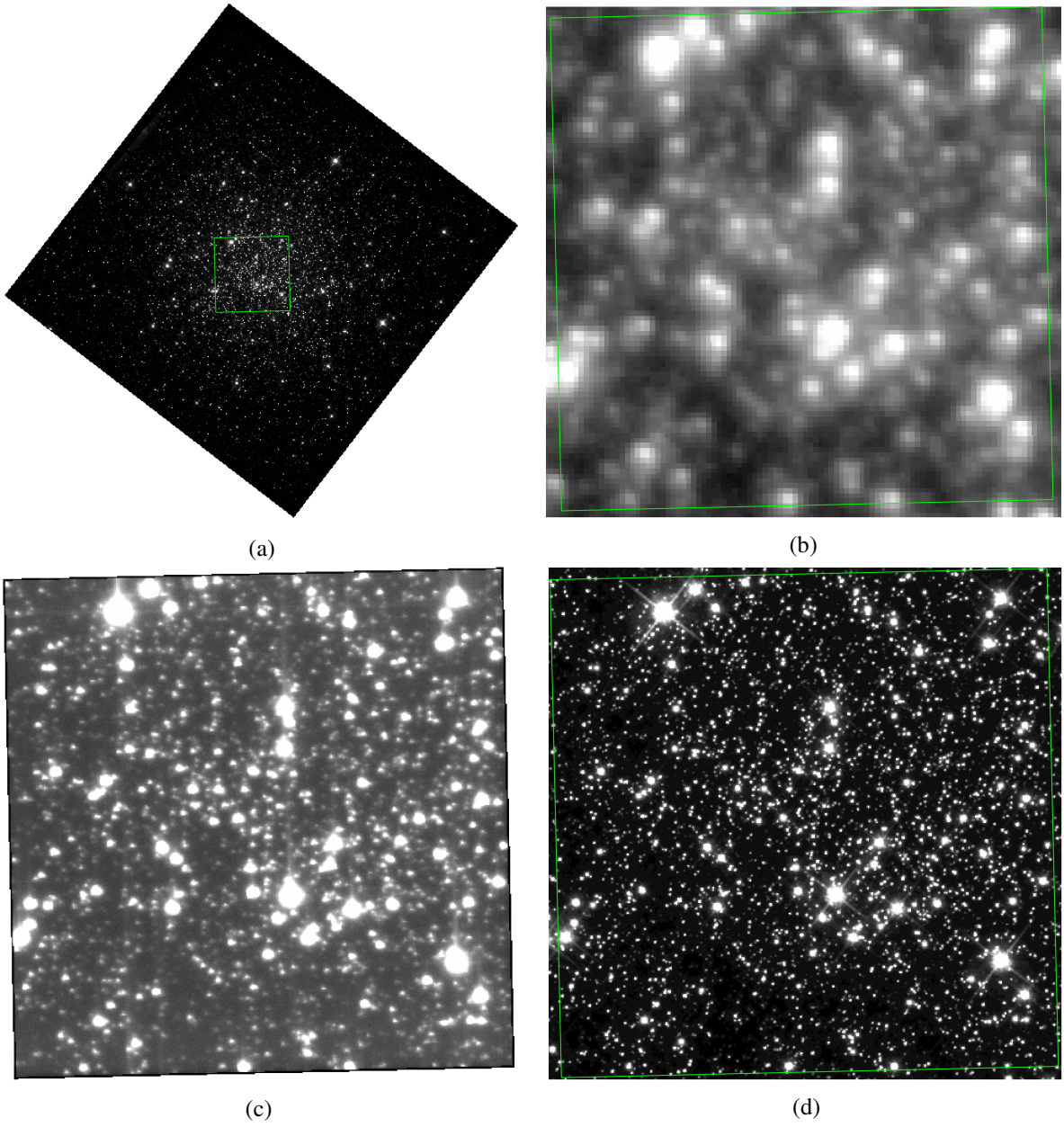

(a) (b) (c) (d)

Figure 5.1: Globular cluster NGC 4590 observed with 3 different cameras. In (a) the field of view correspond to the ACS instrument at the HST and the small green box is the field shown in (d) for the same HST image, (b) for Las Cumbres Observatory camera, and (c) for the EMCCD at the Danish 1.54m telescope. PSF FWHM for (a) and (d) is 0.1″ to 0.14″, 1.49″ in (b), and 0.40″ in (c).

spectroscopy can be made using EMCCDs by properly configuring several of these devices as arrays and even be installing them in telescopes such as the 42 m European Extremely Large Telescope (E-ELT).

5.3 Our analysis

We have performed a deeper analysis of variable star detection for 11 globular clusters in our Galaxy and have found a diversity of interesting results which were presented in previous chapters. However, let us review some aspects below.

In our list of globular clusters, we observed famous globular clusters such as NGC 104 (better known as 47 Tucanae) and NGC 5139 (better known as Omega Centauri). If the physical parameters given in Table 3.2 are compared for the 11 clusters, it is possible to notice that we have covered metallicities [Fe/H] between -0.72 to -1.81 dex which is equivalent to a range in metallicities of -1.09 dex. The magnitudes of the horizontal branch V_{HB} are from 13.45 to 18.16 mag for a range of 4.71 mag. Distance modulus $V - M_V$ was between 12.82 to 17.58 mag for a range of 4.76 mag. The central luminosity density ρ_0 goes from 2.79 to 5.82 dex for a range of 3.03 dex. Additionally, the FWHM measured in the reference frames was from 0.37 to 0.61 arcsec with a mean of 0.49 arcsec. In Table 5.3 these intervals are shown.

Table 5.3: The intervals covered by several parameters of the 11 globular clusters are shown. Column 1 is the interval in metallicities, Column 2 corresponds to the interval covered in the magnitude level of the horizontal branch, Column 3 is for distance modulus, Column 4 for central luminosity density and column 5 for FWHM measured in the reference frames

[Fe/H]	V_{HB}	$V - M_V$	ρ_0	FWHM
	mag	mag		arcsec
from - to	from - to	from - to	from - to	from - to
−0.78 −1.81	13.45 18.16	12.82 17.58	2.79 5.82	0.37 0.61

Similarly, in Table 5.4 we summarize some data related to our observations. Thus, NGC 5139 is the cluster with the highest number of stars detected with 2616 stars and it is NGC 104 which is the cluster with the least number of detection with 507 stars. In the range of magnitudes covered, it was NGC 6656 where we covered the largest range with 9.54 mag in contrast to NGC 6715 for which we covered the shortest range with 5.53 mag. Notice that for globular clusters NGC 6121, NGC 6656, NGC 6656, and NGC 6656, no new variable stars were detected in the range of magnitudes covered in this study. The reader should find this interesting even though no new variables were found because our analysis helped to properly corroborate the completeness of previous studies related to the search for variables has in the range of magnitudes we have covered. NGC 6715 and NGC 5286 are the clusters in which we discovered the highest number of new variables and it is worth noticing that these two clusters have 200 and 58 already known variables, respectively, which also shows the impact of our research to properly study crowded star fields.

From the numbers given in Table 5.4, the 97 new variable stars discovered in this work are divided into 37 long-period, 34 RR Lyrae, 10 semi-regular, 1 W Virginis, 1 eclipsing binary, 1 SX Phoenicis, and 13 unclassified. Similarly, we detected and corroborated the variability of 48 previously known variables from which 36 are RR Lyrae, 3 are long-period, 3 semi-regular, 3 cataclysmic variables, 1 SX Phoenicis, 1 eclipsing binary, and 1 unclassified. The new discoveries of long-period and semi-regular variables might show that these variables could be as common as RR Lyrae are in globular clusters. It is also likely that they were not discovered before because they were saturated in the images taken on these clusters and/or they were blended with other stars and their low-amplitude variability information was lost. As part of testing the quality and reliability of our data with the EMCCD, it is important to notice that we recovered the variability information of the previously known variables in the field of view covered by our observations and we have supplied to the astronomical community light curves with a better coverage and refined periods and amplitudes.

Table 5.4: Variables and magnitude ranges covered by our observations for the 11 globular clusters. Column 1 is the name of the globular cluster, Column 2 is the number of stars detected inside the field of view of our reference frame for each cluster, Column 3 is the number of epochs of our observations, Column 4 is the magnitude of the brightest star we detected, Column 5 is the magnitude of the faintest star detected, Column 6 is the range in magnitude covered by our observations, Column 7 is the number of previously known variable stars in the cluster (inside and outside our field of view), Column 8 is the number of new discoveries we made.

id	Stars	Epochs	Max	Min	Range	Known	New
NGC	#	HJD	mag	mag	mag	#	#
104	507	149	9.59	16.08	6.50	300	7
5139	2616	78	10.21	19.61	9.40	400	3
5286	1903	74	11.54	19.40	7.87	58	11
6093	1220	62	11.40	18.58	7.18	34	6
6121	681	64	10.99	20.26	9.27	100	0
6541	843	43	10.76	18.06	7.30	20	2
6656	1445	51	9.40	18.94	9.54	100	0
6681	1315	50	11.68	19.63	7.95	5	1
6715	1402	44	12.76	18.29	5.53	200	67
6723	1258	56	11.20	19.88	8.69	47	0
6752	794	78	10.77	17.95	7.18	32	0

In NGC 104, we have nicely covered an important fraction of its CMD from the top of the red giant branch, with the discovery of the long-period and semi-regular variables, to a region close to what could be the top of the blue straggler zone. Notice that we have two unclassified variables, they appear to be close to the blue straggler zone, which might be an indication that these two stars are SX Phoenicis. Going further down in the CMD may result in the discovery of several SX Phoenicis.

In NGC 5139, we did not find any RR Lyrae variables. The cluster has a very well pronounced blue horizontal branch. The one unclassified variable we discovered is at the beginning of the red giant branch and our coverage goes down in the CMD about 19.6 mag. There is no evidence for any SX Phoenicis variables in the field of view covered by our reference frame.

In NGC 5286, we have also nicely covered the CMD with the discovery of long-period and semi-regular variables from the top of the red giant branch to the blue straggler zone with the discovery of one SX Phoenicis. Further studies deeper in the CMD might result in the discovery of more SX Phoenicis. From the RR Lyrae in this study, we have helped to corroborate that this cluster is an Oosterhoff II type.

In NGC 6093, only new long-period variables were discovered. However, we also detected several previously known RR Lyraes for which nicely covered light curves and period improvements are supplied. Particularly interesting in this globular cluster is the case of the star labeled as V34 which is classified as cataclysmic variable as a Nova sub-type. It turned out that this is the famous case of the 1860 Nova discovered by Arthur von Auwers at Koenigsberg Observatory and no visual observations for this star in outburst were made until this study.

In NGC 6121, we only detected a previously known RR Lyrae and no new variables were found. Further studies in fainter magnitudes of the CMD could result in the discovery of new variables.

In NGC 6541, we have detected only 3 variables from which two are new discoveries, one a long-period variable, and one RR Lyrae. The previously known variable is an SX Phoenicis in the blue straggler zone which gives us a nice coverage of the CMD. The range of magnitudes covered by our observations does not indicate more variables in the CMD for the stars covered in our field of view.

In NGC 6656, no new discoveries were made. However, we presented light curves for 3 previously known variables. A semi-regular, an eclipsing binary, and a cataclysmic variable sub-classified as Nova for

which we covered its outburst. The eclipsing binary and the Nova are below the turn-off point of the CMD and there is no indication of new variables inside our field of view.

In NGC 6681, one new RR Lyrae was discovered and none of the previously known variables were inside our field of view. The range of magnitudes covered by our observations in the CMD does not indicate more variables toward the blue straggler zone.

In NGC 6715, we have discovered 67 new variable stars. From the magnitudes covered in the CMD, it is possible to see that we covered from the top of the red giant branch to the horizontal branch with the discovery of 30 RR Lyrae, 21 long-period irregulars, 3 semi-regular, 1 W Virginis, 1 eclipsing binary, and 11 were unclassified. However, we did not cover down to regions such as the blue straggler zone. Observations further down in the CMD might result also with a high number of new discoveries. This globular cluster was particularly interesting because it was previously observed by the HST and OGLE survey and our discoveries were missed in their analysis mainly due to blending in the very crowded central region of the cluster or/and saturation of the brightest stars. It shows the challenges observations with conventional CCDs have to deal with when observing crowded fields, especially in the case of variable sources. It also shows the advantages and capabilities of EMCCDs and the techniques employed in this work. The new RR Lyrae discoveries helped us to confirm that this globular cluster is indeed of intermediate Oosterhoff type.

In NGC 6723, no new variables were found but there were four previously known RR Lyrae in our field of view which were used in the period-amplitude diagram to help to corroborate that this cluster is of Oosterhoff I type. The magnitude coverage in the cmd for this cluster does not indicate the presence of more variables in the field and magnitude range coverage.

In NGC 6752, no new variables were found. However, we covered the outburst of a previously known dwarf nova. The cluster has several known pulsars in the field of view covered by our reference frame but no visual counterpart was detected in our observations.

5.4 Our future work

This study has helped to produce images with the highest angular resolution so far taken with ground-based telescopes for the 11 globular clusters presented in this thesis. We have properly studied and covered a wide range of magnitudes in the color-magnitude diagrams for variable star detection. We discovered a wide number of variable stars and corroborated the variability of variables previously known in the field of view of our reference frames. We calculated and improved periods and light curve coverage for all the variables, calculated their astrometric solution, and gave precise positions in the finding charts and astronomical coordinates in our tables. Characteristics of their variability were also given. Ephemerides and photometric measurements for the variable stars are available in electronic form through the Strasbourg Astronomical Data Centre.

Even though we presented a linear transformation to the standard system of the form

$$M_{std} = aM_{ins} + b \tag{5.2}$$

where M_{std} is the standard magnitude for a given filter, M_{ins} is the instrumental magnitude for a given filter and a and c the linear coefficients of the transformation, we did not consider a color correction in our transformation. We have now equipped the Danish 1.54m telescope with a secondary EMCCD camera that covers a visual-band which is equivalent to a wavelength from about 450 nm to 650 nm which is roughly equivalent to SDSS $g' + r'$(see Skottfelt et al. 2015c). Both cameras are configured to take simultaneous observations of the same field observed. With this new implementation, we are now able to produce a linear transformation to the standard system using a color term correction of the form e. g.

$$V - v = a(v - i) + c \tag{5.3}$$

where v and i are the instrumental magnitudes in the visual and infrared, respectively, V is the standard magnitude in the visual, and a and c are the linear coefficients of the transformation (see Figuera Jaimes

et al. 2013, where we first employed this transformation with a CCD study).

With the two cameras, we are able now to produce simultaneous colour information to produce the first color-magnitude diagrams obtained with EMCCD observations. Variability of the new discoveries can be confirmed through two different colors independently.

Moving forward with our study, we will review how well our data can be used to test semi-empirical calibrations already available in the literature to determine physical parameters of the variables and the clusters (as shown in the introduction). Because of the wide wavelength covered by our two cameras, new calibrations might need to be developed.

During these years, apart from the 11 globular clusters selected for this thesis, we have continued taking observations for a wide group of globular clusters. Our main goal in this part is to properly resolve the crowded central region of all globular clusters visible from La Silla Observatory and to properly detect and characterize their variable stars.

For variables in the asymptotic and red giant branch, we plan to continue monitoring globular clusters with the aim of updating the number of these variables and to have these types of variables available in a wide range of cluster metallicities, and along with spectroscopic studies, perform a proper determination of their physical properties. Thus, in the case of long-period variables, we may corroborate if they do really have a relation between their luminosity and metallicities (Frogel & Whitelock 1998). Additionally, with the parameters we already know from photometry such as their periods, amplitudes, median magnitudes and in combination with spectra, we will find possible relations between physical properties of the stars and their possible connection with physical parameters of the clusters similar to how it occurs for RR Lyrae stars. We will try to infer possible connections of their variability with mass loss and evolutionary stages before the helium flash. It is also thought that the variability of these stars could be due to large and cool photospheric zones produced by stellar rotation which has also been associated with the "second parameter" in the horizontal branch morphology (Welty 1985, and references therein).

For RR Lyrae stars we plan to review the validity of using the semi-empirical calibrations with the filters employed in our work and if needed adapt them or create new calibrations for our filters. Apart from updating the census of these variables in the globular clusters, we also plan to review the Blazhko effect. To do so we observed a globular cluster which is known to have a high number of RR Lyrae using the Las Cumbres Observatory network of robotic telescopes. Due to the distribution of the telescopes along both Southern and Northern hemispheres, it was possible to observe the cluster 24 hours continuously and for several days.

In the case of binary systems, we plan to continue our monitoring for the detection and period determination of these stars. Additionally, we will take spectra of these stars to be able to determine their radial velocities and thus their eccentricity. Finally, with these parameters, we will be able to constrain the mass of the binary systems.

We will expand our survey of the globular clusters to cover a wider range of wavelength in the electromagnetic spectrum through multi-color photometry. The addition of more filters to our observations will help us to monitor and discover systems such as cataclysmic variables. In the introduction, we already pointed out that this type of variable is expected to be found in high quantities in the denser globular clusters. However, during the last years, they have not been found in such numbers. Thus, observations aiming to detect these stars should also take into account, apart from visual observations, their emission lines in the spectra, excessively blue color and/or X-ray emission (Knigge et al. 2008).

In a similar vein, to continue exploiting the capabilities of the EMCCD to the maximum, we will produce reference frames with enough signal to noise ratio to reach the faintest zones of the color-magnitude diagram. With this we will be able to properly cover the blue straggler zones to discriminate which stars belong to them and to properly update the SX Phoenicis population for each of the clusters observed. These stars will help us to calculate distances to the clusters as an independent method. Additionally, as these stars are in the instability strip, they are pulsating variables, so we will search for relations between their physical properties and the parameters related with their variability, as in the case of RR Lyrae stars.

Other types of peculiar stars, variables, and symbiotic stars can also be discovered. The capabilities of the EMCCDs enable us to detect other types of physical systems such as intermediate mass-black holes in

the center of globular clusters. Even though it is thought they were dynamically ejected from the densest core of globular clusters, they can survive in clusters with intermediate density and capture stars to form low-mass X-ray binary systems (Kulkarni et al. 1993). More recent comparisons between observations and simulations suggest the presence of intermediate-mass black holes with masses of about 10^2-$10^5 M_\odot$ in the center of globular clusters (e. g. Lützgendorf et al. 2013; Feldmeier et al. 2013). We can compare the position of the stars in our images with those obtained years ago by the HST to infer any presence of the IMBHs through e. g. astrometric microlensing (Kains et al. 2017). Another way is by microlensing events.

Some references in literature are related to the observation of microlensing events in globular clusters (Pietrukowicz et al. 2012; de Luca & Jetzer 2008; Jetzer et al. 1998; Sahu et al. 2001b). The first microlensing event in a globular cluster was found by Pietrukowicz et al. (2012). It was found in the globular cluster M22, with data obtained using the adaptive optics system NACO at ESO VLT. It shows that the lensing event is a low mass star with $\sim 0.18 M_\odot$. de Luca & Jetzer (2008) says that an important fraction of the mass in the globular clusters could be represented by brown dwarfs and low mass stars. Through microlensing, observations in these stellar systems could be a possible way to understand this issue. One of their main conclusions is that more observations focused on the detection of microlensing events in globular clusters are needed.

Safonova & Stalin (2010) did research into the feasibility of finding black holes in globular clusters by using microlensing. They say correlations between the super-massive black holes and their host galaxies suggest that globular clusters also follow the same pattern. Almost all the effort put into detections of black holes is indirect and has a lot of observational constraints mainly because of the **crowding central region in globular clusters**. They argue that, if the globular cluster center is resolved properly, then a direct determination of the lensing curve will be possible, and also of the lensing parameters produced by the presence of IMBH in the clusters.

To help us accomplish the ideas commented above, apart from continuing to use the Danish 1.54 m telescope with the EMCCD, we aim to support our observations with some facilities such as the two Monet 1.2 m telescopes at McDonald Observatory (Texas, USA) and at The South African Astronomical Observatory (South Africa) who also joined the MINDSTEp consortium efforts with the EMCCD technologies. We plan to also include MPG/ESO 2.2-metre telescope at La Silla Observatory which is equipped with a 67-million pixel Wide Field Imager capable of covering the field of view similar to the full moon. It also has GROND, the Gamma-Ray Burst Optical/Near-Infrared Detector, and FEROS, a high-resolution spectrograph. We have also already included in our efforts Las Cumbres Observatory which is a network of twenty-one robotic telescopes at eight sites around the world in which we have been accumulating ~600 hours of multi-color photometry of selected globular clusters in both hemispheres. Finally, in this Ph. D. we prepared a set of codes that help us to automatically control and manipulate our observations from the moment they are taken, including automatic reduction procedures using DanDIA, and automatic or semi-automatic variable stars detection and extraction.

Appendix A

Histogram of observations

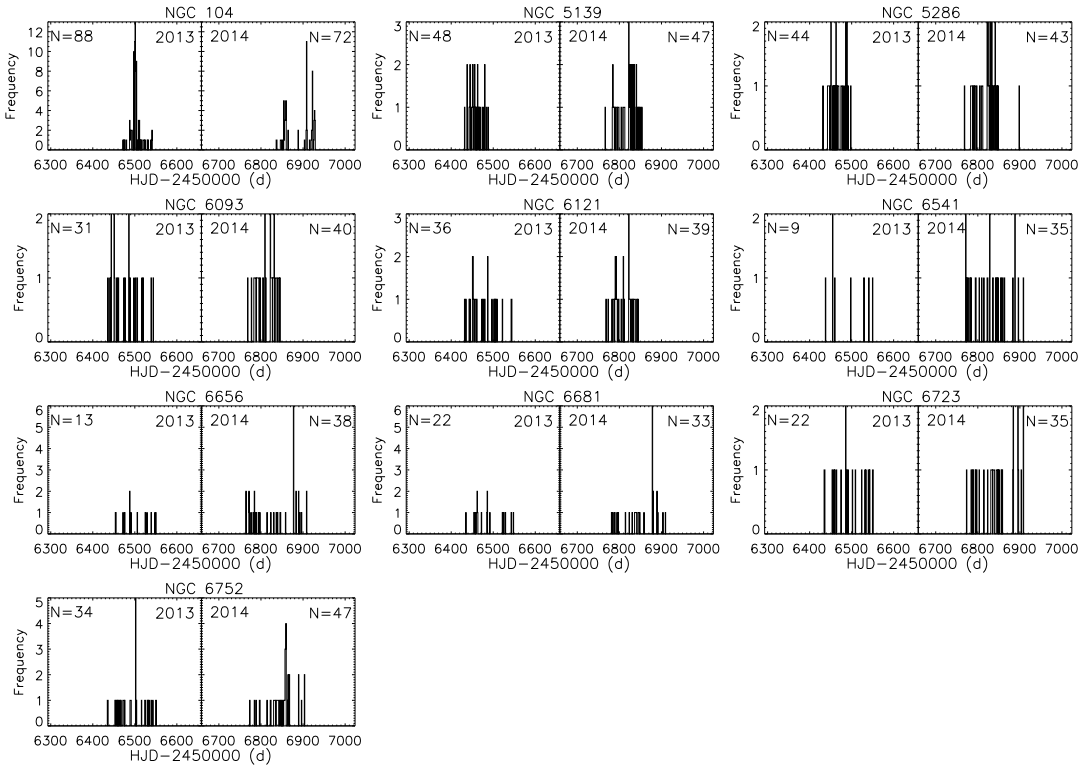

Figure A.1: Each plot represents the histograms with the number of data taken for each globular cluster during the different observational seasons. The boxes correspond to each year.

Appendix B

Photometric calibrations

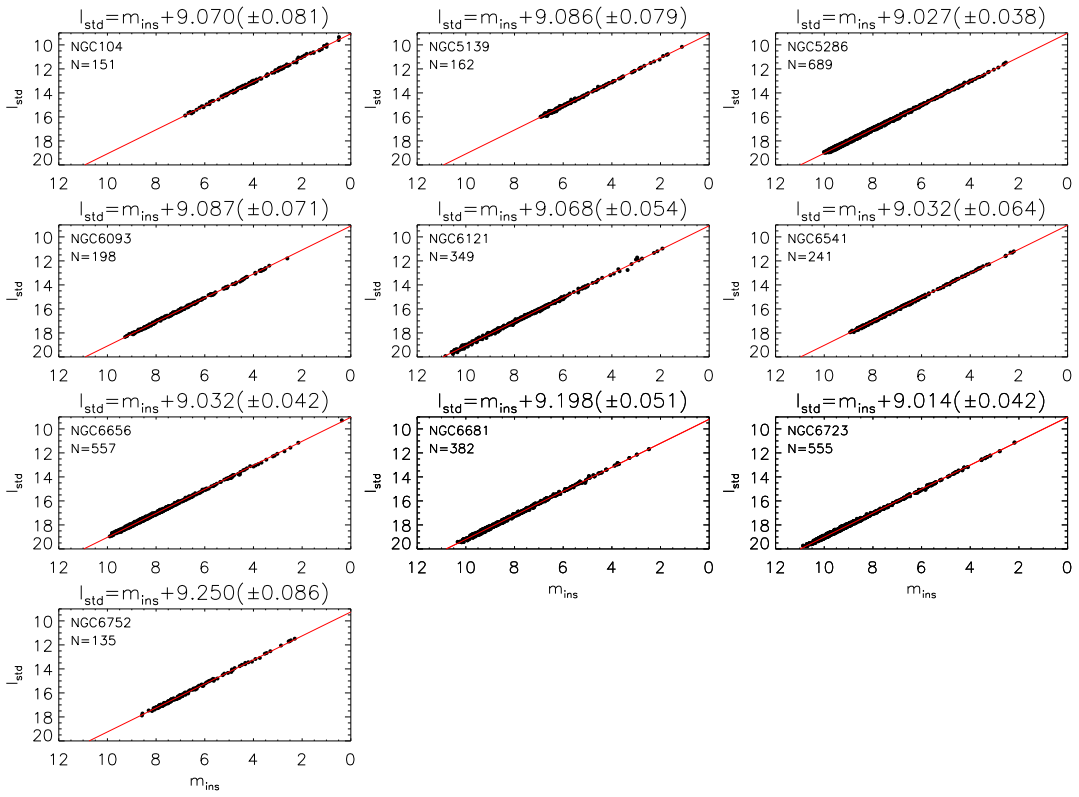

Figure B.1: Standard I magnitude taken from the HST observations as a function of the instrumental i′ + z′ magnitude. The red lines are the fits that best match the data and they are described by the equations in the titles of each plot. The correlation coefficient is 0.999 in all cases.

Appendix C

Cross identification between variables

Table C.1: Cross identification between the RR Lyrae variables listed by the CVSGGC (Clement et al. 2001), the variable star candidates from Montiel & Mighell (2010), and the OGLE RR Lyrae stars (Udalski et al. 2015)

CVSGGC id	OGLE id (OGLE-BLG-)	Montiel id	CVSGGC id	OGLE id	Montiel id	CVSGGC id	OGLE id	Montiel id
V3	RRLYR-37571		V77	RRLYR-37524		V152	RRLYR-37615	
V4	RRLYR-37540		V78	RRLYR-37629		V158	RRLYR-37539	
V5	RRLYR-37518		V80	RRLYR-37624		V159	RRLYR-37589	
V6	RRLYR-37655		V82	RRLYR-37548		V160	RRLYR-37595	VC34
V7	RRLYR-37620		V83	RRLYR-37522		V161	RRLYR-37616	
V12	RRLYR-37511		V84	RRLYR-37577		V162	RRLYR-37592	VC11
V15	RRLYR-37649		V85	RRLYR-37569		V163	RRLYR-37604	VC12
V28	RRLYR-37623		V87	RRLYR-37641		V164	RRLYR-37564	VC14
V29	RRLYR-37519		V88	RRLYR-37515		V165	RRLYR-37609	
V31	RRLYR-37528		V89	RRLYR-37530		V168	RRLYR-37619	
V32	RRLYR-37514		V90	RRLYR-37622		V172	RRLYR-37614	
V33	RRLYR-37631		V92	RRLYR-37611		V174	RRLYR-37608	
V34	RRLYR-37541		V93	RRLYR-37567		V176	RRLYR-37618	
V35	RRLYR-37533		V94	RRLYR-37634		V177	RRLYR-37556	
V36	RRLYR-37648		V95	RRLYR-37560	VC13	V178	RRLYR-37562	
V37	RRLYR-37617		V97	RRLYR-37607		V179	RRLYR-37557	VC18
V38	RRLYR-37538		V98	RRLYR-37637		V180	RRLYR-37588	
V39	RRLYR-37527		V118	RRLYR-37660		V181	–	VC28
V40	RRLYR-37543		V119	RRLYR-37654		V182	RRLYR-37561	
V41	RRLYR-37647		V120	RRLYR-37638		V183	RRLYR-37603	
V42	RRLYR-37626		V121	RRLYR-37635		V184	RRLYR-37559	
V43	RRLYR-37516		V122	RRLYR-37632		V185	RRLYR-37563	
V44	RRLYR-37599		V123	RRLYR-37583		V186	RRLYR-37546	
V45	RRLYR-37646		V124	RRLYR-37628		V188	RRLYR-37584	
V46	RRLYR-37552	VC44	V125	RRLYR-37613		V192	RRLYR-37568	VC46
V47	RRLYR-37554		V126	RRLYR-37600		V193	RRLYR-37605	
V48	RRLYR-37659		V127	RRLYR-37580	VC2	V194	RRLYR-37574	
V49	RRLYR-37532		V128	RRLYR-37551		V227	RRLYR-37582	
V50	RRLYR-37640		V129	RRLYR-37526	VC17	V228	RRLYR-37575	
V51	RRLYR-37657		V130	RRLYR-37549		V229	RRLYR-37597	
V52	RRLYR-37636		V131	RRLYR-37525		V233	RRLYR-37591	
V54	RRLYR-37521		V132	RRLYR-37555		V236	RRLYR-37585	
V55	RRLYR-37651		V133	RRLYR-37550		V237	RRLYR-37570	
V57	RRLYR-37666		V136	RRLYR-37513		V240	RRLYR-37576	
V58	RRLYR-37630		V137	RRLYR-37612		V244	RRLYR-37581	
V59	RRLYR-37512		V138	RRLYR-37610		V246	RRLYR-37573	
V60	RRLYR-37509		V139	RRLYR-37596		V250	RRLYR-37590	
V61	RRLYR-37547		V140	RRLYR-37572		V251	RRLYR-37579	
V62	RRLYR-37531		V141	RRLYR-37558		V252	RRLYR-37593	
V63	RRLYR-37553		V142	RRLYR-37545	VC15	V253	RRLYR-37586	
V67	RRLYR-37587		V143	RRLYR-37534		–	RRLYR-37565	
V69	RRLYR-37505		V147	RRLYR-37602		–	RRLYR-37578	VC38
V74	RRLYR-37645		V148	–	VC45	–	RRLYR-37594	
V76	RRLYR-37529	VC47	V151	RRLYR-37517		–	RRLYR-37621	

Bibliography

Abell, G. O. 1982, Science, 217, 1280

Albrow, M. D., Gilliland, R. L., Brown, T. M., et al. 2001, ApJ, 559, 1060

Alcock, C., Allsman, R., Alves, D. R., et al. 2000, ApJ, 542, 257

Alonso-Garcia, J., Minniti, D., Angeloni, R., et al. 2015, The Astronomer's Telegram, 7238, 1

Anderson, J., Cool, A. M., & King, I. R. 2003, Astrophysical Journal, Letters, 597, L137

Anderson, J., Sarajedini, A., Bedin, L. R., et al. 2008, AJ, 135, 2055

Ashman, K. M. & Zepf, S. E. 1998, Globular Cluster Systems

Bailey, S. I. 1902, Annals of Harvard College Observatory, 38, 1

Beletic, J. & Amico, P. 1998, in Optical Detectors for Astronomy, Vol. 228

Belloni, D., Giersz, M., Askar, A., & Hypki, A. 2016, Mem. Societa Astronomica Italiana, 87, 551

Bessell, M. S. 2005, ARAA, 43, 293

Binney, J. & Merrifield, M. 1998, Galactic Astronomy

Blažko, S. 1907, Astronomische Nachrichten, 175, 325

Boyle, W. S. & Smith, G. E. 1970, Bell System Technical Journal, 49, 587

Bramich, D. M. 2008, MNRAS, 386, L77

Bramich, D. M., Bachelet, E., Alsubai, K. A., Mislis, D., & Parley, N. 2015, A&A, 577, A108

Bramich, D. M., Figuera Jaimes, R., Giridhar, S., & Arellano Ferro, A. 2011, MNRAS, 413, 1275

Bramich, D. M., Horne, K., Albrow, M. D., et al. 2013, MNRAS, 428, 2275

Brown, T. M., Ferguson, H. C., Smith, E., et al. 2004, AJ, 127, 2738

Burke, Jr., E. W., Rolland, W. W., & Boy, W. R. 1970, JRASC, 64, 353

Cacciari, C., Corwin, T. M., & Carney, B. W. 2005, AJ, 129, 267

Catelan, M. 2004, in Astronomical Society of the Pacific Conference Series, Vol. 310, IAU Colloq. 193: Variable Stars in the Local Group, ed. D. W. Kurtz & K. R. Pollard, 113

Catelan, M. 2009, Astrophysics and Space Science, 320, 261

Ciceri, S., Mancini, L., Southworth, J., et al. 2016, MNRAS, 456, 990

Clement, C. M., Muzzin, A., Dufton, Q., et al. 2001, AJ, 122, 2587

Clement, C. M. & Shelton, I. 1999, Astrophysical Journal, Letters, 515, L85

Cohen, R. E. & Sarajedini, A. 2012, MNRAS, 419, 342

Cox, A. N., Hodson, S. W., & Clancy, S. P. 1983, ApJ, 266, 94

Cseresnjes, P. 2001, A&A, 375, 909

D'Amico, N., Lyne, A. G., Manchester, R. N., Possenti, A., & Camilo, F. 2001, Astrophysical Journal, Letters, 548, L171

D'Amico, N., Possenti, A., Fici, L., et al. 2002, Astrophysical Journal, Letters, 570, L89

de Luca, F. & Jetzer, P. 2008, International Journal of Modern Physics D, 17, 2305

Denvir, D. J. & Conroy, E. 2003, in Proceedings of the SPIE, Vol. 4796, Low-Light-Level and Real-Time Imaging Systems, Components, and Applications, ed. C. B. Johnson, D. Sinha, & P. A. Laplante, 164–174

Díaz-Sánchez, A., Pérez-Garrido, A., Villó, I., et al. 2012, MNRAS, 423, 2260

Dickens, R. J. 1970, ApJS, 22, 249

Dickens, R. J. & Saunders, J. 1965, Royal Greenwich Observatory Bulletins, 101, 101

Dieball, A., Long, K. S., Knigge, C., Thomson, G. S., & Zurek, D. R. 2010, ApJ, 710, 332

Diolaiti, E., Bendinelli, O., Bonaccini, D., et al. 2000a, Astron. Astrophys. Suppl. Ser., 147, 335

Diolaiti, E., Bendinelli, O., Bonaccini, D., et al. 2000b, Astron. Astrophys. Suppl. Ser., 147, 335

Djorgovski, S. 1993, in Astronomical Society of the Pacific Conference Series, Vol. 50, Structure and Dynamics of Globular Clusters, ed. S. G. Djorgovski & G. Meylan, 373

Draper, P. W. 2000, in Astronomical Society of the Pacific Conference Series, Vol. 216, Astronomical Data Analysis Software and Systems IX, ed. N. Manset, C. Veillet, & D. Crabtree, 615

Dworetsky, M. M. 1983, MNRAS, 203, 917

Feldmeier, A., Lützgendorf, N., Neumayer, N., et al. 2013, A&A, 554, A63

Fernie, J. D. 1969, PASP, 81, 707

Figuera Jaimes, R., Arellano Ferro, A., Bramich, D. M., & Giridhar, S. 2011, in Revista Mexicana de Astronomia y Astrofisica Conference Series, Vol. 40, Revista Mexicana de Astronomia y Astrofisica Conference Series, 235–236

Figuera Jaimes, R., Arellano Ferro, A., Bramich, D. M., Giridhar, S., & Kuppuswamy, K. 2013, A&A, 556, A20

Figuera Jaimes, R., Bramich, D. M., Kains, N., et al. 2016a, A&A, 592, A120

Figuera Jaimes, R., Bramich, D. M., Skottfelt, J., et al. 2016b, A&A, 588, A128

Fiorentino, G., Lanzoni, B., Dalessandro, E., et al. 2014, ApJ, 783, 34

Fiorentino, G., Marconi, M., Bono, G., et al. 2015, ApJ, 810, 15

Freire, P. C., Camilo, F., Lorimer, D. R., et al. 2001, MNRAS, 326, 901

Frogel, J. A. & Whitelock, P. A. 1998, AJ, 116, 754

Furenlid, I. 1984, AAS Photo Bulletin, 36, 5

Goldsbury, R., Richer, H. B., Anderson, J., et al. 2010, AJ, 140, 1830

Goodman, J. & Hut, P. 1989, Nature, 339, 40

Gratton, R. G., Carretta, E., Bragaglia, A., Lucatello, S., & D'Orazi, V. 2010, A&A, 517, A81

Hansen, C. J., Kawaler, S. D., & Trimble, V. 2004, Stellar interiors : physical principles, structure, and evolution

Harpsøe, K. B. W., Andersen, M. I., & Kjægaard, P. 2012a, A&A, 537, A50

Harpsøe, K. B. W., Jørgensen, U. G., Andersen, M. I., & Grundahl, F. 2012b, A&A, 542, A23

Harris, W. E. 1996, AJ, 112, 1487

Heinke, C. O., Ruiter, A. J., Muno, M. P., & Belczynski, K. 2008, in American Institute of Physics Conference Series, Vol. 1010, A Population Explosion: The Nature & Evolution of X-ray Binaries in Diverse Environments, ed. R. M. Bandyopadhyay, S. Wachter, D. Gelino, & C. R. Gelino, 136–142

Hertzsprung, E. 1913, Astronomische Nachrichten, 196, 201

Howell, S. B. 2006, Handbook of CCD astronomy, Vol. 5 (Cambridge University Press)

Hubble, E. P. 1925, Popular Astronomy, 33

Hut, P., McMillan, S., Goodman, J., et al. 1992, PASP, 104, 981

Jeon, Y.-B., Lee, M. G., Kim, S.-L., & Lee, H. 2003, AJ, 125, 3165

Jerram, P., Pool, P. J., Bell, R., et al. 2001, in Proceedings of the SPIE, Vol. 4306, Sensors and Camera Systems for Scientific, Industrial, and Digital Photography Applications II, ed. M. M. Blouke, J. Canosa, & N. Sampat, 178–186

Jetzer, P., Straessle, M., & Wandeler, U. 1998, AAP, 336, 411

Jones, D. 2006, The Observatory, 126, 379

Jurcsik, J. 1998, A&A, 333, 571

Jurcsik, J. & Kovacs, G. 1996, A&A, 312, 111

Kadla, Z. I., Gerashchenko, A. N., & Malakhova, Y. N. 1996, Information Bulletin on Variable Stars, 4414, 1

Kains, N., Bramich, D. M., Figuera Jaimes, R., et al. 2012, A&A, 548, A92

Kains, N., Calamida, A., Sahu, K. C., et al. 2017, ApJ, 843, 145

Kaluzny, J., Hilditch, R. W., Clement, C., & Rucinski, S. M. 1998, MNRAS, 296, 347

Kaluzny, J., Olech, A., Thompson, I. B., et al. 2004, A&A, 424, 1101

King, I. R. 1966, AJ, 71, 64

Kippenhahn, R., Weigert, A., & Weiss, A. 2012, Stellar Structure and Evolution

Kjeldsen, H. & Frandsen, S. 1992, PASP, 104, 413

Knigge, C. 2012, Mem. Societa Astronomica Italiana, 83, 549

Knigge, C., Dieball, A., Maíz Apellániz, J., et al. 2008, ApJ, 683, 1006

Kopacki, G. 2013, Acta Astronomica, 63, 91

Kouwenhoven, M. B. N., Brown, A. G. A., Zinnecker, H., Kaper, L., & Portegies Zwart, S. F. 2005, A&A, 430, 137

Kovacs, G., Shlosman, I., & Buchler, J. R. 1986, ApJ, 307, 593

Kovács, G. & Walker, A. R. 2001, A&A, 371, 579

Kulkarni, S. R., Hut, P., & McMillan, S. 1993, Nature, 364, 421

Kunder, A., Stetson, P. B., Catelan, M., Walker, A. R., & Amigo, P. 2013, AJ, 145, 33

Lafler, J. & Kinman, T. D. 1965, ApJS, 11, 216

Law, N. M., Mackay, C. D., & Baldwin, J. E. 2006, A&A, 446, 739

Layden, A. C. & Sarajedini, A. 2000a, AJ, 119, 1760

Layden, A. C. & Sarajedini, A. 2000b, AJ, 119, 1760

Leavitt, H. S. & Pickering, E. C. 1912, Harvard College Observatory Circular, 173, 1

Lebzelter, T. & Wood, P. R. 2005, A&A, 441, 1117

Lee, J.-W. & Carney, B. W. 1999, AJ, 118, 1373

Lee, J.-W., López-Morales, M., Hong, K., et al. 2014, ApJS, 210, 6

Léna, P. 1996, in European Southern Observatory Conference and Workshop Proceedings, Vol. 54, European Southern Observatory Conference and Workshop Proceedings, ed. M. Cullum, 317

Lesser, M. 2015, PASP, 127, 1097

Luther. 1860, Astronomical news, 53, 293

Lützgendorf, N., Kissler-Patig, M., Gebhardt, K., et al. 2013, A&A, 552, A49

Mackay, C. 2013, MNRAS, 432, 702

Mackay, C. D., Baldwin, J., Law, N., & Warner, P. 2004, in Proceedings of the SPIE, Vol. 5492, Ground-based Instrumentation for Astronomy, ed. A. F. M. Moorwood & M. Iye, 128–135

Martinez, P. & Klotz, A. 1998, A practical guide to CCD astronomy

Martínez Roger, C., Perez Fournón, I., & Sánchez, F., eds. 1999, Globular clusters. Proceedings.

McDonald, I., Zijlstra, A. A., Sloan, G. C., et al. 2014, MNRAS, 439, 2618

McLaughlin, D. E. & van der Marel, R. P. 2005, ApJS, 161, 304

McNamara, D. H. 1995, AJ, 109, 1751

Milone, A. P. 2013, Mem. Societa Astronomica Italiana, 84, 79

Montiel, E. J. & Mighell, K. J. 2010, AJ, 140, 1500

Morgan, S. M., Wahl, J. N., & Wieckhorst, R. M. 2007, MNRAS, 374, 1421

Moskalik, P. 2013, in Astrophysics and Space Science Proceedings, Vol. 31, Stellar Pulsations: Impact of New Instrumentation and New Insights, ed. J. C. Suárez, R. Garrido, L. A. Balona, & J. Christensen-Dalsgaard, 103

Murdin, P. 2001, Encyclopedia of astronomy and astrophysics

Navarrete, C., Contreras Ramos, R., Catelan, M., et al. 2015, A&A, 577, A99

Nemec, J. M., Smolec, R., Benkő, J. M., et al. 2011, MNRAS, 417, 1022

Netzel, H., Smolec, R., & Dziembowski, W. 2015, MNRAS, 451, L25

O'Meara, S. 2002, The Caldwell Objects, Deep-sky companions (Sky Pub.)

Oosterhoff, P. T. 1939, The Observatory, 62, 104

Pál, A. & Bakos, G. Á. 2006, PASP, 118, 1474

Percy, J. R. 2011, Understanding Variable Stars

Pickering, E. C., Colson, H. R., Fleming, W. P., & Wells, L. D. 1901, ApJ, 13

Pietrukowicz, P. & Kaluzny, J. 2003, Acta Astronomica, 53, 371

Pietrukowicz, P., Minniti, D., Jetzer, P., Alonso-García, J., & Udalski, A. 2012, APJL, 744, L18

Preston, G. W. 1959, ApJ, 130, 507

Rosino, L. 1952, Mem. Societa Astronomica Italiana, 23, 49

Rosino, L. & Nobili, F. 1958, Mem. Societa Astronomica Italiana, 29, 413

Rousset, G., Fontanella, J. C., Kern, P., Gigan, P., & Rigaut, F. 1990, A&A, 230, L29

Ryu, Y.-H., Yee, J. C., Udalski, A., et al. 2018, AJ, 155, 40

Safonova, M. & Stalin, C. S. 2010, NA, 15, 450

Sahay, A., Lebzelter, T., & Wood, P. R. 2014, Publications of the Astron. Soc. of Australia, 31, 12

Sahu, K. C., Casertano, S., Livio, M., et al. 2001a, Nature, 411, 1022

Sahu, K. C., Casertano, S., Livio, M., et al. 2001b, Nat, 411, 1022

Salinas, R., Contreras Ramos, R., Strader, J., et al. 2016, AJ, 152, 55

Samus, N. N., Durlevich, O. V., & et al. 2009a, VizieR Online Data Catalog, 1

Samus, N. N., Kazarovets, E. V., Pastukhova, E. N., Tsvetkova, T. M., & Durlevich, O. V. 2009b, PASP, 121, 1378

Sandage, A. 1981, ApJ, 248, 161

Sawyer, H. B. 1938, JRASC, 32, 69

Sawyer, H. B. 1939, Publications of the David Dunlap Observatory, 1, 125

Scargle, J. D. 1989, ApJ, 343, 874

Shapley, H. 1917, Proceedings of the National Academy of Science, 3, 479

Shapley, H. 1918a, Contributions from the Mount Wilson Observatory / Carnegie Institution of Washington, 151, 1

Shapley, H. 1918b, Contributions from the Mount Wilson Observatory / Carnegie Institution of Washington, 153, 1

Shapley, H. 1918c, Contributions from the Mount Wilson Observatory / Carnegie Institution of Washington, 156, 1

Shapley, H. 1918d, ApJ, 48

Shara, M. M., Hinkley, S., & Zurek, D. R. 2005, ApJ, 634, 1272

Simon, N. R. & Clement, C. M. 1993, ApJ, 410, 526

Sirianni, M., Jee, M. J., Benítez, N., et al. 2005, PASP, 117, 1049

Skottfelt, J., Bramich, D. M., Figuera Jaimes, R., et al. 2015a, A&A, 573, A103

Skottfelt, J., Bramich, D. M., Figuera Jaimes, R., et al. 2013, A&A, 553, A111

Skottfelt, J., Bramich, D. M., Hundertmark, M., et al. 2015b, A&A, 574, A54

Skottfelt, J., Bramich, D. M., Hundertmark, M., et al. 2015c, A&A, 574, A54

Smith, A., Bailey, J., Hough, J. H., & Lee, S. 2009, MNRAS, 398, 2069

Smith, B. A. 1976, in Charge-Coupled Device Technology and Applications, ed. S. Iwasa & W. J. White

Smith, H. A. 1995, Cambridge Astrophysics Series, 27

Smith, H. A. 2004, RR Lyrae Stars, 166

Smith, H. A., Catelan, M., & Kuehn, C. 2011, in RR Lyrae Stars, Metal-Poor Stars, and the Galaxy, ed. A. McWilliam, Vol. 5, 17

Smith, N., Giltinan, A., O'Connor, A., et al. 2008, in Astrophysics and Space Science Library, Vol. 351, Astrophysics and Space Science Library, ed. D. Phelan, O. Ryan, & A. Shearer, 257

Sollima, A., Cacciari, C., Bellazzini, M., & Colucci, S. 2010, MNRAS, 406, 329

Sollima, A., Cassisi, S., Fiorentino, G., & Gratton, R. G. 2014, MNRAS, 444, 1862

Soszyński, I., Udalski, A., Pietrukowicz, P., et al. 2011, Acta Astronomica, 61, 285

Southworth, J., Mancini, L., Ciceri, S., et al. 2015, MNRAS, 447, 711

Stetson, P. B. 1987, PASP, 99, 191

Street, R. A., Tsapras, Y., Hundertmark, M. P. G., et al. 2014, in The Third Hot-wiring the Transient Universe Workshop, ed. P. R. Wozniak, M. J. Graham, A. A. Mahabal, & R. Seaman, 189–195

Tamuz, O., Mazeh, T., & North, P. 2006, MNRAS, 367, 1521

Tanikawa, A. & Fukushige, T. 2009, Publications of the ASJ, 61, 721

Thomson, G. S., Knigge, C., Dieball, A., et al. 2012, MNRAS, 423, 2901

Tulloch, S. 2003, The Newsletter of the Isaac Newton Group of Telescopes, 7, 25

Tulloch, S. M. & Dhillon, V. S. 2011, MNRAS, 411, 211

Udalski, A., Szymanski, M., Kaluzny, J., Kubiak, M., & Mateo, M. 1992, Acta Astronomica, 42, 253

Udalski, A., Szymański, M. K., & Szymański, G. 2015, Acta Astronomica, 65, 1

van Albada, T. S. & Baker, N. 1971, ApJ, 169, 311

van Dokkum, P. G. 2001, PASP, 113, 1420

Wallerstein, G. 2002, PASP, 114, 689

Warner, B. D. 2006, A Practical Guide to Lightcurve Photometry and Analysis

Wehlau, A., Butterworth, S., & Hogg, H. S. 1990, AJ, 99, 1159

Weldrake, D. T. F., Sackett, P. D., & Bridges, T. J. 2007, AJ, 133, 1447

Weldrake, D. T. F., Sackett, P. D., Bridges, T. J., & Freeman, K. C. 2004, AJ, 128, 736

Welty, D. E. 1985, AJ, 90, 2555

Wilson, C. P. 1975, AJ, 80, 175

Wizinowich, P., Acton, D. S., Shelton, C., et al. 2000, PASP, 112, 315

Wrobel, J. M., Greene, J. E., & Ho, L. C. 2011, AJ, 142, 113

Zorotovic, M., Catelan, M., Smith, H. A., et al. 2010, AJ, 139, 357